Classification of Compact Polarimetric Synthetic Aperture Radar Images

by

Mohsen Ghanbari

A thesis
presented to the University of Waterloo
in fulfillment of the
thesis requirement for the degree of
Doctor of Philosophy
in
Systems Design Engineering

Waterloo, Ontario, Canada, 2021

© Mohsen Ghanbari 2021

Examining Committee Membership

The following served on the Examining Committee for this thesis. The decision of the Examining Committee is by majority vote.

External Examiner: Qian (Jenny) Du
Professor, Dept. of Electrical and Computer Engineering,
Mississippi State University

Supervisors: David A. Clausi
Professor, Dept. of Systems Design Engineering,
University of Waterloo

Linlin Xu
Research Assistant Professor,
Dept. of Systems Design Engineering,
University of Waterloo

Internal Member: Andrea Scott
Professor, Dept. of Systems Design Engineering,
University of Waterloo

Alexander Wong
Professor, Dept. of Systems Design Engineering,
University of Waterloo

Internal-External Member: Claude Duguay
Professor, Dept. of Geography and Environmental Management,
University of Waterloo

Author's Declaration

This thesis consists of material all of which I authored or co-authored: see Statement of Contributions included in the thesis. This is a true copy of the thesis, including any required final revisions, as accepted by my examiners.

I understand that my thesis may be made electronically available to the public.

Statement of Contribution

The following three journal papers are used in this thesis. I was a co-author with a major contribution on the design, development, evaluation and writing of the material of papers.

Ghanbari, M., Clausi, D., A., Xu, L., and Jiang, M., (2019, Published). "Contextual Classification of Sea-Ice Types Using Compact Polarimetric SAR Data". *IEEE Transactions on Geoscience and Remote Sensing*, vol. 57, no. 10, pp. 7476-7491.

Ghanbari, M., Clausi, D., A., and Xu, L., (2021, Published). "CP-IRGS: A Region-based Complex Compact Polarimetric SAR Data". *IEEE Journal of Selected Topics in Applied Earth Observations and Remote Sensing*.

Ghanbari, M., Xu, L., and Clausi, D., A., (2021, Submitted). "Local and Global Spatial Information for Land Cover Semi-Supervised Classification of Complex Polarimetric SAR Data". *IEEE Transactions on Geoscience and Remote Sensing*.

Abstract

The RADARSAT Constellation Mission (RCM) was launched in June 2019. RCM, in addition to dual-polarization (DP) and fully quad-polarimetric (QP) imaging modes, provides compact polarimetric (CP) mode data. A CP synthetic aperture radar (SAR) is a coherent DP system in which a single circular polarization is transmitted followed by the reception in two orthogonal linear polarizations. A CP SAR fully characterizes the backscattered field using the Stokes parameters, or equivalently, the complex coherence matrix. This is the main advantage of a CP SAR over the traditional (non-coherent) DP SAR. Therefore, designing scene segmentation and classification methods using CP complex coherence matrix data is advocated in this thesis.

Scene classification of remotely captured images is an important task in monitoring the Earth's surface. The high-resolution RCM CP SAR data can be used for land cover classification as well as sea-ice mapping. Mapping sea ice formed in ocean bodies is important for ship navigation and climate change modeling. The Canadian Ice Service (CIS) has expert ice analysts who manually generate sea-ice maps of Arctic areas on a daily basis. An automated sea-ice mapping process that can provide detailed yet reliable maps of ice types and water is desirable for CIS. In addition to linear DP SAR data in ScanSAR mode (500km), RCM wide-swath CP data (350km) can also be used in operational sea-ice mapping of the vast expanses in the Arctic areas. The smaller swath coverage of QP SAR data (50km) is the reason why the use of QP SAR data is limited for sea-ice mapping.

This thesis involves the design and development of CP classification methods that consist of two steps: an unsupervised segmentation of CP data to identify homogeneous regions (superpixels) and a labeling step where a ground truth label is assigned to each super-pixel. An unsupervised segmentation algorithm is developed based on the existing Iterative Region Growing using Semantics (IRGS) for CP data and is called CP-IRGS. The constituents of feature model and spatial context model energy terms in CP-IRGS are developed based on the statistical properties of CP complex coherence matrix data. The superpixels generated by CP-IRGS are then used in a graph-based labeling method that incorporates the global spatial correlation among super-pixels in CP data.

The classifications of sea-ice and land cover types using test scenes indicate that (a) CP scenes provide improved sea-ice classification than the linear DP scenes, (b) CP-IRGS performs more accurate segmentation than that using only CP channel intensity images, and (c) using global spatial information (provided by a graph-based labeling approach) provides an improvement in classification accuracy values over methods that do not exploit global spatial correlation.

Acknowledgements

Table of Contents

List of Figures

List of Tables

Chapter 1

Introduction

1.1 Domain

The RADARSAT Constellation Mission (RCM) was launched in June 2019, supporting Canada's need for enhancing the operational use of synthetic aperture radar (SAR) data for maritime surveillance, disaster management, and environmental monitoring [1]. In addition to single, dual polarization (DP), and quad-polarimetric (QP) imaging modes, RCM provides wide-swath compact polarimetric (CP) SAR data for which the SAR system receives two coherent linear polarizations in response to a circularly-polarized field on transmit. Moreover, the RCM has the benefit of near daily coverage of all of Canada's coastal areas improving the dynamic monitoring of the Arctic areas [2].

A CP SAR has many advantages over traditional DP SAR systems such as minimum sensitivity to noise and cross-channel errors, being relatively simple to implement, and self-calibration property [3]. Also, the data from a CP SAR is expected to be "as good as" those of a fine QP SAR [4]. More importantly, like DP SAR, CP SAR sensor is able to capture a wide swath width. An important shortcoming of QP SAR is its inability to produce wide swaths which limits the use of QP data [5].

Scene classification is an important task in monitoring the Earth's surface. The high-resolution RCM CP SAR data can be used for land cover classification as well as sea-ice mapping [6, 7]. Freezing of the ocean surface results in forming sea-ice which is mostly formed in polar regions where, on average, it covers about 25 million square kilometers of the Earth's surface. In the Arctic, sea-ice can be an obstacle to shipping. The extent of sea-ice in the Arctic can vary from year to year, which can greatly affect climate [8].

1

Therefore, sea-ice maps are important for environmental monitoring and climate change modeling[1, 2, 9].

Remote sensing satellites are the main source of image data for sea-ice observation. These satellites acquire images in visible, infrared, and microwave spectral ranges. Meteorological satellites (NOAA AVHAR, VIIRS, MODIS, Sentinel-3) provide visible and infrared images with the resolutions of 250m - 1km. Satellites operating in passive microwave with coarser resolutions of 6 - 70km (AMSR2, NOAA AMSU, SSMIS) have cloud-penetrating capability suitable for sea-ice observation. Most importantly, active microwave SAR satellites (RADARSAT-2, Sentinel-1, TerraSAR-X, COSMO-SkyMed, ALOS-2, and RCM satellites) provide data with better resolution (10 - 100m) [10].

Since the polar regions are dark roughly half of the year and often cloud-covered, SAR satellites, which capture images with appropriate resolution and in all-weather and daylight conditions, are very useful in sea-ice mapping [11–13]. Linear dual polarization (DP) SAR data are used by the Canadian Ice Service (CIS) for sea-ice monitoring. CIS uses the wide-swath 500km DP ScanSAR data to generate ice maps of Canadian waters on a daily basis. After the launch of RCM satellites, using RCM CP data along with the DP data is of interest of the CIS.

1.2 Thesis Objectives

Many SAR scenes are processed daily by human analysts, which is very time consuming. CIS personnel classify different ice types in terms of stage of development in the form of ice charts associated with "egg codes". Egg codes contain the ice concentration information interpreted from SAR scenes by CIS experts [8]. This process involves some approximations and can lead to different results through various interpretations. These all make automated SAR scene classification approaches attractive. Although there are many classification methods using SAR data for sea-ice mapping proposed in the literature [11–14], there are a limited number of scene classification studies dealing specifically with CP SAR data [9, 15–17].

There are a number of challenges when designing a classification method using CP SAR images. The input data in DP SAR classification are HH and HV intensity images, and in the case of QP SAR data, are either the 3×3 complex covariance matrix or a set of decomposition features. Unlike DP and QP, CP provides two different data sources: the 2×2 complex coherence matrix and a set of features that are derived from the four-element Stokes vector. The challenge when processing CP SAR data is to design a method

that integrates the special characteristics of CP data. If the data source used is the complex coherence matrix data, the statistical characteristics of this data type need to be incorporated in the classification method. If the input data to the method are Stokes vector-derived features, an understanding of the nature of each feature is necessary for the analysis of classification results.

Several characteristics of CP data make this data type unique compared to DP data type. The intensity images of DP (HH and HV images) each provides different source information, however, since the mean signal values in the two channels of CP (RH and RV images) are at the same level and the first and second order statistics in the channels are identical [3], RH and RV are similar data sources. Another distinction of CP over DP is that DP SAR has the disadvantage of received vertical polarization being cross-polarized (with a horizontally-polarized wave on transmit). However, neither of CP channels is cross-polarized. Also, CP provides Stokes vector which can be used to derive decompositions such as $m - \delta$ or $m - \chi$ [18] to apply a more accurate classification than the case using DP data.

A common-sense approach to scene classification is a two-step method [11]. In the first step, a segmentation is applied on SAR data to determine the homogeneous regions each of which containing one ground truth class. In the second step, the regions specified in the segmentation step are labeled by the use of a supervised or semi-supervised labeling method. Due to the challenges in sea-ice classification using SAR images such as the existence of speckle noise, similar backscatter for different ice types, and intra-class backscatter variability (different backscatter values for the same ice type in different parts of a SAR scene), incorporating spatial context through modeling the spatial correlation among pixels is effective in both segmentation and labeling steps.

Developing a region-based segmentation that models the spatial context information reduces the impact of speckle noise in SAR imagery [11]. A main objective of this thesis is to develop a region-based contextual image segmentation method using CP SAR data. Markov random field (MRF) image segmentation methods are advocated for their use of contextual information [19]. Iterative Region Growing using Semantics (IRGS) is a region-based segmentation algorithm [20] that incorporates edge strength information in MRFs. IRGS segmentation is also adapted to be used for full QP SAR data [21], DP SAR scene classification [11], and hyperspectral images [22]. To the best of our knowledge, no research has been done in contextual segmentation of CP SAR data.

Using a contextual segmentation, a CP SAR scene is divided to regions, also called superpixels, that are assumed to be homogeneous. Classification then involves labeling to assign ground truth labels to the segmentation regions. A labeling method that in-

corporates the global correlation among the superpixels is developed and evaluated. The labeling method utilizes graph learning to predict labels in a semi-supervised manner. Through modeling the global spatial context information by the graph-based method, the labeling approach tackles the issue of intra-class variability over a SAR image. This is because the correlation among superpixels from one certain ground truth class all over the scene is integrated in to the classification model.

The contribution of the thesis resides in three main aspects:

1. The performance of scene classification using reconstructed full QP (namely pseudo-QP) from a CP SAR scene and the derived features from the Stokes vector is investigated, and the result accuracy of CP data is compared to that of DP and full QP data . In particular, a region-based QP-based segmentation models the spatial context information using pseudo-QP data from CP and provides homogeneous regions in a SAR scene. Then, a pixel-based labeling classification using the CP Stokes vector-derived features is performed. The combination of the segmentation and labeling results leads to the final classification maps. A thorough performance analysis of QP reconstruction from CP for the application of sea-ice mapping was also performed (Chapter 2).

2. The statistical properties of complex CP SAR data is described, and an unsupervised segmentation method based on the statistical model of complex CP SAR data is developed. IRGS, a well-known region-based segmentation algorithm, is extended to complex CP data. First, it is demonstrated that the multilook complex (MLC) CP data is complex Wishart-distributed. Then, the unary and pairwise constituents of IRGS are derived specifically for multilook complex CP data type (Chapter 3). From operational perspective, a contribution of the proposed unsupervised segmentation in sea-ice mapping is that the segmentation method segments a CP scene to a certain number of classes, where each class can then be assigned to an ice types by an ice expert.

3. A CP classification methodology is designed that exploits the superpixels generated by the unsupervised segmentation and performs labeling with a graph-based approach. Such a method includes the global correlation among superpixels by utilizing the spatial distance between superpixels as well as the statistical significance between the MLC matrices associated with superpixels. This is discussed in Chapter 4.

4

1.3 Thesis Structure

Each of Chapters 2, 3, and 4 proposes a novel classification method for CP SAR data. The three chapters are based on three published/submitted journal manuscripts [23–25]. The introduction to the chapters and the underlying theory in the three chapters may provide overlapping information.

Following the two-step classification methodology (segmentation followed by labeling), Chapter 2 aims to provide a full-scene classification method of sea-ice types using CP SAR data. To use an existing QP-based segmentation method, QP data is reconstructed from CP data. An SVM labeling method is then performed to assign ice type labels to segmentation regions.

Since QP reconstruction from CP entails invoking certain symmetry arguments that might be not valid, directly using complex CP data is more desirable. Chapter 3 proposes an unsupervised region-based segmentation method based on the statistical properties of complex CP SAR data. The segmentation method developed in Chapter 3 can be used to identify homogeneous regions (superpixels) in the image. To model the spatial correlation among all the superpixels in the image, a graph is used. Chapter 4 describes a semi-supervised classification method which is based on the graph built on superpixels. A summary of contributions and conclusions are provided in Chapter 5 where, finally, the future work is described.

Chapter 2

Sea-Ice Type Classification Methodology

The purpose of this chapter is to implement a CP dedicated automatic full scene classification approach for sea-ice mapping. A two-step methodology comprising an unsupervised segmentation method (to segment ice-class homogeneous regions) and a supervised labeling method (to classify the ice-type labels for each homogeneous region) is designed. Two complex quad-polarimetric RADARSAT-2 scenes are used to mathematically derive corresponding CP scenes for algorithm testing. This chapter is a refereed journal publication [23].

2.1 Introduction

Sea-ice maps are important for ship navigation, environmental monitoring, and climate change modeling. Satellite synthetic aperture radar (SAR) imagery has been the most important asset for sea-ice mapping for over two decades. The current SAR imagery, that is acquired in any weather and day-light conditions, has proven to be beneficial, specifically for Arctic regions [11–13]. Linear dual polarization (DP) SAR data provided by RADARSAT-2 is currently the primary SAR data source used by the Canadian Ice Service (CIS) for sea-ice monitoring. CIS uses the wide-swath 500km DP ScanSAR data to generate ice maps of Canadian waters on a daily basis. Recently, the RADARSAT Constellation Mission (RCM) was launched supporting Canada's need for enhancing the operational use of SAR data for maritime surveillance, disaster management, and environmental monitoring [1].

In addition to single, DP, and quad-polarimetric (QP) imaging modes, RCM will provide wide-swath coverage CP SAR data for which the SAR system receives two coherent linear polarizations in response to a circularly-polarized field on transmit. Moreover, the RCM has the benefit of near daily coverage of all of Canada's coastal areas improving the dynamic monitoring of the Arctic areas [2]. A CP SAR has many advantages over other DP SAR systems such as minimum sensitivity to noise and cross-channel errors, being relatively simple to implement, and self-calibration property [3]. More importantly, like a DP SAR, a CP SAR is able to capture a wide swath necessary for operational sea-ice mapping. An important shortcoming of QP SAR is its inability to produce wide swaths (limited to 100km in RADARSAT-2) which limits the use of QP data for operational sea-ice mapping [5].

Many SAR scenes are processed daily by human analysts which is very time consuming, making automated scene classification approaches attractive. Although there are many classification methods using SAR data for sea-ice mapping proposed in the literature [11–14], there are a limited number of papers published dealing specifically with CP SAR data for ice-type mapping [9, 15–17]. To the best of our knowledge, there is no study that utilizes the contextual information in CP SAR data to classify ice types. Incorporating a region-based segmentation that models the spatial context information reduces the impact of speckle noise in SAR imagery [11]. Here, we develop a multi-class ice-type classification method that uses region-based segmentation for CP data.

Markov random field (MRF) image segmentation methods are advocated for their use of spatial-context information [19]. We apply the unsupervised segmentation algorithm called IRGS [26] to determine the homogeneous regions of ice types and open water. Other than modeling spatial-context information, IRGS is advantageous since it is region-based, and by using the statistical properties of regions, it is less sensitive to speckle noise and the intra-class backscatter variability induced by incidence angle in SAR images [11]. Also, a region-based segmentation method is preferred in terms of computation speed as the number of regions/superpixels, which are used to construct region adjacency graph (RAG), is usually significantly less than the number of pixels [20].

IRGS, similar to other superpixel segmentation methods such as simple linear iterative clustering (slic) [27], preserves image boundaries by generating homogeneous superpixels that contain only one ground-truth class. However, a main advantage of IRGS is that IRGS is adaptive, i.e., it captures the important local details without having to utilize many superpixels in homogeneous regions. IRGS method models the backscatter based on Gaussian statistics and changes the initial boundaries from a watershed algorithm [28] by merging the regions to obtain the final segmentation image. A complex QP extension of IRGS called PolarIRGS has also been published and applied to a land cover type data

7

set [21]. PolarIRGS algorithm is performed here for sea-ice scene segmentation using reconstructed QP data from CP data. This contributes to utilizing all the information which can be extracted from a CP data set in a contextual segmentation.

Since the segmentation is unsupervised, a separately trained SVM model is used to assign true ice-type labels to the regions. SVM classification algorithm has already proven to be effective in discriminating between SAR signatures of ice and water [11, 29]. The segmentation maps are combined with the ice-type classification results obtained from the SVM algorithm to generate the final ice-type maps.

The proposed sea-ice type classification method which combines the IRGS-based segmentation and the SVM classification is applied to assess the capability of CP SAR data in sea-ice type mapping compared to DP data. The performance of the classification method is tested using a pair of fine complex quad-polarization SAR scenes from which the CP data is derived (to mimic the RCM CP data).

Section 2.4 provides a literature review of the classification methods using CP SAR data. In Section 2.2, a review of CP SAR features is provided. A review on the methods of QP reconstruction from CP data is presented in Section 2.3. Section 4.4 presents the steps of the proposed methodology. Section 2.6 describes the study area and the data used in this chapter, and Section 2.7 presents the experiments and the corresponding results and analyses.

2.2   Compact Polarimetric SAR Theory

The polarization of an electromagnetic wave characterizes the behavior of its electric field. The polarization can be represented in general by the Jones vector $\underline{\mathbf{E}}$ [30]

$$\underline{\mathbf{E}} = A e^{j\alpha} \begin{bmatrix} \cos\psi\cos\chi - j\sin\psi\sin\chi \\ \sin\psi\cos\chi + j\cos\psi\sin\chi \end{bmatrix} \tag{2.1}$$

where A, ψ, and χ parameterize the "polarization ellipse", which is the trajectory of the electric field at a fixed location along the propagation direction. A is the ellipse amplitude, and ψ and χ are called the orientation angle and the ellipticity angle, respectively [31]. Also, the term α is an absolute phase term. The relationship between the incident field in radar $\underline{\mathbf{E}}_i$ and the backscatter field $\underline{\mathbf{E}}_s$ is described by [30]

$$\underline{\mathbf{E}}_s = \frac{e^{-jkr}}{r}\mathbf{S}\underline{\mathbf{E}}_i = \frac{e^{-jkr}}{r} \begin{bmatrix} S_{HH} & S_{HV} \\ S_{VH} & S_{VV} \end{bmatrix} \underline{\mathbf{E}}_i, \tag{2.2}$$

8

where $\mathbf{S}$ is the scattering matrix. The term r is the distance between the target and the radar antenna, and k is the wave number of the illuminating wave [32]. This is the case where the transmitting and receiving antennas are at the same location (monostatic backscattering case). Therefore, the incident and scattered Jones vector are expressed in the same orthogonal basis with horizontal (H) and vertical (V) unit vectors ($\hat{u}_H, \hat{u}_V$). In the case of a reciprocal propagation medium, the vector reciprocity theorem [32] requires that the matrix $\mathbf{S}$ be symmetric, with $S_{HV} = S_{VH}$.

A SAR system that provides a complete scattering matrix is called a full QP SAR. Despite the complete data source that a QP SAR provides, a QP SAR system requires a higher frequency of pulse repetition than that of a DP SAR to transmit and receive in two orthogonal polarizations. The pulse repetition frequency in QP system is twice the frequency as in a single or DP SAR for a given coverage area [4]. The data requirements restrict the use of fine QP SAR data in wide swaths when mapping vast expanses of ice/water in oceans, and make wide-swath dual- and, especially, CP modes more favorable.

The first application of CP is attributed to Souyris *et al.*[33], who proposed using "$\pi/4$-mode", and reconstructed full QP data. In this mode, in response to a linearly-polarized transmitted field with a 45° inclination, two coherent linear polarizations are received. The CTLR-CP mode [3], where a circular polarization on transmit is followed by two coherent orthogonal linear polarizations on receive, is another implementation of CP. This mode has been more appealing due to the simpler and more robust implementation than that of the other conventional coherent dual-polarized modes [4]. Raney *et al.* [34] described the properties of the hybrid-polarity modes and compared the CTLR mode with the other CP modes.

In the case of a CP SAR, a complex measurement vector $\underline{\mathbf{E}}$ of the backscattered field, which is the multiplication of scattering matrix ($\mathbf{S}$) and the transmit polarization is used

$$\underline{\mathbf{E}}_{CP} = \begin{bmatrix} E_H \\ E_V \end{bmatrix} = \mathbf{S}\underline{\hat{\mathbf{u}}}_t, \tag{2.3}$$

where $\underline{\hat{\mathbf{u}}}_t$ is the unit Jones vector associated with the transmit wave. For instance, according to (2.1), in the CTLR mode ($\psi = 0$, $\chi = -\frac{\pi}{4}$), the unit Jones vector is $\frac{1}{\sqrt{2}}[1 \quad -j]^T$, and therefore, $\underline{\mathbf{E}}_{CTLR}$ can be given by

$$\underline{\mathbf{E}}_{CTLR} = \begin{bmatrix} S_{HH} & S_{HV} \\ S_{HV} & S_{VV} \end{bmatrix} \begin{bmatrix} \frac{1}{\sqrt{2}} \\ \frac{-j}{\sqrt{2}} \end{bmatrix} = \frac{1}{\sqrt{2}} \begin{bmatrix} S_{HH} - jS_{HV} \\ S_{HV} - jS_{VV} \end{bmatrix}. \tag{2.4}$$

To characterize the scattering properties of a random medium using a CP SAR, the

2×2 Hermitian positive semidefinite coherence matrix ($\mathbf{J}$) given by multiplying $\underline{\mathbf{E}}$ by its complex conjugate transpose [32] is used

$$\mathbf{J} = \frac{1}{L} \sum_{i=1}^{L} \mathbf{E}_{CP} \underline{\mathbf{E}}_{CP}^{*T} = \begin{bmatrix} \langle |E_H|^2 \rangle & \langle E_H E_V^* \rangle \\ \langle E_V E_H^* \rangle & \langle |E_V|^2 \rangle \end{bmatrix} \tag{2.5}$$

where $< \cdots >$ shows temporal or spatial averaging, ^{T} represents the transpose operator, * indicates the complex conjugate, and L is the number of looks used for averaging. According to (2.4) and (2.5), the sample coherence matrix in the CTLR mode can also be given by

$$\begin{aligned} \mathbf{J} &= \frac{1}{2} \begin{bmatrix} \langle |S_{HH}|^2 \rangle & j \langle S_{HH} S_{VV}^* \rangle \\ -j \langle S_{VV} S_{HH}^* \rangle & \langle |S_{HH}|^2 \rangle \end{bmatrix} + \frac{\langle |S_{HV}|^2 \rangle}{2} \begin{bmatrix} 1 & -j \\ j & 1 \end{bmatrix} \\ &+ \frac{1}{2} \begin{bmatrix} -2\mathrm{Im}\left(\langle S_{HH} S_{HV}^* \rangle \right) & \langle S_{HH} S_{HV}^* \rangle + \langle S_{HV} S_{VV}^* \rangle \\ \langle S_{HH} S_{VV}^* \rangle + \langle S_{VV} S_{HV}^* \rangle & 2\mathrm{Im}\left(\langle S_{VV} S_{HV}^* \rangle \right) \end{bmatrix}. \end{aligned} \tag{2.6}$$

Consider the classical unitary Pauli matrix group [30]

$$\boldsymbol{\sigma_0} = \begin{bmatrix} 1 & 0 \\ 0 & 1 \end{bmatrix}, \quad \boldsymbol{\sigma_1} = \begin{bmatrix} 1 & 0 \\ 0 & -1 \end{bmatrix}, \quad \boldsymbol{\sigma_2} = \begin{bmatrix} 0 & 1 \\ 1 & 0 \end{bmatrix}, \quad \boldsymbol{\sigma_3} = \begin{bmatrix} 0 & -j \\ j & 0 \end{bmatrix}. \tag{2.7}$$

To represent CP data by real values, equation (2.5) can be decomposed as [30]:

$$\begin{aligned} \mathbf{J} &= \frac{1}{2} \{ S_0 \boldsymbol{\sigma_0} + S_1 \boldsymbol{\sigma_1} + S_2 \boldsymbol{\sigma_2} + S_3 \boldsymbol{\sigma_3} \} \\ &= \frac{1}{2} \begin{bmatrix} \langle S_0 + S_1 \rangle & \langle S_2 - jS_3 \rangle \\ \langle S_2 + jS_3 \rangle & \langle S_0 - S_1 \rangle \end{bmatrix} \end{aligned} \tag{2.8}$$

where the real-valued parameters $\{ S_0, S_1, S_2, S_3 \}$ form what is called the Stokes vector [32]

$$\begin{aligned} S_0 &= E_H E_H^* + E_V E_V^* = |E_H|^2 + |E_V|^2 \\ S_1 &= E_H E_H^* - E_V E_V^* = |E_H|^2 - |E_V|^2 \\ S_2 &= 2\mathrm{Re}(E_H E_V^*) \\ S_3 &= -2\mathrm{Im}(E_H E_V^*). \end{aligned} \tag{2.9}$$

The Stokes vector fully characterizes the backscattered field by four real parameters.

Table 2.1: List of CP features used in the ice-typing method.

Name	Description	#[1]
α_s	scattering mechanism parameter [35]	1
μ_c	circular polarization ratio [4]	1
u	conformity coefficient [7]	1
ρ	correlation coefficient of RH and RV [7]	1
δ	relative phase angle between RH and RV [4,7]	1
m	degree of polarization [18]	1
H_i	Shannon entropy, intensity component [7]	1
H_P	Shannon entropy, polarimetric component [7]	1
$m - \chi$	m-chi decomposition of CP data [18]	3
$m - \delta$	m-delta decomposition of CP data [4]	3
RH, RV	intensity values of RH and RV channels [36]	2
$S_0, ..., S_3$	Stokes vector components [37]	4

[1]This column indicates the number of features in each category.

The Stokes parameters can also be represented as a function of polarization ellipse parameters, i.e., A, ψ, χ [32]. Several quantitative features characterizing the backscattered field can be derived from the Stokes vector. The *degree of polarization*, *circular polarization ratio*, *relative phase*, *conformity coefficient*, and the *m-chi* decomposition features are examples of Stokes-vector-derived features. A list of some commonly-known CP SAR features is presented in Table 2.1.

2.3   QP Reconstruction from CP Data

For a QP SAR, in some cases (e.g., distributed targets [32]), the scattering matrix can not fully describe the scattering properties of all radar targets [31]. Therefore, the second-order target descriptors such as covariance matrix are needed. Assuming reciprocity in the monostatic radar case, 3×3 multilook complex covariance matrix is given by [30]

$$\mathbf{C} = \begin{bmatrix} \langle |S_{HH}|^2 \rangle & \sqrt{2} \langle S_{HH} S_{HV}^* \rangle & \langle S_{HH} S_{VV}^* \rangle \\ \sqrt{2} \langle S_{HV} S_{HH}^* \rangle & 2 \langle |S_{HV}|^2 \rangle & \sqrt{2} \langle S_{HV} S_{VV}^* \rangle \\ \langle S_{VV} S_{HH}^* \rangle & \sqrt{2} \langle S_{VV} S_{HV}^* \rangle & \langle |S_{VV}|^2 \rangle \end{bmatrix}, \quad (2.10)$$
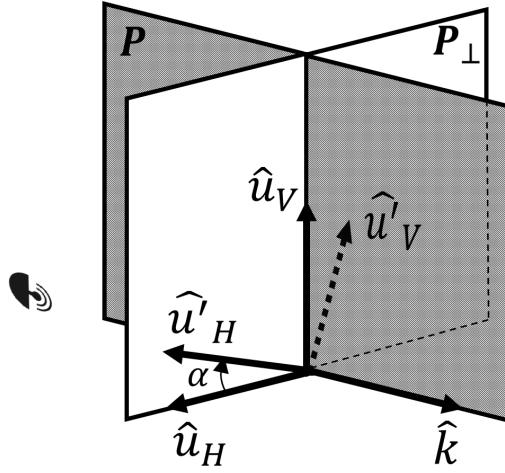
Figure 2.1: Traverse $P_\perp$ and incident P planes involved in reflection symmetry (This figure is based on Fig. 1 by Souyris *et al.* [38].)

which is a Hermitian positive semi-definite matrix, in which the main diagonal elements are the real-valued intensities of the polarimetric channels, and the off-diagonal elements represent their complex covariances.

The reconstruction of full QP from CP SAR data allows us to analyze the reconstructed QP (pseudo-QP) data using the state-of-the-art full polarimetric SAR classification methods [2]. To construct pseudo-QP 3×3 covariance matrix using 2×2 CP coherence matrix $\mathbf{J}_{CTLR}$, according to (2.10) and (2.6), there are four equations (using one complex J_{12} and two real measurements J_{11}, J_{22}) and nine unknown variables (three real elements C_{11}, C_{22}, C_{33}, and three complex ones C_{12}, C_{13}, and C_{23}). To solve this underdetermined system of equations, some assumptions regarding the symmetry of geophysical media have been made [38, 39]. A review of reconstruction methods is provided next.

The first QP reconstruction method is proposed by Souyris *et al.* [38] where they made two symmetry assumptions. The first assumption is reflection symmetry [38, 40]. Assume the linear orthogonal basis $(\hat{\mathbf{u}}_H, \hat{\mathbf{u}}_V)$ in Fig. 2.1 is oriented such that $(\hat{\mathbf{u}}_H \perp P)$ and $(\hat{\mathbf{u}}_V \parallel P)$ where P is the plane containing the incident wave $\hat{k}$ and $P_\perp$ is the traverse plane which is normal to the incident wave. Reflection symmetry occurs where the target is symmetrical about the plane P. Geophysical media such as ocean water, forest, snow, and sea-ice can have reflection symmetry properties [38]. With this type of symme-

---

[2]As will be discussed later in this section, the symmetry assumptions that are made to reconstruct the 3×3 full QP covariance matrix from a 2×2 CP coherence matrix coerce the QP covariance matrix to be sparse. Therefore, not all the QP classification methods will be applicable using pseudo-QP data.

try, the correlation between the co- and cross-pol coefficients is approximated to be zero, $\langle S_{HH}S_{HV}^* \rangle = \langle S_{HV}S_{VV}^* \rangle = 0$. Accordingly, the covariance matrix is formed as [40]

$$\mathbf{C} = \begin{bmatrix} \langle |S_{HH}|^2 \rangle & 0 & \langle S_{HH}S_{VV}^* \rangle \\ 0 & 2\langle |S_{HV}|^2 \rangle & 0 \\ \langle S_{VV}S_{HH}^* \rangle & 0 & \langle |S_{VV}|^2 \rangle \end{bmatrix}, \tag{2.11}$$

and the CTLR coherence matrix with this assumption is given by

$$\mathbf{J}_{CTLR} = \frac{1}{2} \begin{bmatrix} \langle |S_{HH}|^2 \rangle + \langle |S_{HV}|^2 \rangle & j\left(\langle S_{HH}S_{VV}^* \rangle - \langle |S_{HV}|^2 \rangle\right) \\ -j\left(\langle S_{HH}S_{VV}^* \rangle - \langle |S_{HV}|^2 \rangle\right) & \langle |S_{VV}|^2 \rangle + \langle |S_{HV}|^2 \rangle \end{bmatrix} \tag{2.12}$$

Rotation symmetry is another type of scattering symmetry. For a target with rotation symmetry around the incident wave, covariance matrix coefficients are invariant to the rotation of the orthogonal basis $(\hat{\mathbf{u}}_H, \hat{\mathbf{u}}_V)$ by any arbitrary angle α (see Fig. 2.1). Under rotation symmetry assumption, Nghiem *et al.* (equations (34)-(38) [40]) provide a set of equations which relate the scattering coefficients

$$\langle |S_{HH}|^2 \rangle = \langle |S_{VV}|^2 \rangle \tag{2.13}$$

$$\frac{\langle |S_{HV}|^2 \rangle}{\langle |S_{HH}|^2 \rangle} = \frac{\langle |S_{HV}|^2 \rangle}{\langle |S_{VV}|^2 \rangle} = \frac{1 - \rho_{HHVV}}{2},$$

$$\rho_{HHVV} = \frac{\langle S_{HH}S_{VV}^* \rangle}{\sqrt{\langle |S_{HH}|^2 \rangle \langle |S_{VV}|^2 \rangle}} \tag{2.14}$$

where ρ_{HHVV} is the correlation coefficient between S_{HH} and S_{VV}. The second assumption in Souyris's method is similar to (2.14) (or equivalently equation (41b) by Nghiem *et al.* [40]) with making differentiation between $\langle |S_{HH}|^2 \rangle$ and $\langle |S_{VV}|^2 \rangle$

$$\frac{\langle |S_{HV}|^2 \rangle}{\langle |S_{HH}|^2 \rangle + \langle |S_{VV}|^2 \rangle} = \frac{1 - |\rho_{HHVV}|}{4}. \tag{2.15}$$

Therefore, this assumption is not based on a complete rotation symmetry but only one condition of this type of symmetry. Souyris *et al.* derived (2.15) by linearly extrapolating between two limits: fully polarized and fully depolarized waves [38].

After making these assumptions, the system of equations can be iteratively solved to reconstruct QP covariance matrix [36, 38]. According to (2.12) and (2.14), the correlation

coefficient ρ_{HHVV} can be calculated by

$$\rho_{HHVV} = \frac{\langle|S_{HV}|^2\rangle - 2jJ_{12}}{\sqrt{(2J_{11} - \langle|S_{HV}|^2\rangle)(2J_{22} - \langle|S_{HV}|^2\rangle)}}, \tag{2.16}$$

and (2.15) can be rewritten as

$$\langle|S_{HV}|^2\rangle = \frac{(J_{11} + J_{22})(1 - |\rho_{HHVV}|)}{3 - |\rho_{HHVV}|}. \tag{2.17}$$

Initially, $\langle|S_{HV}|^2\rangle$ is set to zero and ρ_{HHVV} is calculated. Using this ρ_{HHVV} value, $\langle|S_{HV}|^2\rangle$ is calculated. The new value of $\langle|S_{HV}|^2\rangle$ is injected back into (2.16), and this loop is iterated until the difference between $\langle|S_{HV}|^2\rangle$ values from the current and previous iterations is less than a threshold. Whenever $|\rho_{HHVV}|$ becomes greater than one for a pixel, or the denominator of (2.16) is the square root of a negative value, $|\rho_{HHVV}|$ is set to 1 and $\langle|S_{HV}|^2\rangle = 0$ and the iterations are stopped [38]. After convergence, using the estimated value of $\langle|S_{HV}|^2\rangle$, we can form the reconstructed sample covariance matrix elements (2.11). Note that, as seen in Eq. (2.16), all the elements can be written in terms of $\langle|S_{HV}|^2\rangle$ and CP coherence matrix elements.

Nord $et\ al.$ [39] proposed a modified version of Souyris's reconstruction method. They demonstrated that the assumption (2.15) may not hold for some datasets. They used a QP scene from urban and forest areas and demonstrated that Eq. (2.17) is not a strict equality for terrain dataset [39]. Based on an inequality relating the arithmetic and geometric means of co-pol terms $\langle|S_{HH}|^2\rangle$ and $\langle|S_{VV}|^2\rangle$, they derived

$$\frac{\langle|S_{HV}|^2\rangle}{\langle|S_{HH}|^2\rangle + \langle|S_{VV}|^2\rangle} = \frac{1 - |\rho_{HHVV}|}{N}, \tag{2.18}$$

where the term N is given by

$$N = \frac{\langle|S_{HH} - S_{VV}|^2\rangle}{\langle|S_{HV}|^2\rangle}, \tag{2.19}$$

which the ratio of double-bounce backscatter ($\langle|S_{HH} - S_{VV}|^2\rangle$) to cross-pol power ($\langle|S_{HV}|^2\rangle$). The term N is the only difference between Nord's and Souyris's methods. The reconstruction algorithm then involves iterating between (2.16) and a modified version of (2.17) as

$$\langle|S_{HV}|^2\rangle = \frac{2(J_{11} + J_{22})(1 - |\rho_{HHVV}|)}{N + 2(1 - |\rho_{HHVV}|)}. \tag{2.20}$$

14

To start the iteration, N is initially set to 4, and the pseudo QP covariance matrix is reconstructed. The value N is then estimated from (2.19) using the reconstructed covariance matrix elements, and used for reconstructing the new pseudo QP covariance matrix afterwards. Note that the following equation holds [3]

$$\langle |S_{HH} - S_{VV}|^2 \rangle = \langle |S_{HH}|^2 \rangle + \langle |S_{VV}|^2 \rangle - 2\text{Re}(\langle S_{HH} S_{VV}^* \rangle). \tag{2.21}$$

Espeseth *et al.* [17] proposed two methods to estimate the cross-pol term $\langle |S_{HV}|^2 \rangle$: one based on the degree of polarization (DoP), and the other based on the eigenvalues of CP sample coherence matrix. In the DoP-based approach, the depolarized power is related to the cross-pol intensity term. The authors assume that all the response power generated in the cross-pol channel $\langle |S_{HV}|^2 \rangle$ originates from the depolarization effects. Accordingly, the surface scattering is assumed to have no contribution to the cross-pol channel power [17]. The cross-pol term $\langle |S_{HV}|^2 \rangle$ is assumed to be related to the power of depolarized scattering mechanism P_d as

$$\langle |S_{HV}|^2 \rangle = \frac{1}{2} P_d = \frac{1}{2}(1 - DoP)S_0,$$
$$DoP = \frac{\sqrt{S_1^2 + S_2^2 + S_3^2}}{S_0} \tag{2.22}$$

where $S_0, \ldots S_3$ are the elements of the Stokes vector. By estimating $\langle |S_{HV}|^2 \rangle$, the pseudo QP covariance elements can be calculated from (2.11) and (2.12). The main limitation of the approach is the assumption of assigning all the cross-pol intensity to the depolarized power [17]. The eigenvalue (Eig)-based method attempts to find the fraction of the total power of the backscattered wave that belongs to the cross-pol intensity

$$2 \langle |S_{HV}|^2 \rangle = \gamma S_0, \tag{2.23}$$

where the term γ is proposed to be approximated by the ratio of two eigenvalues of the sample coherence matrix $\mathbf{J}$, λ_1, λ_2

$$\gamma = \frac{\lambda_2}{\lambda_1},$$
$$2\lambda_1 = S_0 + \sqrt{S_1^2 + S_2^2 + S_3^2}, \qquad 2\lambda_2 = S_0 - \sqrt{S_1^2 + S_2^2 + S_3^2}. \tag{2.24}$$

---

[3] This equation holds for any pair of complex values such as S_{HH} and S_{VV}. This equality has also been used in Eq. (B5) in the work by Nord *et al.* [39]. Also, as noted by Collins *et al.* [41], the term $(1 - |\rho|)$ in Eq. (B5) [39] is misplaced and should be moved to the beginning of the last line.

Therefore, according to (2.23) and (2.24), the cross-pol intensity is given by

$$\left\langle |S_{HV}|^2 \right\rangle = \frac{(1 - DoP)}{2\,(1 + DoP)}\,S_0, \tag{2.25}$$

As compared to the Souyris's and Nord's methods, the DoP-based and Eig-based reconstruction methods noticeably execute faster. Therefore, the cross-pol intensity values estimated from the DoP- and eigenvalue-based methods can be used as the initial value for the Souyris's and Nord's method.

2.4 Intelligent Systems for Satellite Scene Interpretation Using CP SAR Data

In this section, a brief review of the recent work in SAR scene classification using CP data is presented. Then, the CP SAR classification methods specifically for sea-ice mapping are described. Existing classification algorithms using CP SAR data can be divided into two categories: classification algorithms using reconstructed full QP data from CP data or features derived directly from CP data.

In the first category, the quad-polarimetric covariance matrix is estimated from CP data [38], producing a pseudo-QP covariance matrix that can be used with QP scene classification methods. Souyris *et al.* [38] proposed the reconstruction of QP data from CP data and used the reconstructed QP data in crop field classification. They presented the full-scene classification images as well as the quantitative results of the classification, and showed the high level of information content preserved in the pseudo-QP data as compared with the QP data. Ainsworth *et al.* [42] demonstrated that pseudo-QP data generated from CP provides almost the same result of the classification of crop fields and forested areas as those directly from CP data.

Li *et al.* [43] proposed a QP reconstruction method that is suited to the oil spill detection on water surface where Bragg scattering is assumed to be dominant. In a work by Collins *et al.* [44], an oil-water mixing index is derived from the reconstructed QP data for oil spill characterization. In a more recent study, Zhang *et al.* [45] used the reconstructed co- and cross-pol coefficients from CP data to calculate the relative phase parameter, and proposed an unsupervised classification scheme to distinguish oil slicks from ocean water.

In the second category, the features derived from the Stokes vector such as decomposition features [3, 35] are used in classification. A multifrequency analysis of tropical

vegetation classification utilizing CP data was done by Lardeux *et al.* [46]. An SVM classification using CP data was performed by Souissi *et al.* [47] to classify different types of land cover. In another study [48], after extracting two main sets of features (one directly from CP covariance and the other from the pseudo-QP covariance data each in different CP modes), Aghabalaei *et al.* performed an SVM classification on a feature set selected by a genetic algorithm to classify forest species. CP data was also utilized for other applications of classification, such as lake-ice breakup monitoring using a thresholding scheme on a number of CP features derived from Stokes vector data [49] and rice monitoring using a decision-tree classification [50].

Shirvany *et al.* [51], used the CP degree of polarization parameter for discriminating man-made objects and oil spills from the sea surface in different CP modes. Salberg *et al.* [52] derived a coherence measure from CP data under a two-scale Bragg scattering model, and demonstrated that this retrieved parameter from CP performs well in suppressing lookalikes in oil spill detection. They also evaluated a number of CP-derived measures in oil spill detection [52].

There have been other studies where based on either sea surface scattering in terms of surfactants and wind conditions [53], or a physical scattering model called X-Bragg [54], a number of parameters extracted from CP data were evaluated in distinguishing oil spills from lookalikes. In another study by Buono *et al.* [55], the X-Bragg scattering model have been used to compare two CP modes with full QP SAR data based on the performance of three parameters derived from both CP coherence and QP covariance data.

Given the recent developments in CP for earth resource management, there are limited papers that consider its use for sea-ice type classification. Dabboor *et al.* [7] applied a maximum likelihood classifier trained and tested using selected pixels from the same image (i.e., not a full scene classification). They analyzed the capability of CP features to distinguish open water, first-year ice, and multi-year ice. Zhang *et al.* [15] investigated different CP modes for sea-ice classification. They also determined the type of CP mode that leads to the highest reconstruction accuracy of a number of polarimetric features. Geldstezer *et al.* [9] used 26 derived CP features and assessed their discrimination capability for different sea-ice types. These studies indicated the most useful set of CP-derived features for sea-ice classification.

An analysis of the performance of m-chi decomposition parameters extracted from CP data in distinguishing between sea-ice types was done by Li *et al.* [16] and the results were compared with those obtained using classic decomposition parameters, entropy and scattering angle, which are extracted from the true QP SAR data. Decomposition results were discussed in a quantitative manner, however, no classification was performed. Espeseth *et*

17

al. [17] proposed two new methods for reconstructing pseudo-QP data from CP data. The methods are based on degree of polarization and eigenvalues of the CP covariance matrix. The authors investigated the performance of their proposed reconstruction methods compared with Souyris's method [38] depending on the frequency of radar. In a recent study by Singha *et al.* [14], 21 polarimetric features extracted from RISAT-1 CP SAR data were ingested into an artificial neural network classifier to differentiate sea-ice types. Full scene classification images as well as a feature information content analysis were reported in the paper. Only a pixel-level classification was performed without using any spatial context.

To the best of our knowledge, there is no CP SAR sea-ice publication that performs full scene classification with multiple classes and using spatial context. Our approach in this chapter is a region-based segmentation integrated with SVM classification to provide full scene, multi-class classification using CP data. Results of our algorithm are compared to those when using DP and full QP data in the same context.

2.5   Classification System

The components of the sea-ice type classification methodology are described in this section. After an overview of the proposed method, the details of the segmentation approach, labeling method, and, finally, the method of combining segmentation and labeling results are provided.

2.5.1   Overview

The ice-type classification methodology consists of three components as shown in Fig. 2.2. The input data for the algorithm consists of the acquired SAR scene with the landmask associated with the scene and trained labeling model. The landmask file is a binary image that masks the land pixels. The labeling model is trained using the training sample data collected from the SAR data set. The algorithm starts with a segmentation process of the SAR data which is shown in the left part of Fig. 2.2. Unsupervised IRGS segmentation approach [11, 20, 21] is used to identify homogeneous regions of ice types. The details of IRGS segmentation approach for real-valued and complex-valued SAR data are described in Section 2.5.2.

Since the segmentation process is unsupervised, the initial labels associated with the regions are arbitrary, and do not correspond to ice types. Therefore, a pixel-based SVM classification that was trained using a list of SAR features is applied to label the CP SAR
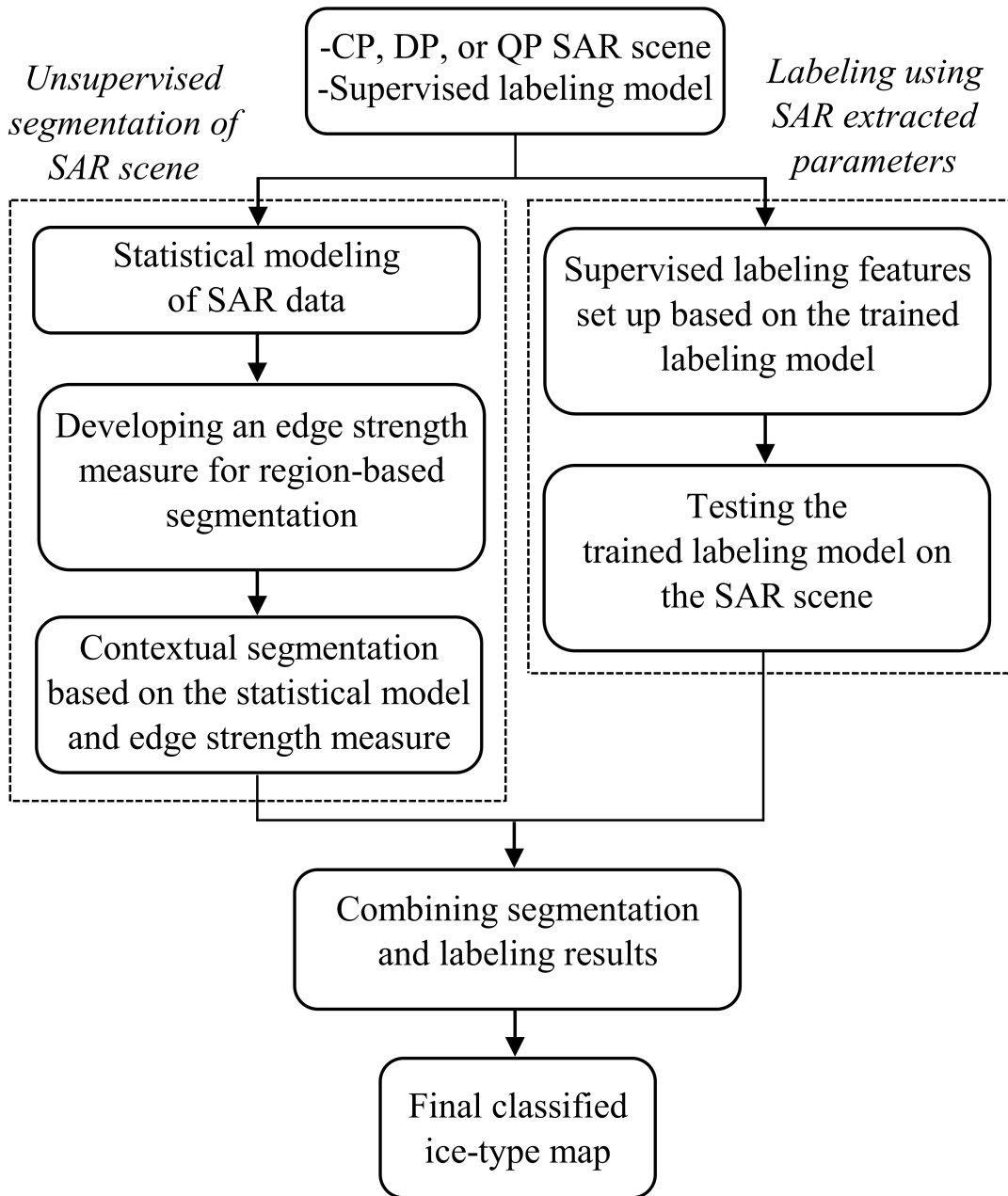
Figure 2.2: General block diagram of the proposed sea-ice classification approach.

scene under analysis. This step is shown in the right part of the block diagram of Fig. 2.2, and is independent of the unsupervised IRGS segmentation. The SVM labeling step is described in Section 2.5.3. The IRGS segmentation and SVM labeling are then combined in a majority-voting process explained in Section 2.5.4. Using this combination, the contextual information provided by IRGS is used to improve the noisy results of the SVM labeling method. The final results of the ice-type classification method is a classification map of different ice types.

The problem of image segmentation using IRGS is described next. First, we consider the segmentation of real-valued SAR satellite data. Afterwards, the segmentation problem formulation for complex full QP SAR data is provided. The labeling method is explained at the end of this section.

2.5.2   Unsupervised segmentation

The capability of reducing the impact of intra-class variations in an image, which can be a serious problem when dealing with wide-swath SAR scenes, using the spatial context information makes MRF-based segmentation beneficial. A region-based solution to the MRF-based segmentation is obtained by a region-growing method that keeps merging regions in a pre-oversegmented image in an iterative manner. The algorithm is called IRGS [20]. IRGS has been successfully used for sea-ice classification using SAR imagery [12, 26, 56–59]. Polarimetric IRGS (PolarIRGS), which is the IRGS extension for complex QP data, was created by Yu *et al* . [21]. In this chapter, we analyze the use of PolarIRGS for sea-ice type classification. Since the input data to PolarIRGS algorithm is complex QP covariance matrix, the *pseudocovariance* matrix, which is reconstructed from complex CP coherence matrix, is used here.

Segmentation of real-valued CP SAR data

This section describes the image segmentation problem using a SAR image that contains real numbers for each pixel. The image can include a scalar (e.g., a CP SAR intensity image) or a vector of real numbers for each pixel (e.g., different CP channel intensity images). Assuming $\mathcal{S}$ indicates the two-dimensional lattice (i.e., the image) and $s \in \mathcal{S}$ denotes a site on the lattice (i.e., an image pixel), let $\mathbf{X} = \{X_s | s \in \mathcal{S}\}$ be a set of discrete-valued random variables with each X_s having a value from $\mathcal{L} = \{1, ..., C\}$ that indicates the set of labels for the pixels. Therefore, the image is to be segmented into C classes. Also, let $\mathbf{Y} = \{\mathbf{Y}_s | s \in \mathcal{S}\}$ be a random field on $\mathcal{S}$. $\mathbf{Y}_s$ represents the measurement vector

at site s. Given $\mathbf{x} = \{x_s | x_s \in \mathcal{L}, s \in \mathcal{S}\}$ and $\mathbf{y} = \{\mathbf{y}_s | s \in \mathcal{S}\}$ as the realizations of $\mathbf{X}$ and $\mathbf{Y}$, respectively, the image segmentation process estimates a solution $\mathbf{x}$ given image $\mathbf{y}$.

IRGS, as a region-level segmentation method, is based on the region adjacency graph (RAG) representation of an image [20]. A RAG is defined by $\mathcal{G} = (\mathcal{V}, \mathcal{E})$ where $\mathcal{V}$ and $\mathcal{E}$ represent the set of vertices and arcs, respectively. Each vertex $v \in \mathcal{V}$ denotes an image region with $\mathcal{S}_v$ indicating the set of image sites inside that region. Also, each arc $e \in \mathcal{E}$ determines the boundary between two adjacent regions. The random field configuration based on region-level representation is defined as $\mathbf{X}^r = \{X_v^r | X_v^r \in \mathcal{L}, v \in \mathcal{V}\}$, with the superscript "$r$" indicating the region-level definition. IRGS, as an MRF-based approach, assumes $\mathbf{x}^r = \{x_v^r | x_v^r \in \mathcal{L}, v \in \mathcal{V}\}$ is a realization of $\mathbf{X}^r$ and attempts to find the optimal label field configuration $\mathbf{x}^{r*}$ that satisfies [20]

$$\mathbf{x}^{r*} = \arg \max_{\mathbf{x}^r \in \mathbf{X}^r} p(\mathbf{y}|\mathbf{x}^r)P(\mathbf{x}^r) \tag{2.26}$$

where $p(\mathbf{y}|\mathbf{x}^r)$ is the conditional probability density function of the observed image $\mathbf{y}$ given the label field configuration $\mathbf{x}^r$ and $P(\mathbf{x}^r)$ is the probability of a specific label field configuration $\mathbf{x}^r$. $p(\mathbf{y}|\mathbf{x}^r)$ and $P(\mathbf{x}^r)$ are respectively called the feature model, which models the distribution of features, and the spatial context model, which models the distribution of $\mathbf{x}^r$. Under class conditionally independent assumption, $p(\mathbf{y}|\mathbf{x}^r)$ is given by

$$p(\mathbf{y}|\mathbf{x}^r) = \prod_{i=1}^{C} \prod_{\mathcal{S}_v \in \Omega_i} \prod_{s \in \mathcal{S}_v} p(\mathbf{y}_s | x_v^r = i) \tag{2.27}$$

where the term $p(\mathbf{y}_s | x_v^r)$ is the probability of obtaining value $\mathbf{y}_s$ assuming the site s belongs to the class specified by x_v^r. Any configuration includes C disjoint subsets $\Omega_1 \ldots \Omega_C$, where Ω_i indicates the regions with class label i. $P(\mathbf{x}^r)$ follows the Gibbs distribution [19,58] and sums up the clique potentials over all possible cliques in $\mathcal{S}$ according to the specific MRF model chosen [19]. To solve equation (2.26), it is converted into an energy function and, therefore, the products are changed into sums

$$\mathbf{x}^{r*} = \arg \min_{\mathbf{x}^r \in \mathbf{X}^r} E_f(\mathbf{y}, \mathbf{x}^r) + E_s(\mathbf{x}^r) \tag{2.28}$$

where $E_f(\mathbf{y}, \mathbf{x}^r)$ and $E_s(\mathbf{x}^r)$ correspond to the feature model and the spatial context model, respectively. Based on the multivariate Gaussian distribution, as extensively used in the

SAR sea-ice segmentation literature [11, 20, 26, 60], $E_f(\mathbf{y}, \mathbf{x}^r)$ is defined as

$$E_f(\mathbf{y}, \mathbf{x}^r) = \frac{1}{n} \sum_{i=1}^{C} \sum_{\mathcal{S}_v \in \Omega_i} \sum_{s \in \mathcal{S}_v} \{\frac{1}{2}\log|\boldsymbol{\Sigma}_i| + \frac{1}{2}(\mathbf{y}_s - \mathbf{u}_i)^T \boldsymbol{\Sigma}_i^{-1}(\mathbf{y}_s - \mathbf{u}_i)\} \qquad (2.29)$$

where $\mathbf{u}_i$ and $\boldsymbol{\Sigma}_i$ denote mean vector and covariance matrix of class i. To calculate the spatial context model energy term $E_s(\mathbf{x}^r)$, IRGS uses the multi-level logistic (MLL) model [19] with a difference that IRGS incorporates an edge penalty function [20]

$$E_s(\mathbf{x}^r) = \beta \sum_{i=1}^{C-1} \sum_{j=i+1}^{C} \sum_{s \in \partial\Omega_i \cap \partial\Omega_j} g(\nabla_s) \qquad (2.30)$$

where $g(\nabla_s)$ is the edge penalty term, and $\partial\Omega_i$ denotes all the boundary sites that separate the regions assigned to class i from other regions. The term $\partial\Omega_i \cap \partial\Omega_j$ determines the shared boundary sites between classes i and j. The parameter β determines the weight of spatial context model with larger β leading to smoother segmentation. Adding $g(\nabla_s)$ to the spatial context model, IRGS penalizes each boundary site s based on the amount of $g(\nabla_s)$, a monotonically decreasing function of the edge strength ∇_s. This approach attempts to assign adjacent regions to the same class only when the strength is weak [20].

IRGS algorithm starts with an oversegmentation using watershed algorithm [28]. Then, it assigns each node a label using K-means algorithm to initialize the algorithm. After that, based on a merging criterion ∂E [58] that is the configuration energy difference computed according to the equation (2.28) before and after merging for each pair of regions and merges the pair with the most negative ∂E. This semantic region growing technique only tests the regions that belong to the same class and have shared boundaries [20]. The merging continues until no more negative ∂E remain or the maximum number of iterations is achieved. The final output is an unsupervised segmentation map of the scene with C arbitrary classes.

Segmentation of complex pseudo-QP SAR data

The image segmentation problem with full QP complex covariance data using PolarIRGS algorithm is explained hereafter. Let $\mathbf{Q}_s = \sum_{i=1}^{L} \underline{\boldsymbol{\Omega}}_i \, \underline{\boldsymbol{\Omega}}_i^{*T}$ be the full QP complex measurement at the site s. The matrix $\mathbf{Q}_s$ has a complex Wishart distribution [61]. Based on

Wishart distribution as the feature model, we have

$$p(Q_s|x_v^r = i) = \frac{(\det(\mathbf{Q}_s))^{L-d} \quad \exp\left[-\text{tr}\left(\mathbf{C}_i^{-1}\mathbf{Q}_s\right)\right]}{\pi^{\frac{1}{2}d(d-1)}\Gamma(L)\dots\Gamma(L-d+1)|\mathbf{C}_i^L|}$$ (2.31)

which corresponds to $p(\mathbf{y}_s|x_v^r = i)$ in (2.27). Here, $\det(\cdot)$ is the determinant operator, tr is the trace of a matrix, and Γ is the Gamma function. $\mathbf{C}_i$ is the ith class covariance matrix which is estimated by taking the average of training covariance matrix samples from class i. The value d is the number of elements in the vector $\mathbf{\Omega}$ ($d = 3$ under reciprocity assumption). By substituting (2.31) into (2.27), Yu *et al.* derived [21]

$$E_f(\mathbf{y}, \mathbf{x}^r) = \sum_{i=1}^{C} \sum_{\mathcal{S}_v \in \Omega_i} \sum_{s \in \mathcal{S}_v} \{\ln|\mathbf{C}_i| + \text{tr}\left(\mathbf{C}_i^{-1}\mathbf{Q}_s\right)\}.$$ (2.32)

To measure the edge strength ∇_s in full QP data, two main sets of approaches were proposed by Yu *et al.* [21]. In the first set of approaches, they used gradient magnitude of either decomposition features or amplitudes of polarimetric channels HH, HV, and VV. Second set of approaches was using complex polarimetric edge strength measures, which as reported by Yu *et al.* do not show the consistency of the first approach in testing different full QP scenes and, therefore, they used the gradient magnitudes as the edge measure [21].

2.5.3 Supervised labeling

The labels associated with the regions in unsupervised segmentation results are arbitrary and do not represent the actual ground truth ice type labels. A supervised classification has to be performed to assign the regions labels associated with the different ice types. The SVM classification has proven to be beneficial in sea-ice classification using SAR images [11]. The SVM classifier is designed to seek the boundary that provides maximum margin between a subset of training samples called support vectors in a high-dimensional space. Let x be the test feature vector to be classified and x_i be the support vectors. The SVM decision function is given as

$$f(x) = \sum_{\forall i} \alpha_i y_i K(x_i, x)$$ (2.33)

where $y_i \in \{-1, 1\}$ are the labels associated with the support vectors, α_i are the Lagrange multipliers, and $K(x_i, x)$ is the kernel function. After solving this optimization problem by

formulating it as a dual-Lagrangian problem [62], the classification label can be defined for any test vector. Non-linear decision boundaries suited to the non-linear SAR signatures of ice types, short training time, and quick testing of a trained SVM on a large SAR scene are among the advantages of the SVM classifier. However, SVM alone lacks the spatial context information and does generate spatially noisy results. As a result, we combine the SVM pixel-level labeling results with the unsupervised segmentation results to incorporate contextual information into the SVM.

2.5.4   Combining segmentation and labeling

By performing IRGS segmentation, we identify the regions for different ice types. To assign real labels to the regions, the region-based IRGS segmentation and pixel-based SVM labeling results are combined. We perform a majority voting of the SVM class labels for each region in the segmentation results. In particular, the number of pixels assigned to each class of ice types by SVM within a region is counted and the label associated with the maximum number of pixels is assigned to the region. Similar majority voting schemes have been used in the literature [63–65]. Alternatively, one can perform an aggregation function, such as *average* or *median*, for the features associated with the pixels within each region, and, afterwards, apply the trained SVM on the aggregated feature set to determine the region label. Since the feature set calculated through the aggregation process might not be a good representative for the whole region, the majority voting method is preferable. However, using an aggregated feature set when combining IRGS segmentation and SVM labeling results has the advantage of lower computation than using majority voting. This is because applying the trained SVM model to each region (as per the aggregate method) is faster than applying to each pixel in the scene (as per the majority voting method).

The overall ice-typing algorithm using CP data is described below (see Fig. 2.2):

1. RH and RV channel intensity images as well as other CP features for the SAR scene are extracted. The CP coherence matrix, which is derived from the Stokes vector elements using (2.8), is used to reconstruct QP data.

2. PolarIRGS is used to perform unsupervised segmentation using the reconstructed QP data.

3. The trained SVM classifier is used to label the scene pixels with four different ice types. Note that all the CP features are used for training the SVM classifier.

4. The IRGS and SVM results are combined leading to the final ice-typing map.
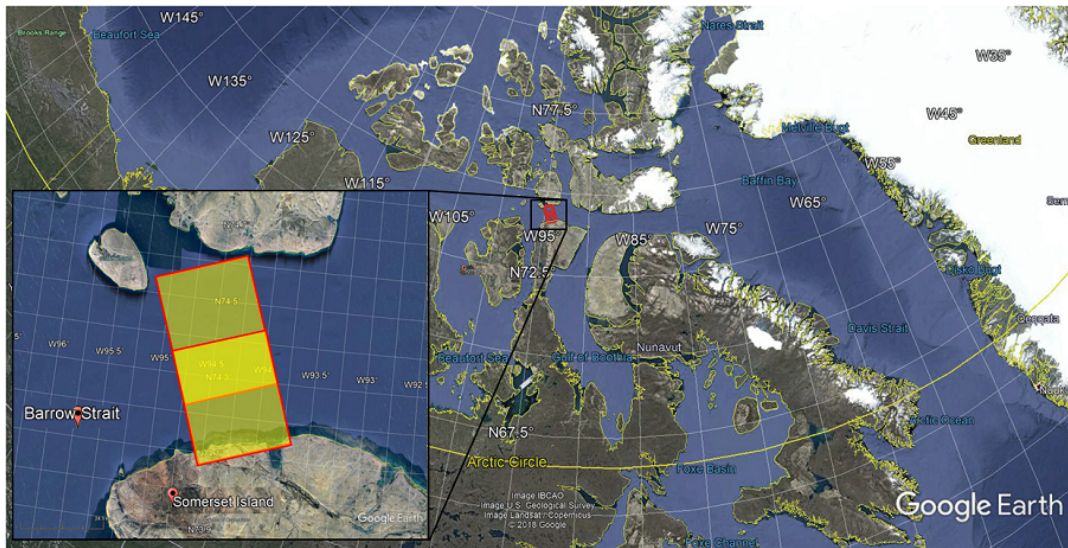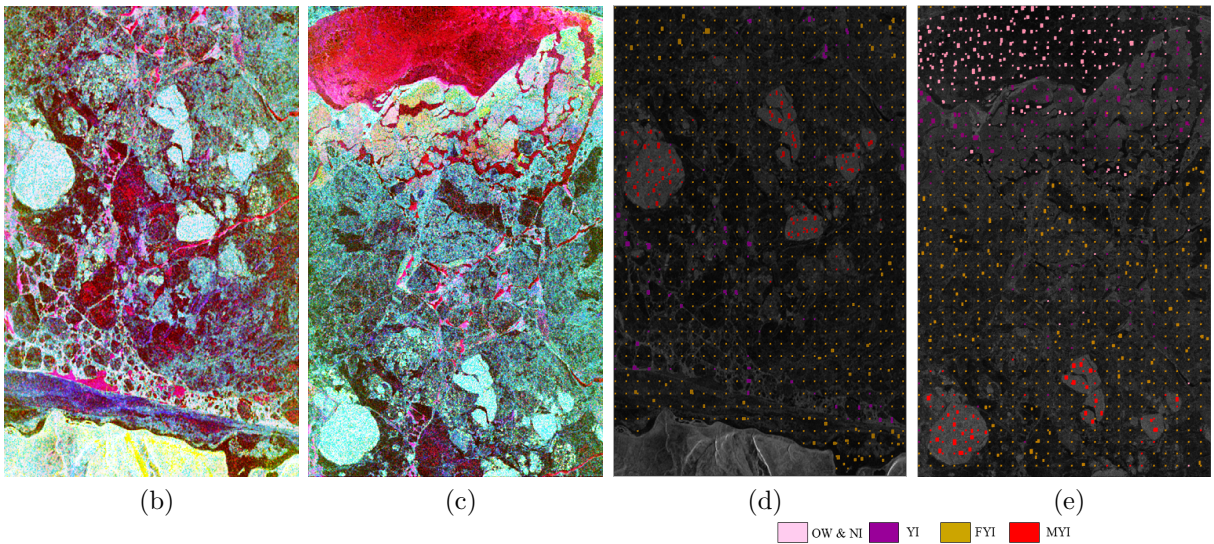
Figure 2.3: (a) The locations of the two RADARSAT-2 fine QP scenes in the Barrow Strait. Scenes (b) 231156 and (c) 231158 images in m-chi RGB composite along with (d)-(e) the images of the first element of Stokes vector with the ground truth overlaid. As presented in the legend, the samples of the classes OW & NI, YI, FYI, and MYI are shown with colors pink, purple, green, and red, respectively.

Table 2.2: The number of training and testing samples.

Name	Description	# of train	# of test
OW/NI	open water and new ice	5183	5227
YI	young ice	5889	5575
FYI	first-year ice	6396	6067
MYI	multi-year ice	5750	5637

The performance of the proposed method using CP data is compared with the cases where DP, and the original QP data are used. The description of the test data set used in this chapter is provided next.

2.6 Study Area and Data Set

The study area is the Barrow Strait, located near Somerset Island in the Canadian Arctic. We used two RADARSAT-2 fine quad-polarized images acquired over the area with a time difference of only two seconds identified as 231156 and 231158 (see Fig. 2.3(a)). Scene 231156 is used by Dabboor *et al.* [7] to train a maximum likelihood classifier with selected pixels and test on another set of selected pixels. The data were collected on May 5, 2010 at an incidence angle range between 30.30° and 32.00° for the first scene, and 30.20° and 31.99° for the second one. The sampled pixel and line spacing for the data sets were 4.73m and 5.61m, respectively.

The area covers approximately 23km by 14km, and contains open water and different ice types including new ice, young ice, first-year ice, and multi-year ice, identified by experts in the Canadian Ice Service. Roughly, 1000 samples per scene are identified by the CIS experts. Based on the samples acquired by the CIS experts, we collected the remaining samples for the classes. In the experiments, we have ensured that no pixels in the training set are included in the test set, and no pixels in the test set are included in the training set. The number of training and testing sample data for each class are presented in Table 2.2.

Four classes considered in this study are as follows: (1) open water and new ice (OW/NI), (2) young ice (YI), (3) first-year ice (FYI), and (4) multi-year ice (MYI). The classes OW and NI were combined because their backscatter signatures are very similar. Scene 231156 is used for training and scene 231158 used for testing. Since scene 231156 had

insufficient OW/NI samples, independent training and test data for OW/NI were obtained from scene 231158.

Fig. 2.3 (a)-(b) depicts the m-chi decomposition color-coded images [18] of the two scenes, where Red indicates double-bounce, Blue corresponds to single-bounce (and Bragg), and Green is related to random volume scattering [18]. The ground truth labeled sample data are also overlaid on the images of the first element of Stokes vector, S_0, which represents the total power of the backscatter field [30], and shown in Fig. 2.3 (c)-(d).

2.7   Experimental Results

The ice-type classification results are presented in this section, and the performance of the classification is discussed for four cases:

Case 1: DP HH and HV channel intensity images as input to original IRGS and SVM labeling methods

Case 2: CP RH and RV channel intensity images as input to original IRGS and SVM labeling methods

Case 3: complex pseudo-QP data as input to PolarIRGS method and CP-derived features (2.1) as input to SVM labeling method

Case 4: complex QP data as input to PolarIRGS and QP-derived features (2.5) as input to SVM labeling method.

The intention is to assess the capability of CP data as compared to those of DP and QP data in discriminating between different ice types, and evaluate whether using all the information inherent in CP data including the Stokes vector and its derived features can lead to more accurate results than those obtained using only intensities. To setup the input data, an RCM-data simulator [4] was used. The simulator extracts the CP coherence matrix from the QP scattering matrix, and based on the data specifications in each beam mode of the RCM, the coherence matrix is resampled. The Stokes vector is then extracted from the resampled coherence matrix. A box-car averaging filter is applied on the Stokes vector elements resulting in the final Stokes vector that is used to derive features [66]. Here, the CP products are derived in the medium resolution RCM mode with the pixel spacing equal to 50m $\times$ 50m (range$\times$azimuth). Also, the averaging filter window size is

(a) HH intensity   (b) HV intensity   (c) DP segmentation   (d) QP segmentation

(e) RH intensity   (f) RV intensity   (g) CP (intensities) segmentation   (h) CP-derived pseudo-QP segmentation
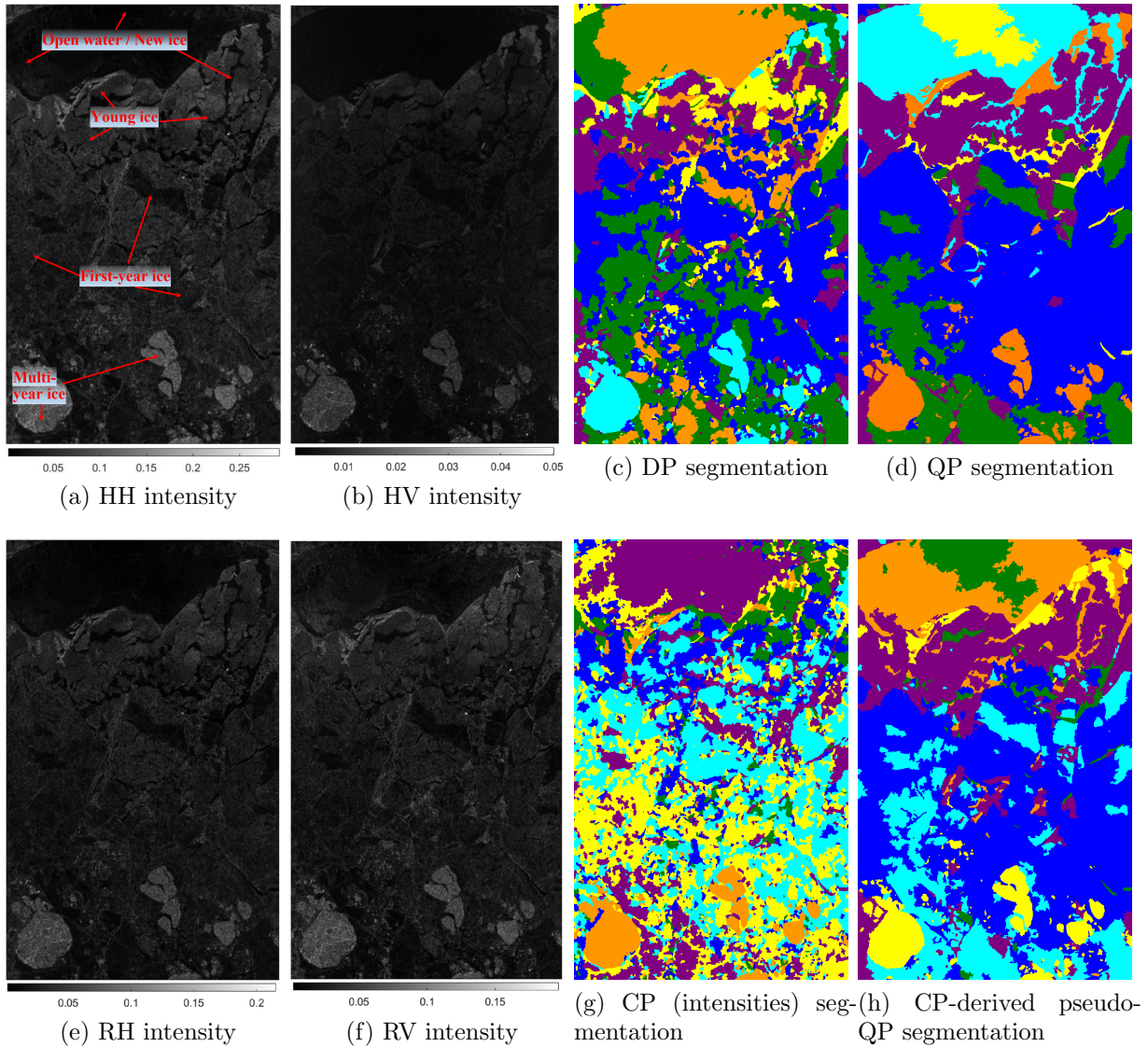
Figure 2.4: (a) HH and (b) HV channel intensity images together with the unsupervised IRGS segmentation of the scene 231158 using only HH and HV intensities, and (d) the segmentation image using original QP data. (e) RH and (f) RV channel intensity images together with the (g) IRGS segmentation of the scene 231158 using only RH and RV intensities, and (h) the segmentation image using pseudo-QP data derived from CP.

Table 2.3: Median and standard deviation values of errors for the reconstructed $|S_{HV}|^2$ values from CP relative to the original full QP $|S_{HV}|^2$ for the four reconstruction methods in the two SAR scenes.

Scene	Measure	Souyris [38]	Nord [39]	DoP-based [17]	Eig-based [17]
231156	Median	0.235	**0.012**	0.302	0.334
	Std. Dev.	0.265	0.256	0.174	**0.169**
231158	Median	0.300	**0.207**	0.213	0.255
	Std. Dev.	**0.306**	0.334	0.313	0.331

set to 9×9. The linear polarizations HH and HV are also extracted with the same pixel spacing and averaging filter size.

Using HH and HV intensity images for the linear DP case (Case 1), and RH and RV intensity images for the CP-intensities case (Case 2), the real-valued-based IRGS segmentation algorithm is applied. The segmentation results identify the ice-type regions and contain six arbitrary classes. The number of arbitrary classes in the IRGS segmentation does not correspond to the number of ice types since closed regions produced using the unsupervised segmentation are each assumed to be homogeneous and will be assigned a true class label via the labeling step. The number six for classes in segmentation was found to perform well in all cases, however, the results were insensitive to minor variations of this parameter. HH and HV, as well as RH and RV channel intensity images, and the corresponding IRGS image segmentation results are shown in Fig. 2.4 (a)-(c) and (e)-(g). The arbitrary nature of class labels is seen in these segmentation results as the class colors are different in two cases. The analysis of different QP reconstruction methods and the classification results are provided next.

2.7.1 QP data reconstruction results

Four reconstruction methods, namely Souyris's, Nord's, DoP-based, and Eig-based methods, that are described in Section 2.3, are analyzed here. The performance of the reconstruction methods in terms of the relative error $((|S_{HV}|^2_{QP} - |S_{HV}|^2_{CP})/|S_{HV}|^2_{QP})$ between the original full QP cross-pol term $|S_{HV}|^2$ values ($|S_{HV}|^2_{QP}$) and the reconstructed ones from CP ($|S_{HV}|^2_{CP}$) for all the image pixels is assessed. The reason for choosing the cross-pol term is that $|S_{HV}|^2$ is the most important term in the reconstruction process since when the value of $|S_{HV}|^2$ is known, the QP covariance matrix can be reconstructed (see Section 2.3 and the work by Souyris *et al.* [38] for more details).
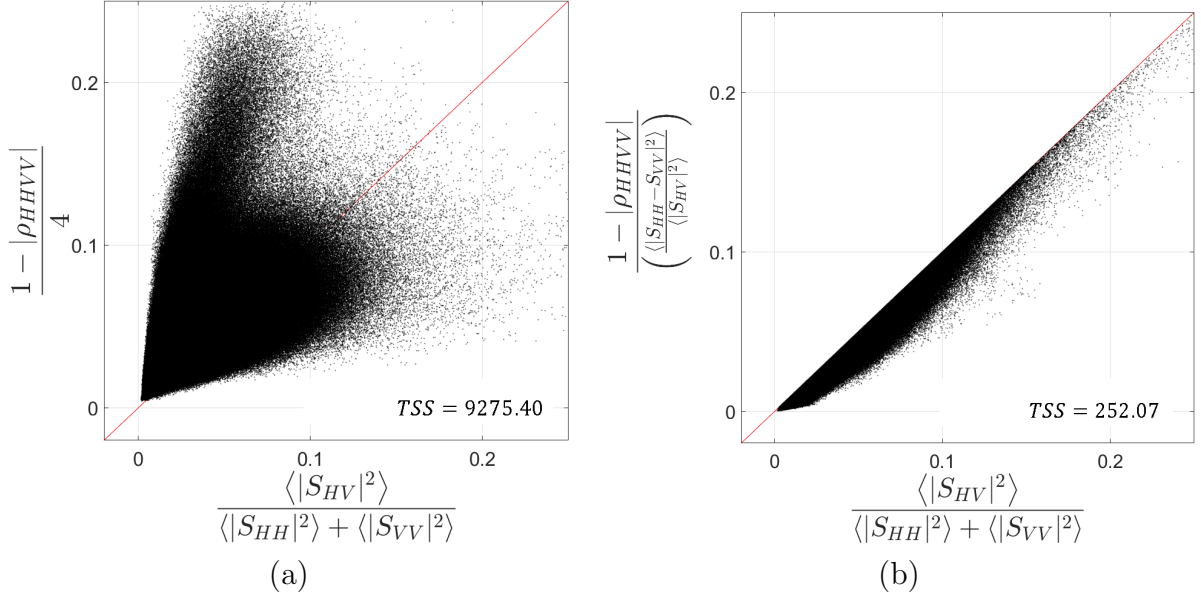
Figure 2.5: Scatter plots of the two sides of the equations considered as the second assumption in the (a) Souyris's (equation (2.15))and (b)Nord's (equation (2.18)) methods. The compactness of the data points around the red diagonal line indicates the level of accuracy of each assumption in the reconstruction methods. The values on the two sides for each case are calculated using the original QP data.

Table 2.3 reports on the median and standard deviation values for the error in all image pixels between the original and reconstructed $|S_{HV}|^2$ for the two scenes 231156 and 231158. As seen in Table 2.3, using Nord's reconstruction method, the lowest median relative errors is obtained among all the reconstruction methods. Nord's method demonstrates considerably better reconstruction performance (median error of 0.012) in scene 231156. Note that all the median values of error are positive which indicates that there is a slight underestimation of $|S_{HV}|^2$ for all the reconstruction methods in the two SAR sea-ice scenes. Low standard deviation values for DoP- and Eig-based methods demonstrate the effectiveness of these methods that have closed form solution.

For Case 3, CP coherence matrix is used to reconstruct the pseudo-QP multilook covariance matrix. The reflection symmetry assumption has been shown to be valid for many natural targets [38, 39]. Here, as shown in Fig. 2.5, the plots of the two sides of the equations (2.15) and (2.18) are provided, which are respectively used as the second assumption in the Souyris's and Nord's reconstruction methods.

The values on each side of both equations (2.15) and (2.18) are calculated using all the

30
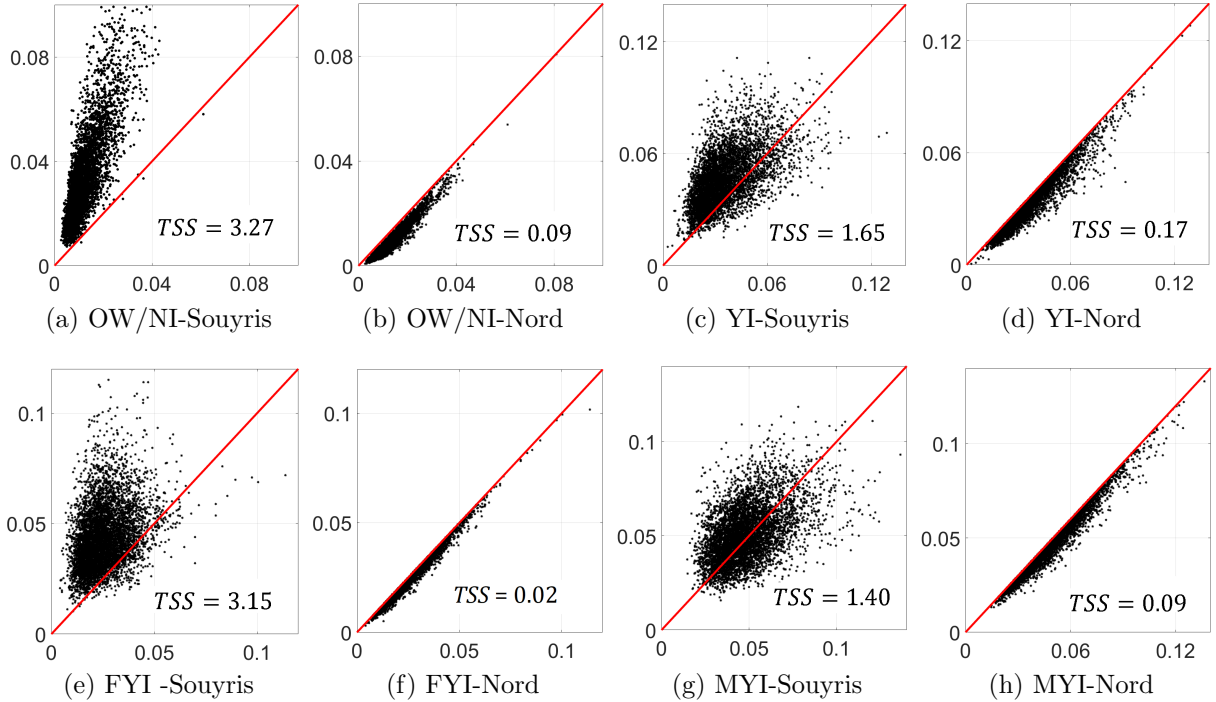
Figure 2.6: Scatter plots of the two sides of the equations considered as the second assumption in Souyris's and Nord's methods for (a)-(b) OW/NI (c)-(d) YI (e)-(f) FYI and (g)-(h) MYI sea-ice types, respectively.

pixels in the original QP data, and their scatter plots are respectively shown in Fig. 2.5. The pixels that fall along the diagonal support the validity of the assumption. The total sum of squares (TSS), which is the difference between the two sides of equations in each case, are also calculated and shown in Fig. 2.5. A lower TSS value for Nord's second assumption (2.18) in Fig. 2.5 (b) than than Souyris's method (2.15) in Fig. 2.5 (a) indicates that Nord's method is more accurate than Souyris's method for sea-ice application. According to Fig. 2.5 (a), the number 4 in the denominator of (2.15) should be larger as most of the pixels fall above the equality line. Fig. 2.5 (b) shows the Nord's method provides a good approximation where the pixels are tightened to the 45° line (These results confirm those by Nord *et al.* [39] where a data set from forestry and urban areas is used).

The median and standard deviation values of relative errors of reconstructing cross-pol intensities $|S_{HV}|^2$ for different sea-ice types are also calculated using the training and testing samples, and presented in Table 2.4. Since Nord's reconstruction method previously

Table 2.4: Median and standard deviation values of Nord's QP reconstruction errors for the reconstructed $|S_{HV}|^2$ values from CP relative to the original full QP $|S_{HV}|^2$ in different sea-ice types using training and testing samples.

Data source	Measure	OW/NI	YI	FYI	MYI
Training samples	Median	0.322	**−0.035**	0.101	-0.100
	Std. Dev.	**0.159**	0.241	0.201	0.227
Testing samples	Median	0.322	0.107	0.250	**0.071**
	Std. Dev.	**0.159**	0.180	0.187	0.219

provided the best results, the analysis of different ice types was only performed using Nord's method. Relatively higher median values for OW/NI class than those for other classes, especially, MYI class, indicate that Nord's reconstruction process is more accurate for the sea-ice types where random volume scattering is dominant. Nonetheless, for the case where the training samples were used, the median error is equal to -0.035 for YI class which is closer to zero than that of MYI class equaling -0.100, according to Table 2.4.

Moreover, to investigate the validity of the second symmetry assumption in Souyris's and Nord's methods for different sea-ice types, the values on each side of equations (2.15) and (2.18) are calculated for the pixels corresponding to the sample data in each sea-ice class, and plotted in Fig. 2.6. The TSS values are also calculated for each case shown in the corresponding plot. According to the scatter plots in Fig. 2.6, Nord's second assumption in (19) is an accurate equality and a good fit to the data. However, for Souyris's method, a majority of OW/NI pixels fall above the diagonal line indicating that the number 4 in the denominator in (2.15) should be higher. Relative to approximation in OW/NI class, the assumption in Souyris's method in (15) gives more accurate approximation for YI, FYI, and, especially, MYI sea-ice types indicating that this assumption does not hold particularly for the areas where single- and double-bounce scattering predominates such as OW/NI areas; however, the assumption is relatively more accurate for MYI pixels which mostly show random volume scattering.

2.7.2 Classification results

PolarIRGS segmentation described in Section 2.5.2 was then applied to the pseudo-QP matrix. The original QP data set is also used to extract the full covariance matrix data in Case 4. The segmentation results, which are respectively used in Cases 3 and 4, are shown in last column of Fig. 2.4. The next step is to create an SVM model to label the

Table 2.5: List of full QP features.

Name	Description	# of features
SPAN	span of the sample covariance matrix [30]	1
$H, A, \alpha,$ $\lambda, \delta, \gamma, \beta$	entropy-based decomposition features [67]	9
$T1, \ldots, T3$	coherency $T3$ matrix elements [30]	9
$\rho_{HHVV}, \rho_{HHVV},$ ρ_{HVVV}	correlation coefficients [30]	3
P_s, P_d, P_v	Yamaguchi decomposition [4]	3
$\tau, \psi, \Phi_s, \alpha_s$	Touzi decomposition [68]	4

segmented regions. For the first and second cases, only the DP and CP intensity images were used to train the SVM classifier. However, a list of Stokes vector derived features, shown in Table 2.1, are used in Case 3 as the feature vector in SVM. Also, for the full QP case (Case 4), the box-car filtered original QP data is used to extract 29 PolSAR features to leverage full polarimetric SAR capability in labeling. These features include the original SAR features (full QP coherency matrix elements), SAR discriminators (SPAN and correlation coefficients), and various decomposition parameters. The list of full QP features are presented in Table 2.5.

For SVM, the radial basis function (RBF) is used as the kernel function. The scale parameter γ in the RBF and the precision hyperparameter c in the SVM need to be tuned. Using training sample data and through a grid search in $c \in [2^{-1}, 2^9]$ and $\gamma \in [2^{-4}, 2^6]$ with an increment factor of one, the parameters were tuned. In particular, through a random selection, 4000 samples of training data are used for training the SVM model, and 1000 samples for testing. The values of c and γ associated with the highest classification overall accuracy were selected. Test Case 3 in the experiments, where all the CP-derived features are used in labeling, were used in parameter tuning. After this grid search, the values $c = 8$ and $\gamma = 64$ were obtained. As the purpose was to classify the scene into four classes, the one-against-all (OAA) strategy is used as the multi-class SVM method. This method tended to give better results in our application as compared to the one-against-one (OAO) method.

Using majority voting described in Section 2.5.4, the SVM labeling results, shown in Fig. 2.7(a)-(d), are combined with the unsupervised segmentation results, which provided
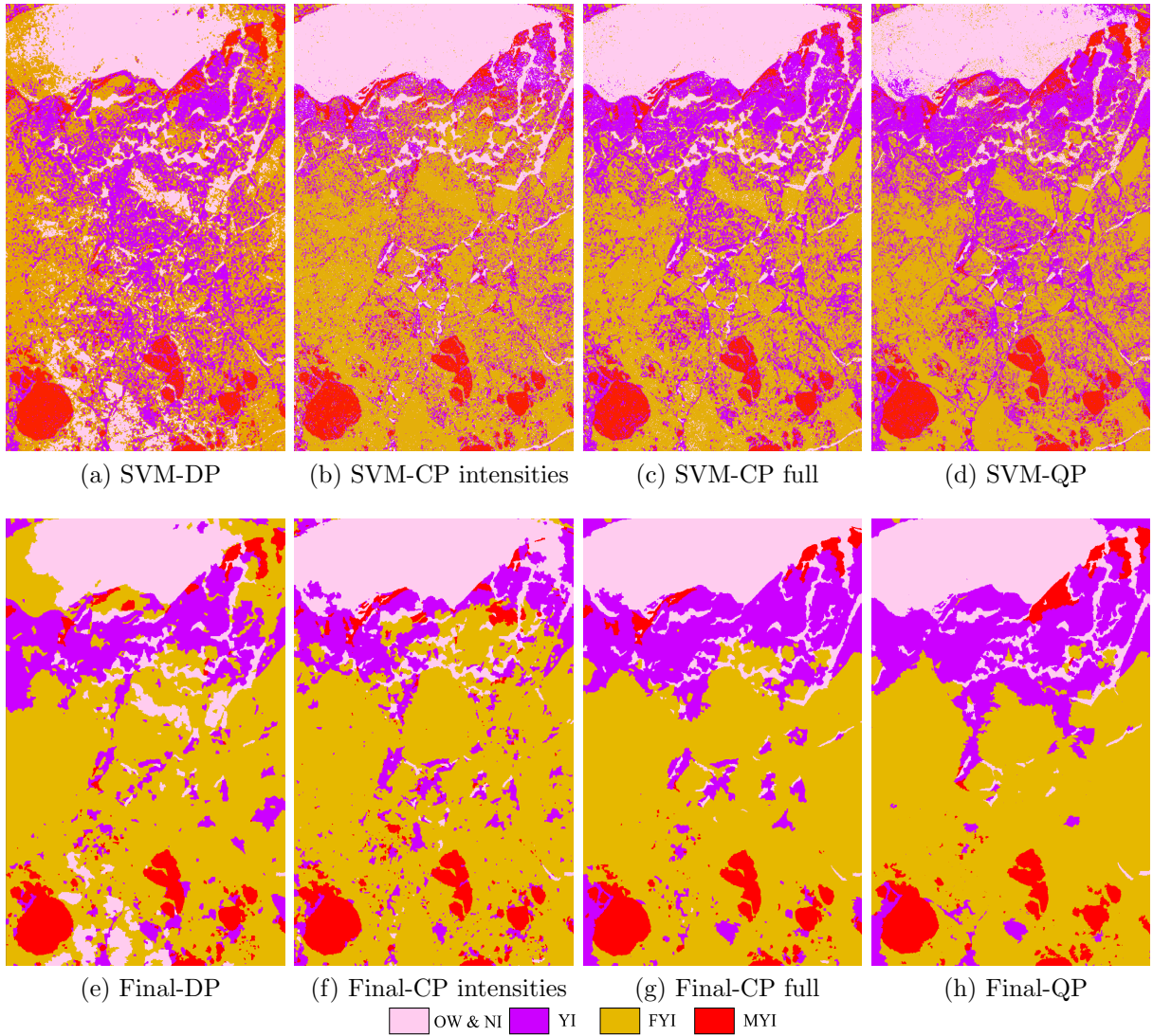
Figure 2.7: (a)-(d) Pixel-based SVM and (e)-(d) segmentation combined with SVM classification results using (a) and (e) HH and HV channel intensities only, (b) and (f) RH and RV channel intensities only, (c) and (g) all the CP features, (d) and (h) original QP data.

well-identified homogeneous regions. The final combined classification results are shown in Fig. 2.7(e)-(h), for the four cases. The noisy results of the SVM are improved by combining them with the unsupervised segmentation results.

Table 2.6: Segmentation method, features used for SVM, and error matrices on test samples for each case: DP, CP, all CP features, and full QP.

Case	Segmentation Method	Labeling Features		OW/NI	YI	FYI	MYI	User's Accuracy(%)
Linear DP (HH, HV)	IRGS using HH and HV intensities	HH and HV intensities	OW/NI	**3772**	4	1058	0	78.03
			YI	2	**4075**	239	2	94.37
			FYI	1452	828	**4762**	5	67.57
			MYI	1	668	8	**5630**	89.27
			Overall Accuracy (%)					**81.04**
			Kappa Coefficient					**0.7465**
CP (RH, RV)	IRGS using RH and RV intensities	RH and RV intensities	OW/NI	**5139**	174	4	0	96.65
			YI	74	**4120**	45	6	97.06
			FYI	13	748	**6013**	5	88.70
			MYI	1	533	5	**5626**	91.26
			Overall Accuracy (%)					**92.86**
			Kappa Coefficient					**0.9046**
All CP Features	PolarIRGS using reconstructed QP from CP	All CP-derived features	OW/NI	**5174**	8	5	0	99.75
			YI	48	**4922**	57	4	97.83
			FYI	4	26	**6002**	5	99.42
			MYI	1	619	3	**5628**	90.03
			Overall Accuracy (%)					**96.53**
			Kappa Coefficient					**0.9587**
Full QP	PolarIRGS using original full QP	Original full QP features (Table 2.5)	OW/NI	**5087**	8	4	0	99.76
			YI	7	**5197**	78	2	98.35
			FYI	133	25	**5979**	31	96.94
			MYI	0	345	6	**5604**	94.11
			Overall Accuracy (%)					**97.16**
			Kappa Coefficient					**0.9621**

The ice type classification performance on the test sampled data, as well as the segmentation method and the features used in the SVM classification for each case are presented in Table 2.6. The lowest overall accuracy was performed by the DP images (81.04%). In this case, the SVM classifier could not differentiate the ice types very well, where, as shown in Fig. 2.7(a), a high number of FYI pixels in the middle part of the scene are identified as

YI. Also, some of the FYI pixels in the lower-left part of the scene are erroneously classified in the OW/NI class. Some other cases of misclassification happened in the upper corners of the scene where some parts of OW/NI class are recognized as FYI. As a result, the final combined classification image in this case, Fig. 2.7(e), gives the lowest accuracy between the four cases.

Using only the RH and RV channel intensities, the classification results are presented in Fig. 2.7(b) and (f). Although there are some YI pixels in the upper-middle part of the scene classified as FYI, the classification results in this case are free from the misclassification cases in the DP case. This is evident when the overall accuracy and kappa coefficient (κ) values are compared for these two cases.

Combining the pseudo-QP-based segmentation and the SVM labeling using all of the CP features in Case 3, we could achieve more accurate classification result with an overall accuracy of 96.53%. The segmentation result using pseudo-QP data provides noticeably improved identified ice regions and leads (long narrow fractures) compared to using only RH and RV images (see Fig. 2.4 (g)-(h)). Note that the segmentation process takes about 3-5 minutes to execute in the case of using RH and RV images and about 15-20 minutes in the case of complex pseudo-QP data. Future work involves a more detailed and separate accuracy assessment of the segmentation step.

Finally, in Case 4, the classification overall accuracy achieved using the full QP data is equal to 97.16%, which is the highest accuracy among the four cases. Higher classification accuracy for the QP case than the CP case was expected because of the more polarimetric information that a fully polarimetric SAR provides. At the upper part of the scene, there are still some pixels in the boundary of OW/NI and YI classes incorrectly classified as MYI in both Case 3 and Case 4, which may be because of the similar backscatter information in these parts to those of the MYI-covered areas.

To assess the effect of number of training samples on the SVM and final classification results, different numbers of training samples were used from the set

$$n = \{5, 10, 25, 50, 100, 500, 1000, 2000, 3000, 4000, n_t\}$$

where n is the number of samples per class, and n_t is the total number of training samples (shown in Table II) for each ice type used to train the SVM classifier. Using all the CP-derived features for labeling and the reconstructed QP data for PolarIRGS segmentation (test Case 3), the SVM and final classifier with different number of samples were tested. Fig. 2.8 shows the plot of κ values of the SVM and final classification results using different number of samples for training the SVM classifier. According to Fig. 2.8, as the number of training samples increases, the κ values of classification using only SVM gradually increase.
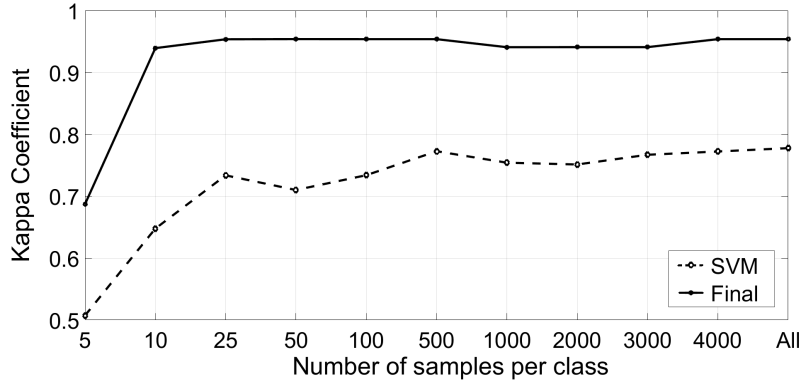
Figure 2.8: Plot of the κ coefficient values (ordinate) of SVM and final combined classification, using different number of training samples (abscissa) in test Case 3, where all the CP-derived features are used for labeling and the reconstructed QP data are used for PolarIRGS segmentation.

On the other hand, the final classification κ values, after a significant boost from 5 to 10 number of samples, remain steady without significant change. This indicates that using contextual information in the segmentation process and defining the segments in the image, one can achieve a very accurate classification result using only a few training samples for each class to train the classifier.

The classification using the aggregated feature sets for all the test cases described in the beginning of Section VII were also tested. Table 2.7 presents the classification overall accuracy and κ coefficients using two different methods for combining the labeling and segmentation results: majority voting and aggregated (median) feature sets. As shown in Table 2.7, the classification performance does not significantly vary if aggregated feature set is used instead of majority voting. Although the classification accuracy improves in Case 2 (linear DP) using aggregated feature set, in general, better classification can be obtained using majority voting as seen in other cases, CP, all CP features, and, especially, full QP.

To evaluate the effectiveness of reconstructed QP covariance data as compared to RH and RV intensities, and the reconstructed QP data against original QP data in the IRGS segmentation, two other test experiments were conducted in addition to the four test cases. First, only RH and RV intensity images were used in the segmentation step and all the CP-derived features (Table I) were used for labeling. The final classification overall accuracy and κ coefficient in this case were 94.45% and 0.9260, respectively. In the other case, the reconstructed QP data were used for segmentation, and the labeling were done

37

Table 2.7: Classification Overall accuracy (OA) and κ values of test samples using majority voting (MV) against aggregated features (AF) for each test case: DP, CP, all CP features, and full QP.

Case	Measure	MV	AF
Linear DP (HH, HV)	OA	**81.04**	80.94
	κ	**0.7465**	0.7452
CP (HH, HV)	OA	92.86	**95.04**
	κ	0.9046	**09337**
All CP Features	OA	96.53	**96.54**
	κ	**0.9587**	0.9539
Full QP	OA	**97.16**	93.15
	κ	**0.9621**	0.9085

using the original full QP features (Table 2.5). The overall accuracy and κ values were obtained as 96.61% and 0.9547, respectively. The results for these two cases indicate that using reconstructed QP data, the IRGS segmentation performs better than when only CP intensity images were used. Moreover, as expected, the performance of IRGS segmentation using the original full QP data is better than using reconstructed QP data from CP.

Using the reconstructed QP data, the QP features (Table 2.5) were extracted and used for labeling. Since the pseudo covariance matrix is not full and four elements are zero, not all of the original SAR features, SAR discriminators, and decomposition features can be extracted from pseudo QP data. Here, a total number of nine features (λ, H, α, P_v, T_{22}, $T_{13_{real}}$, $T_{13_{imag}}$, ρ_{HHVV}, τ) were found to be informative among 29 features listed in Table 2.5. Using these nine pseudo-QP derived features in labeling, and pseudo QP covariance data for segmentation, overall accuracy and κ coefficient were obtained as 96.32% and 0.9504, respectively. These values are close to those obtained in Case 3. This indicates that pseudo-QP derived features can also provide useful information in ice typing. Future work can lie on using CP- and pseudo-QP derived as well as texture features extracted from RH and RV intensities in ice typing. A feature selection process will likely be necessary to select the most informative features for training model.

2.8   Summary

With CP SAR data becoming accessible from the recent launch of the RCM satellites, automated CP SAR classification systems will be beneficial especially for CIS where the

CP sea-ice scenes will be used for ice map generation purpose. In this chapter, by combining the IRGS unsupervised segmentation results with supervised SVM labeling images, we performed full-scene classification with multiple ice types including OW/NI, YI, FYI, and MYI. The purpose was to compare the classification results using CP with those from linear DP data. It was demonstrated that using reconstructed QP data from CP as the input to PolarIRGS unsupervised segmentation algorithm and all CP-derived features for the SVM labeling method, an overall accuracy as high as that using full QP data is obtained. A comparison of the classification performance using only CP intensities against DP intensities showed the superiority of CP data with 11% higher overall accuracy than that of DP data.

Chapter 3

Unsupervised Segmentation Methodology

CP captures single-look complex (SLC) data which can be used to derive the multilook complex (MLC) coherence matrix, or, equivalently, the Stokes vector data of the backscattered field. The purpose of this chapter is to develop computer vision algorithms that can be used to effectively segment the scene using this new data source. An unsupervised region-based segmentation approach is designed and implemented that utilizes the complex Wishart distribution characteristic of the MLC CP data. The algorithm is tested using both simulated CP SAR images based on complex Wishart distribution and a pair of available quad polarization SAR images. This chapter is based on a published article [24].

3.1 Introduction

A CP SAR maximizes the measurement potential of a radar illumination by providing the four elements of Stokes vector, or equivalently, the 2×2 coherence matrix of the backscattered field [69]. This is the main advantage of a CP SAR over the traditional dual-polarized SARs. Self-calibration capability, less error sensitivity (to relative errors and cross-talk), and comparable signal levels in the two received polarization channels are other advantages of CP SARs [3]. The RADARSAT Constellation Mission (RCM), which is the successor of the RADARSAT-1 and -2 satellites, includes three satellites that were all launched June 2019. Each satellite, in addition to the QP and DP modes, also has a CP mode that is implemented in wide swaths. This will be utilized extensively by a primary

user of this data, the Canadian Ice Service (CIS). CIS experts process 1000s of SAR scenes annually and manually generate maps of ice regimes on a daily basis. As such, automated methods based on computer vision algorithms for mapping ice regimes using CP SAR data are advocated.

CP data to support classification and segmentation methodologies can be categorized into two main approaches. In the first approach, the four elements of the Stokes vector and all the derived "child parameters" are used as features [38, 42]. In the second approach, based on two target symmetry assumptions, the QP 3×3 covariance matrix is reconstructed using the CP 2×2 coherence matrix. The reconstructed "pseudocovariance" matrix (pseudo-QP data) is then used to support the classification algorithm [33].

In this chapter, a different approach is proposed. Directly using the 2×2 coherence matrix, which is more favorable than using pseudocovariance matrix [70], an unsupervised region-based segmentation method on the basis of the statistical properties of the CP coherence matrix is developed. The region-based segmentation is formulated using Markov random fields (MRFs). A region-based segmentation algorithm uses the statistical properties of regions, and, as a result, is less sensitive to the multiplicative speckle noise and intra-class nonstationarities that are prevalent in wide-swath SAR images. Also, a region-based segmentation method is favorable in computation speed as the number of regions is significantly smaller than the number of pixels. We know of no other published paper that performs unsupervised region-based segmentation of complex CP SAR images.

The region-based segmentation approach proposed in this thesis is based on a published unsupervised segmentation method called IRGS [20] which has been shown to be successful when applied to generic imagery, hyperspectral imagery, amplitude SAR imagery, as well as complex QP SAR data (PolarIRGS) [21, 22, 26, 58]. IRGS is based on MRFs and incorporates an edge strength measure in the MRF's spatial context model as well as a novel iterative region-merging process [26]. In an MRF-based segmentation model, using Bayesian inference, the optimal label field is obtained through maximizing the multiplication of conditional probability density function ("feature model" or "likelihood") and the probability of a random field ("spatial context model" or "prior") [21].

In this thesis, an extension to the IRGS algorithm for CP SAR data is formulated and implemented. The backscattered field in a CP SAR is known to follow a complex Gaussian distribution and, as such, this leads to the multilook CP coherence matrix to be Wishart distributed and this acts as the unary and pairwise potentials of the MRF in the region-based CP-IRGS segmentation method. The statistical significance of differences [71] in CP coherence matrices is used in a novel definition of edge strength and the weight parameter in the pairwise potential of the MRF model. Moreover, based on the assumption that the

"product model" [72] is held for the CP backscatter field, a CP coherence matrix data set is simulated and used in the performance evaluation of the proposed segmentation method.

In summary, in this chapter, we provide a detailed description of the statistical characteristics of the CP data and develop a region-based unsupervised segmentation method for CP data. Our main contributions are as follows:

- Despite the great amount of work in the literature on segmentation/classification using DP and QP SAR data, the studies on segmentation/classification using CP data are limited. Here, for what we expect is the first time in the literature, we propose a region-based approach to unsupervised segmentation of CP data by developing a CP extension of IRGS segmentation methodology.

- In the pairwise potential of IRGS, a new edge strength calculation and weight parameter estimation methods are developed particularly based on the complex CP data type.

- Based on the statistical properties of the complex CP backscatter field data and the product model, a method is proposed to simulate complex CP scenes. The simulated scenes allow for accurately evaluating the proposed unsupervised segmentation method since the boundaries are known.

Section 3.2 provides the statistical formulation of the complex CP data. Section 3.3 provides a method to simulate complex CP data. Section 3.4 outlines the IRGS algorithm structure. Section 3.5 details the proposed CP-IRGS including the formulation of the MRF data likelihood and the prior term. Section 3.7 describes the simulated and real complex SAR images which are used to evaluate the performance of the CP-IRGS segmentation in Section 3.8. Conclusions and future work are provided in Section 3.9.

3.2   Statistical Modeling of Complex CP SAR Data

The purpose of this section is to provide the statistical formulation of the MLC CP coherence matrix data. In a CP SAR, a complex measurement vector $\mathbf{E}$ of the backscattered field is measured. The radar scattering matrix $\mathbf{S}$ relates the incident field to the backscatter one [30]

$$\mathbf{E}_{CP} = \begin{bmatrix} E_H \\ E_V \end{bmatrix} = \mathbf{S}\hat{\mathbf{u}}_t \tag{3.1}$$

where $\hat{\mathbf{u}}_t$ is the unit Jones vector related to the incident field. The 2×2 Hermitian positive semidefinite MLC coherence matrix ($\mathbf{J}$) is derived via multiplying $\mathbf{E}_{CP}$ by its complex conjugate transpose [32]

$$\mathbf{J} = \frac{1}{L} \sum_{i=1}^{L} \mathbf{E}_{CP} \mathbf{E}_{CP}^{\dagger} = \begin{bmatrix} \langle |E_H|^2 \rangle & \langle E_H E_V^* \rangle \\ \langle E_V E_H^* \rangle & \langle |E_V|^2 \rangle \end{bmatrix} \tag{3.2}$$

where $< \cdots >$ shows temporal or spatial averaging, $\dagger$ indicates Hermitian conjugate, and L is the number of looks used for averaging.

Since a radar illuminates an area of many random scatterers, the 2D measurement vector $\mathbf{E}_{CP}$ in (3.1) provided by a CP SAR can be assumed to have a bivariate complex Gaussian distribution

$$p(\mathbf{E}_{CP}) = \frac{1}{\pi^2 |\mathbf{B}|} \exp\left(-\mathbf{E}_{CP}^{*T} \mathbf{B} \mathbf{E}_{CP}\right), \tag{3.3}$$

where $\mathbf{B} = \mathscr{E}\{\mathbf{E}_{CP} \mathbf{E}_{CP}^{*T}\}$, in which $\mathscr{E}$ represents the mathematical expectation, is the Hermitian complex coherence matrix. The value $\mathbf{J}$ (3.2) is the maximum likelihood estimator and a sufficient estimator for $\mathbf{B}$ [73]. Then, Goodman *et al.* [73] showed the matrix $\mathbf{G} = L\mathbf{J} = \sum_{i=1}^{L} \mathbf{E}_{CP_i} \mathbf{E}_{CP_i}^{*T}$ has a complex Wishart distribution. Given that the size of the tuple of complex Gaussian variables in Eq. (1.6) is equal to 2 (the dimension of vector $\mathbf{E}_{CP}$) here, the probability density function of $\mathbf{G}$ is given by

$$p(\mathbf{G}) = \frac{|\mathbf{G}|^{L-2}}{\pi \Gamma(L) \Gamma(L-1) |\mathbf{J}|^L} \exp\left[-\text{tr}\left(\mathbf{J}^{-1} \mathbf{G}\right)\right] \tag{3.4}$$

where $|\cdot|$ is the determinant operator, $\text{tr}(\cdot)$ represents the trace of a matrix, and Γ is Gamma function. $p(\mathbf{G})$ is defined over the domain $D_{\mathbf{G}}$ where $\mathbf{G}$ is Hermitian semi-definite [73].

3.3 Simulation method of MLC CP

Simulating MLC CP scenes allows for accurately evaluating the proposed unsupervised segmentation method since the boundaries are known. A multilook CP coherence matrix data set can be simulated based on the assumption that the "product model" is held for

the complex vector of the backscattered field (2.3) [1]

$$\mathbf{E}_{CP} = \sqrt{T}\mathbf{Q} \tag{3.5}$$

where $\mathbf{E}_{CP}$ consists of the CP complex measurements E_H and E_V. In Eq. (3.5), it is indicated that the CP measurements are statistically modeled by the product of two terms: T which is a positive scalar that models the texture (spatial variation in the mean backscatter) and a random variable $\mathbf{Q}$ known as speckle parameter that is assumed to be complex Gaussian distributed [2]. Then, according to Eqs. (3.2) and (3.5), the multilook complex coherence matrix is given by [74]

$$\mathbf{J} = \frac{1}{L}\sum_{i=1}^{L}\mathbf{E}_{CP}(l)\mathbf{E}_{CP}^{\dagger}(l) = \frac{1}{L}\sum_{l=1}^{L}T(l)\mathbf{Q}(l)\mathbf{Q}^{\dagger}(l). \tag{3.6}$$

For a SAR scene with homogeneous areas, it can be assumed that $T(l) = T$. Based on the assumption that $\mathbf{Q}$ has a complex Gaussian distribution, as discussed earlier, the matrix $\sum_{l=1}^{L}\mathbf{Q}(l)\mathbf{Q}^{\dagger}(l)$ becomes complex Wishart distributed. Therefore, depending on the probability distribution of T (3.5) that is chosen based on the homogeneity of the scene, the MLC CP coherence matrix $\mathbf{J}$ obeys different parametric distributions [75]. The simplest case is for homogeneous areas where texture is assumed to be constant. Other probability distributions such as Gamma and generalized inverse Gaussian were also considered in the literature to model the texture parameter in the heterogeneous and extremely heterogeneous areas, respectively [76].

3.4   Background

This section summarizes the fundamental steps of the IRGS segmentation algorithm [20]. Let $\mathcal{S}$ be the image and $s \in \mathcal{S}$ be a site on the image (an image pixel). Also, assume that $\mathbf{x} = \{x_s | s \in \mathcal{S}\}$ represents the image data and $\mathbf{y} = \{y_s | y_s \in \mathcal{M}, s \in \mathcal{S}\}$ is a label configuration on the image with discrete-valued random variables y_s having a value from the label set $\mathcal{M} = \{1, ..., m\}$. The purpose of an image segmentation is essentially to find the optimum label configuration. IRGS is formulated based on the Bayesian theory where

---

[1]This assumption is valid when the mean number of scatterers that contribute to a pixel measurement in a CP image is large. For more description, please refer to the work by Olivier *et al.* [72].

[2]This is the more general case of what discussed earlier where we mentioned the CP complex measurements $\mathbf{E}_{CP}$ has a complex Gaussian distribution.

the objective is to find a label configuration $\mathbf{y}^*$ that satisfies

$$\mathbf{y}^* = \arg\max_{\mathbf{y} \in \mathbf{Y}} p(\mathbf{x}|\mathbf{y})P(\mathbf{y}) \tag{3.7}$$

where $\mathbf{Y}$ is the set of possible label configurations. The term $p(\mathbf{x}|\mathbf{y})$ is called the feature model or data likelihood and is the conditional probability density function of the image data $\mathbf{x}$ given the label configuration $\mathbf{y}$. $P(\mathbf{y})$ indicates the prior also called the spatial context model. IRGS is a region-based method which uses a region adjacency graph (RAG) [19] and aims to find the optimum label field over a RAG instead of all the image sites separately. A RAG is defined as $\mathcal{G} = (\mathcal{V}, \mathcal{E})$ where $\mathcal{V}$ and $\mathcal{E}$ denote the image regions as vertices and arcs that are the boundaries of adjacent regions. Thus, a region $v \in \mathcal{V}$ in the image consists of a set of image sites $\mathcal{S}_v$.

In IRGS, a Gaussian mixture model [21] is used to model $p(\mathbf{x}|\mathbf{y})$ with an expectation-maximization (EM) algorithm to estimate the parameters of the Gaussian mixture. Also, the spatial context model $P(\mathbf{y})$ is defined using an edge strength measure [20]. By taking a logarithm and multiplying the terms (3.7) by -1 [3], the problem is converted to the minimization of two energy terms

$$\mathbf{y}^* = \arg\min_{\mathbf{y} \in \mathbf{Y}} \{ -\sum_{\mathcal{S}_v \in \mathcal{V}} \sum_{s \in \mathcal{S}_v} \psi_u(x_s, y_s)$$
$$-\sum_{\mathcal{S}_v \in \mathcal{V}} \sum_{s \in \mathcal{S}_v} \sum_{n \in \mathcal{N}_s} \psi_p(y_s, y_n) \} \tag{3.8}$$

where ψ_u and ψ_p are called the unary and pairwise clique potentials. The unary potential is summed up over all sites in the vertex $\mathcal{S}_v$, which is the region that includes the site s, from the set $\mathcal{V}$, and the pairwise potential is summed up over all the pair sites s and n, where $\mathcal{N}_s$ is the set of neighbors of the site s. By substituting the corresponding spatial context model in IRGS [20]

$$\mathbf{y}^* = \arg\min_{\mathbf{y} \in \mathbf{Y}} \{ -\sum_{i=1}^{m} \sum_{\mathcal{S}_v \in v_i} \sum_{s \in \mathcal{S}_v} \ln\{p(\mathbf{x}_s|y_s = i)\}$$
$$+ \beta \sum_{i=1}^{m-1} \sum_{j=i+1}^{m} \sum_{s \in \partial v_i \cap \partial v_j} g(\nabla_s) \} \tag{3.9}$$

---

[3]The terms are multiplied by -1 to convert the probability maximization problem to an energy minimization problem.

where $g(\nabla_s)$ is called the edge penalty term [21], v_i is a subset of $\mathcal{V}$ with label i, and ∂v_i indicates all the boundary sites between regions labeled i with other regions. Thus, $\partial v_i \cap \partial v_j$ denotes all the boundary sites between classes i and j. In the first term on the right side of (3.9), $p(\mathbf{x}_s|y_s = i)$ is the probability value of obtaining $\mathbf{x}_s$ given the label of the site s is i. This term is modeled by a Gaussian mixture model in IRGS [20]. In the second term, the edge penalty function $g(\nabla_s)$ is a monotonically decreasing function (when the edge strength for a specific boundary site is high, the penalty is low) that generates a sequence of edge penalties for each iteration of the algorithm [20]. The parameter β controls the smoothness of the segmentation with the greater values of β leading to smoother segmentation results.

IRGS uses a simulated annealing (SA) algorithm to solve the combinatorial optimization problem (3.9). Also, in each iteration before the optimization by SA, IRGS performs a region merging process to reduce the number of regions and to avoid being trapped in a local minima [20, 26]. In summary, after constructing RAG on the "deliberate" oversegmentation image obtained by the watershed algorithm [28], IRGS starts its iterations. In each iteration, SA assigns a label to each region to move the label configuration toward the optimal solution. Adjacent regions that have the same class labels, are then merged in a greedy fashion using a merging criterion ∂E [20], and, afterwards, the next iteration is executed.

PolarIRGS, the extension to IRGS for QP SAR data, was developed by Yu *et al.* [21]. Based on Wishart distribution, the unary potential was derived in PolarIRGS. The data input in PolarIRGS is the complex QP data which is different than the complex CP data in terms of physical interpretation. The complex QP data is derived from the elements of scattering matrix ($\mathbf{S}$ in Eq. (2.3)), however, the complex CP data is extracted from the complex backscattered field ($\mathbf{E}_{CP}$ in Eq. (2.3)). These two data types are related by Eq. (2.3) as discussed in Section 3.2. The unary based on complex Wishart distribution and the region merging criterion in PolarIRGS [21] are used here by modifying the data type to complex CP data and new methods are proposed for the calculation of edge penalty and the weight parameters in the pairwise potential.

3.5 Proposed Unsupervised Segmentation: CP-IRGS

In this section, we describe the formulation of the proposed algorithm based on the complex Wishart distribution. In Section 3.5.1 and 3.5.2, we will define the unary and pairwise clique potentials in the formulation (3.8) of CP-IRGS.

3.5.1 Complex CP-based unary potential

The data likelihood term $p(\mathbf{x}_s|y_s = i)$ (3.9) is defined here for MLC coherence matrix data. For each site s in an MLC CP image, the observation data x_s is the MLC coherence matrix, i.e., $x_s = \mathbf{G}_s$, where $L\mathbf{J}_s = \mathbf{G}_s$ was shown in Section 3.2 to have a complex Wishart distribution. Therefore, the conditional probability of obtaining $\mathbf{x}_s$ given the site s is labeled y_s, $p(\mathbf{x}_s|y_s)$, is given by [4]

$$p(\mathbf{J}_s|y_s) = \frac{L^{2L}|\mathbf{G}_s|^{L-2}}{\pi\Gamma(L)\Gamma(L-1)|\mathbf{J}_{y_s}|^L} \exp\left[-L\mathrm{tr}\left(\mathbf{J}_{y_s}^{-1}\mathbf{G}_s\right)\right] \tag{3.10}$$

where $\mathbf{J}_{y_s}$ is the average MLC coherence matrix for all the sites labeled y_s. According to equations (3.8) and (3.9), the unary potential term in CP-IRGS is given by

$$\psi_u(x_s, y_s) = \ln\{p(\mathbf{J}_s|y_s)\} \tag{3.11}$$

By taking the natural logarithm of $p(\mathbf{J}_s|y_s)$, and eliminating all the elements that are not a function of y_s the unary term is given by

$$\psi_u(x_s, y_s) = \sum_{\mathcal{S}_v \in \mathcal{V}} \sum_{s \in \mathcal{S}_v} \{\ln|\mathbf{J}_{y_s}| + \mathrm{tr}\left(\mathbf{J}_{y_s}^{-1}\mathbf{G}_s\right)\} \tag{3.12}$$

3.5.2 Complex CP-based pairwise potential

We define the pairwise potential in CP-IRGS as

$$\psi_p(y_s, y_n) = \begin{cases} \beta g(\nabla_s) & \text{different labels} \\ 0 & \text{otherwise} \end{cases} \tag{3.13}$$

where "different labels" means that the sites s and n are labeled differently. ∇_s is the edge strength measure at the site s, and the edge penalty function $g(\nabla_s)$ is defined as in the original IRGS algorithm [20, Eq. 18]

$$g(\nabla_s) = \exp\left[-\left(\frac{\nabla_s}{K(i)}\right)^2\right] \tag{3.14}$$

---

[4]Note that the probability function in Eq. (3.10) directly models the MLC CP coherence matrix $\mathbf{J}$, and it is slightly different than Eq. (3.4). The probability function in Eq. (3.10) is often called the *scaled complex Wishart distribution* [76].
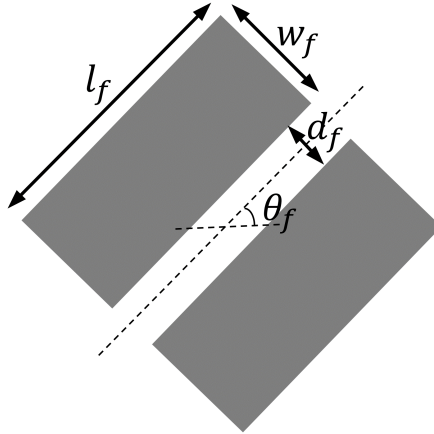
Figure 3.1: Bi-window configuration used in the edge strength map calculation.

where $K(i)$ is a positive coefficient that monotonically increases with the iteration number i to control the effect of the edge penalty term ([20, Section 3.1]). At a conceptual level, Eq. (3.13) increases the pairwise potential by $\beta g(\bigtriangledown_s)$ if adjacent regions are of different labels, and in this manner, penalizes segmentations where neighboring regions have weak edges and different labels.

Calculating edge strength

Measuring the edge strength $\bigtriangledown_s$ in each site s can essentially be considered as an edge detection problem. Two edge strength calculation methods are developed. In the first method, following the previous IRGS papers [20,21], the intensity values in the RH and RV CP channels are used in the vector field gradient (VFG) method [77]. The second method is to develop an edge strength measure that uses the MLC CP coherence matrix data as its input. We propose to use the ratio-based edge detectors [78–80] with a complex-CP based *similarity* measure. As shown in Section 3.2, since the MLC CP coherence matrix shares statistical properties with the QP MLC covariance matrix, all the similarity measures for the QP covariance matrices are immediately applicable to the CP coherence matrices.

The ratio-based detectors [78, 80] use a rectangle bi-window configuration shown in Fig. 3.1. In particular, as shown in Fig. 3.1, the bi-window configuration consists of two parallel rectangles which are specified by two parameters: length l_f and width w_f, a spacing parameter d_f, and an orientation angle θ_f. Touzi *et al.* [78] proposed using the ratio of mean intensity values in SAR images and operating a constant false alarm rate

48

(CFAR)-based thresholding afterwards. This algorithm is called likelihood test ratio, and has also been expanded for the QP SAR images [80]. Here, we use the Hotelling-Lawley trace (HLT) [81] as the similarity measure. The HLT statistic is considered as the matrix-variate version of the intensity ratio test [81]. The HLT measure has shown to be an effective test statistic compared to the measures such as Kullback-Leibler divergence in the problem of change detection using the MLC QP covariance matrix data [82]. Since the change detection methods based on test statistics such as the HLT statistic are based on the difference between two MLC QP covariance matrix in the time series, the problem of change detection is similar to the edge strength calculation problem using a ratio-based edge detector, where the difference between the two mean MLC matrices from the two windows in Fig. 3.1 are measured. The HLT statistic measures the similarity between two complex matrix-variates $\mathbf{J}_1$ and $\mathbf{J}_2$

$$\tau_{\text{HLT}} = \text{tr}(\mathbf{J}_1^{-1}\mathbf{J}_2) \tag{3.15}$$

where $\mathbf{J}_1$ and $\mathbf{J}_2$ are two mean MLC CP coherence matrices in the two rectangles in Fig. 3.1. Note that τ_{HLT} becomes the intensity ratio when $\mathbf{J}_1$ and $\mathbf{J}_2$ are two scalars indicating intensity values. In the case $\mathbf{J}_1 = \mathbf{J}_2$, the HLT statistic equals the dimension of a complex CP coherence matrix, i.e., $\tau_{\text{HLT}} = 2$. In the case of "dissimilar" $\mathbf{J}_1$ and $\mathbf{J}_2$, τ_{HLT} obtains values distant from d. Based on the type of difference in the two mean coherence matrices, τ_{HLT} can obtain positive values either "smaller" or "much larger" than the dimension of a complex CP coherence matrix [82]. Therefore, the maximum value of $\text{tr}(\mathbf{J}_1^{-1}\mathbf{J}_2)$ and $\text{tr}(\mathbf{J}_2^{-1}\mathbf{J}_1)$ is used here as the test statistic

$$\tau_{\text{maxHLT}} = \max\{\text{tr}(\mathbf{J}_1^{-1}\mathbf{J}_2), \text{tr}(\mathbf{J}_2^{-1}\mathbf{J}_1)\}. \tag{3.16}$$

Finally, considering there are n_θ different orientation angles, we take the minimum value of τ_{maxHLT} from all the orientations

$$\tau_{\text{total}} = \min_{i=1,\ldots,n_\theta} \{\tau_{\text{maxHLT}}^{\text{i}}(\mathbf{J}_1, \mathbf{J}_2)\}. \tag{3.17}$$

where $\tau_{\text{maxHLT}}^{\text{i}}$ is the τ_{maxHLT} value for the ith orientation. Each orientation angle i corresponds to a pair of mean MLC coherence matrices $\mathbf{J}_1$ and $\mathbf{J}_2$ (from the two rectangles in the bi-window configuration). For each i, the "dissimilarity" between the two mean MLC coherence indicates that there is a change in radar backscatter in that orientation. Taking the minimum value of all the dissimilarity values from different orientations captures the smallest changes in backscatter values in all orientations. In this thesis, $n_\theta = 2$, i.e., two orientation angles are considered: $\theta_f = 0$ and $\theta_f = 90$, where the windows are in horizontal

and vertical directions, respectively. Also, the dimension parameters, $l_f = 5$ and $w_f = 3$ produced the best results in this thesis.

Estimating the weight parameter β

The weight parameter β in the pairwise potential (3.13) and in the equation related to the region growing (3.20) should be estimated in each iteration of the algorithm. In the standard IRGS [20], the parameter β is determined by the boundary length expected over the whole image, and, then, it is adjusted to be adaptive to the noise strength of the image. In particular, in each iteration i, a value $\beta_0(i)$ is estimated as a prior via maintaining the expectation of the boundary length the same as the current [20, 83]. To incorporate the noise strength in each iteration of the segmentation into the parameter β, Yu *et al.* [20, (23), (24)] used the Fisher criterion as a separability measure between any pair of classes in the image for adjusting the prior $\beta_0(i)$. Here, we use τ_{maxHLT} statistic [5]

$$\hat{\beta}(i) = C_1 \frac{h}{C_2 + h} \beta_0(i), \tag{3.18}$$

where $\hat{\beta}(t)$ represents the adjusted weight parameter. C_1 and C_2 are two constants which are set based on the the homogeneity of the scene. For the SAR scenes with homogeneous classes (less noise), C_1 and C_2 are set to 1.5 and 0.4, and if the classes in the scene are noisy, a smaller number is set to C1: $C_1 = 1$ and $C_2 = 0.4$. The parameter h (3.18) is also given by

$$h = \min_{i,j}\{\tau_{\mathrm{maxHLT}}(\mathbf{M}_i, \mathbf{M}_j)\} \tag{3.19}$$

where h is a measure of separability between all pairs of classes i and j with respect to the mean value of the MLC CP coherence matrices of the two classes $\mathbf{M}_i$ and $\mathbf{M}_j$.

3.5.3 Region merging criterion

One of the main features of the IRGS algorithm is incorporating a region merging technique in each iteration of the optimization. Starting from an oversegmentation, a region merging process is executed in each iteration. Only for all pairs of the neighboring regions with the same labels, the energy terms (3.9) for two cases are calculated: (1) merging the two

---

[5]See Section 4.3 in the work by Yu *et al.* [20] for more description.

Algorithm 1 CP-IRGS Algorithm

Input: Set C_1 and C_2 (3.18), number of classes m, and maximum number of iterations t_{max}.

Output: Segmentation image with m classes.

   Initialization:
 1: Compute the edge strength τ_{total} (3.17) for each site in the image.
 2: Apply watershed to obtain an oversegmentation and construct a RAG with each watershed region as a vertex.
 3: Assign a random label to each watershed region
 4: Apply a region-based K-means algorithm [58] to obtain an initial segmentation from which the average MLC coherence matrix for each class is calculated.
   LOOP Process
 5: **for** $t = 1$ to t_{max} **do**
 6:    Update β and K.
 7:    Scan all the vertices in a random manner and assign a label to each vertex that minimizes energy terms in $\mathbf{y}^*$ (3.9).
 8:    **Repeat:** While all $\partial E \geq 0$
 9:       Compute ∂E (3.20) for all adjacent regions that have the same label.
10:       Merge the region pair with the most negative ∂E.
11: **end for**
---

regions and (2) keeping the regions separate. If the merged case reduces the energy, the regions are merged. The region merging criterion is given by [20, 21]

$$\partial E(i,j) = n_{ij} \ln |\mathbf{M}|_{ij} - n_i \ln |\mathbf{M}_i| - n_j \ln |\mathbf{M}_j| \\ - \beta \sum_{s \in \partial v_i \cap \partial v_j} g(\nabla_s) \qquad (3.20)$$

where $\partial E(i,j)$ is the energy difference between before and after merging, n_i is the number of pixel sites in region i, and ij denotes the region obtained from merging regions i and j. $\mathbf{M}_j$ is the average MLC CP coherence matrix of region i.

3.5.4 CP-IRGS algorithm overview

An overview of the CP-IRGS algorithm is shown in Algorithm 1. After an oversegmentation using the watershed algorithm [28], a RAG is constructed. To start the algorithm, an initialization is required to input into the algorithm. Through this initialization, each region is assigned a label and, then, the mean MLC CP coherence matrix for each class is computed. The initialization image is obtained via applying a region-based K-means algorithm [58] on the RH and RV channel intensity images.

CP-IRGS is executed in two main nested loops. The outer loop guides the segmentation to the optimal configuration. In each iteration of this loop, the parameter β (3.18) and K (3.14) are updated. Then, all the vertices in the RAG are assigned a label (3.9). In particular, via a simulated annealing algorithm, all the vertices in the RAG are scanned in a random manner, and each vertex is assigned a label that minimizes the energy terms (3.9). The inner loop executes the region growing process. In each iteration of the inner loop, for all the neighboring pairs of regions that have the same class label, the criterion ∂E (3.20) is computed. The region pair with the most negative ∂E are merged. The inner loop ends when there is no adjacent pair with the same label that has $\partial E < 0$.

3.6 Experimental Setup

An unsupervised segmentation algorithm is expected to produce an image where each pixel is assigned to a particular class with an unknown label. A labeling step is usually followed to assign ground truth labels (the actual class labels of the scene) to the regions in the image [11, 23]. Since the objective of this chapter is unsupervised segmentation, to evaluate the algorithm without any uncertainties due to an imperfect labeling process, the segmentation regions are assigned labels based on the fully labeled ground truth image of the scenes. The fully labeled ground truth images were produced using the labeled samples from on a grid over the scene from the CIS ice experts and oversegmentation images from the scene.

Each class in the unsupervised segmentation image is assigned a label via a majority voting process on the ground truth labels of the pixels inside the class. In other words, in each segmentation class, the number of pixels with each label in the ground truth image is counted and all the regions of the segmentation class is assigned the label associated with the maximum number of pixels. An accurate segmentation provides segmentation classes that are homogeneous, i.e., each class in the segmentation image contains areas only from one ground truth class.
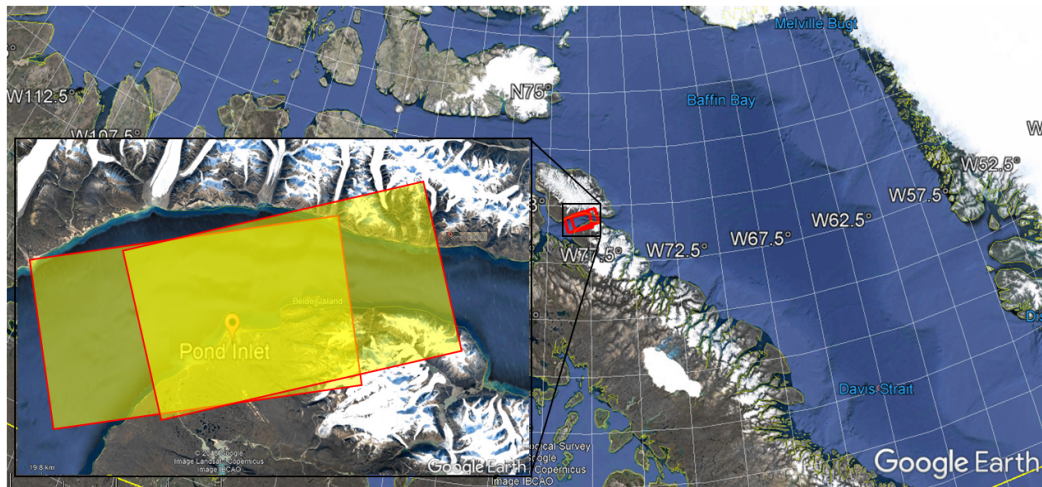
Figure 3.2: (a) The locations of the two RADARSAT-2 fine QP scenes in the Pond Inlet. The Pauli RGB composites (Red: $|HH - VV|$; Green: $2|HV|$; Blue $|HH + VV|$) of the scenes (b) Dec16 and (c) Jan17. Example ice types in the scenes are labeled.

After labeling, the overall accuracy (OA), the accuracy of each class, and the Kappa coefficient (κ) are computed as accuracy measures of the algorithm. Moreover, to measure the effectiveness of the region merging in the unsupervised segmentation algorithm, the total number of regions in the segmentation image is counted. Favorably, the segmentation algorithm should produce images where the regions are as homogeneous as possible (i.e., high accuracy values) and the number of regions is as low as possible.

Three cases are tested and compared:

Table 3.1: The elements of the mean MLC CP coherence matrices for each class in the simulated data

Class	$\mathbf{J}_{11}$	$\mathbf{J}_{12}$	$\mathbf{J}_{22}$
OW/NI	0.0069	0.0008-0.0056j	0.0118
YI	0.0400	0.0032-0.0272j	0.0407
FYI	0.0167	0.0006-0.0106j	0.0163
MYI	0.0549	0.0040-0.0338j	0.0556

Case 1: The standard IRGS method [20] using the RH and RV intensities.

Case 2: The CP-IRGS method described in Algorithm 1 using vector field gradients (VFG) [77] method on the RH and RV intensities for edge strength map calculation.

Case 3: The CP-IRGS method using edge strength map method described in Section 3.5.2, which will be referred to as the CP-IRGS using complex ratio (CR)-based method.

The IRGS method in Case 1 uses only the CP channel intensities. In Case 2, the CP-IRGS method uses the MLC CP coherence matrix data in the unary potential, however, in the pairwise potential, the CP channel intensities are used in the VFG. In Case 3, both the unary and pairwise potentials are calculated based on the MLC CP coherence matrix data. The data sets will be described in the next section, and the experiments and analyses are provided afterwards.

3.7 Data Sets

A multilook CP coherence matrix data set of sea-ice with 1500×1500 pixels were simulated using the simulation method described in Section 3.3 based on the assumption that the texture is constant. The mean coherence matrix for each class was derived from a real CP SAR scene. Elements of the mean coherence matrices for sea-ice classes are presented in Table 3.1. The class boundaries of a real SAR sea-ice scene were used for the simulated MLC CP image, and, then, the regions of each class were populated by the corresponding simulated pixel values of the MLC coherence matrix.

(a) $M - \chi$

(b) Ground truth

(c) IRGS using RH and RV

(d) Labeled IRGS using RH and RV
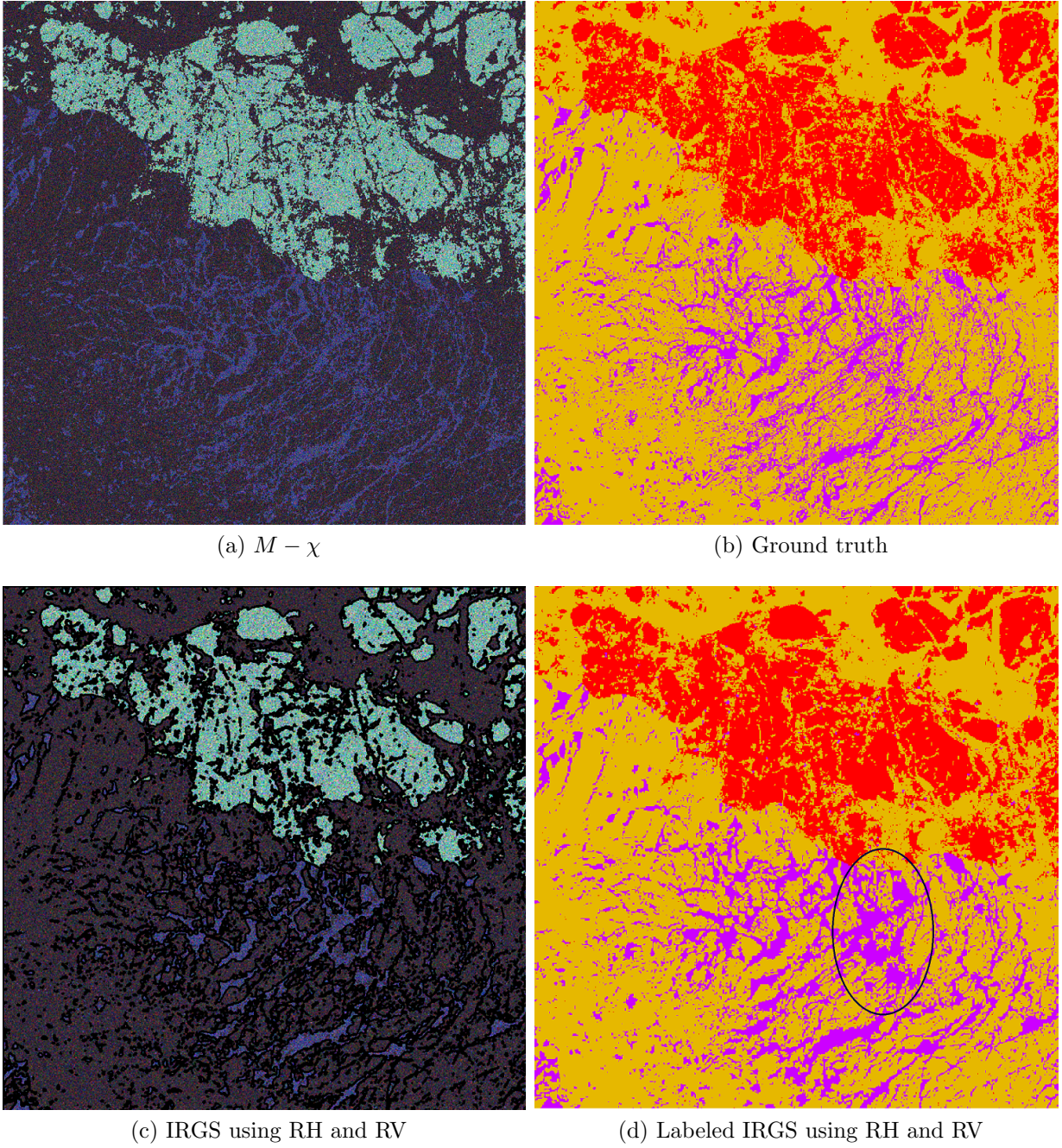
Figure 3.3: (a) The $M - \chi$ [18] RGB composite: R $= \sqrt{(mS_0 - S_3)/2}$ G $= \sqrt{S_0(1-m)}$ B $= \sqrt{(mS_0 + S_3)/2}$, where S_0, S_1, S_2, S_3 are the Stokes parameters and $m = \sqrt{S_1^2 + S_2^2 + S_3^2}/S_0$ is the degree of polarization, (b) ground truth, and the unsupervised segmentation and labeled images of the simulated MLC CP coherence data for (c)-(d) original IRGS segmentation using RH and RV images

55

(e) IRGS using $M - \chi$ (f) Labeled IRGS using $M - \chi$

■ YI   ■ FYI   ■ MYI

Figure 3.3: (e)-(f) The unsupervised segmentation and labeled images of the simulated MLC CP coherence data for original IRGS segmentation using $M - \chi$ parameters (cont.)

3.7.1 MLC CP images

Two RADARASAT-2 SLC QP images are used for testing. The images are acquired over Pond Inlet located in Northern Baffin Island. Pond Inlet is of importance in the Arctic in terms of sea-ice mapping support as it has the largest community in Northern Baffin Island. The scenes were collected on Dec 24, 2016 and Jan 31, 2017, identified here as Dec16 and Jan17. The sampled pixel and line spacing were 4.7m and 4.7m for the scene Dec16, and 4.7m and 5.1m for the scene Jan17, respectively. Fig. 3.2 depicts the RGB composites along with some example ice types labeled in the scenes.

Over each scene, CIS experts assigned class labels to pixels via the MAGIC software [56]. Based on the sample pixels, each of the ground truth maps was generated from an over-segmentation that was manually labeled. The incidence angle varies between 31° and 34° for the scene Dec16, and 38° and 41° for the scene Jan17. The scenes have a large overlap, however, the ice types in the scenes vary from one scene to the other. While the scene Dec16 consists of different ice types including new ice (NI), young ice (YI), first-year ice

(g) CP-IRGS using VFG
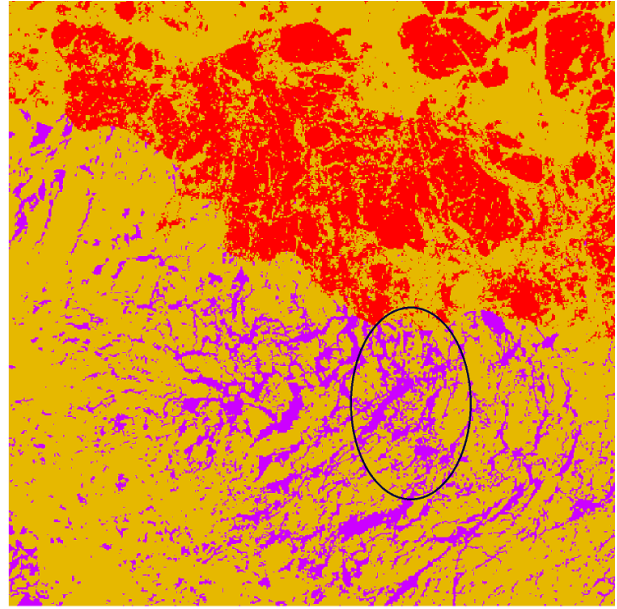
(h) Labeled CP-IRGS using VFG
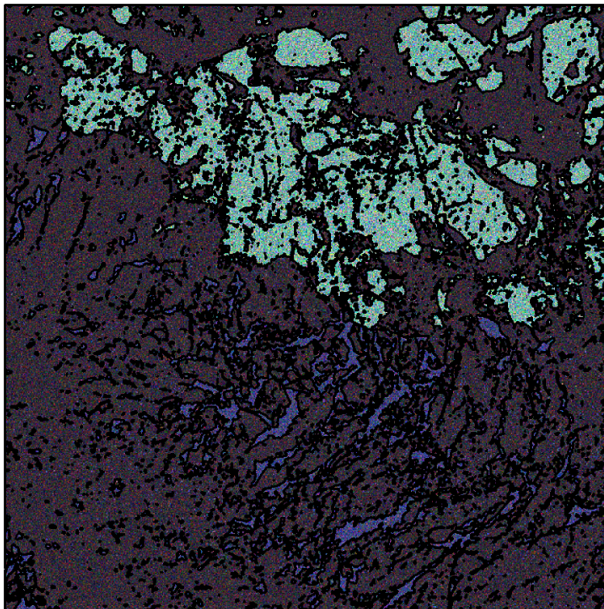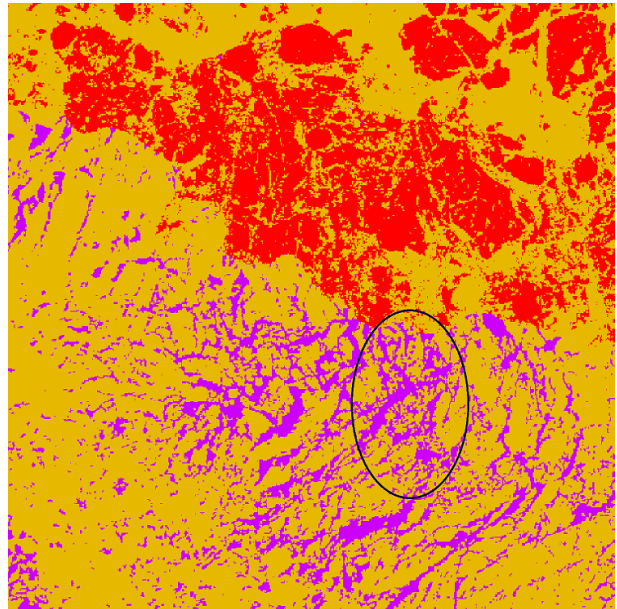
(i) CP-IRGS using CR

(j) Labeled CP-IRGS using CR

Figure 3.3: The unsupervised segmentation and labeled images of the simulated MLC CP coherence data for CP-IRGS segmentation using (g)-(h) VFG and (i)-(j) CR-based methods (cont.)

(FYI), and multi-year ice (MYI), due to the freeze-up process, the scene Jan17 includes only FYI and MYI.

The full QP images were used to synthesize the MLC CP coherence matrix data via an

(k) PolarIRGS using pseudo-QP   (l) Labeled PolarIRGS using pseudo-QP

YI   FYI   MYI
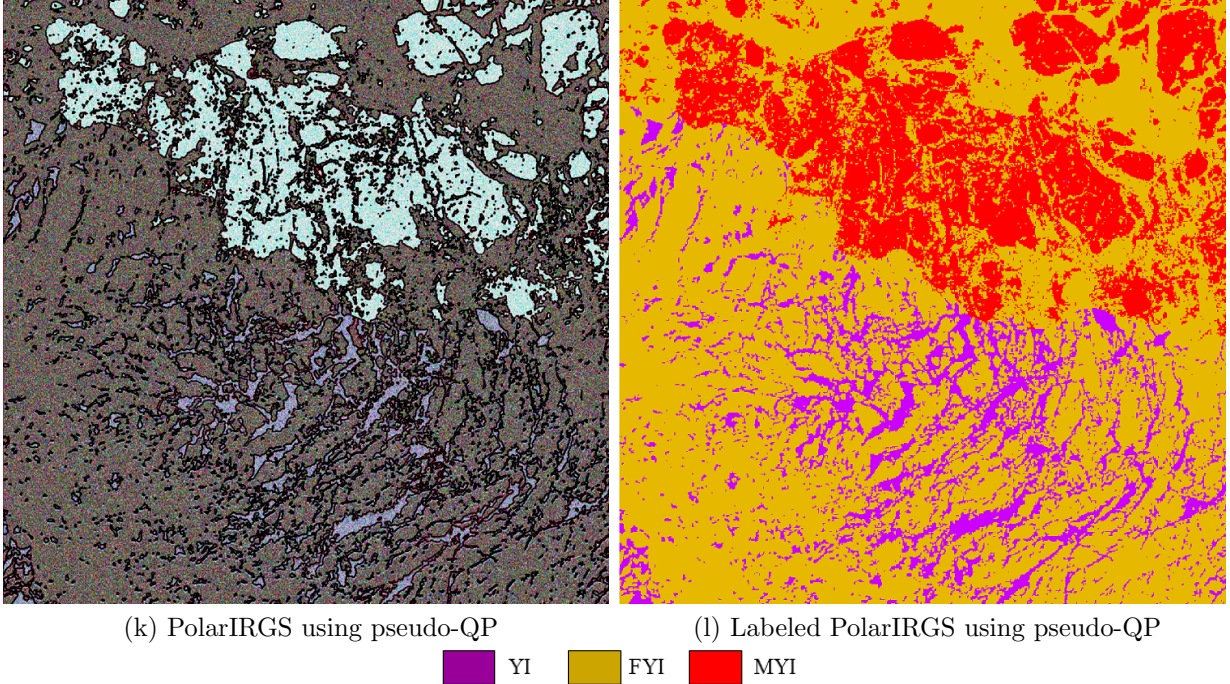
Figure 3.3: (k)-(l) The unsupervised segmentation overlaid on the reconstructed Pauli RGB composite and the labeled images of the simulated MLC CP coherence data for the reconstructed QP (pseudo-QP) from the simulated MLC CP coherence data using PolarIRGS segmentation method [21] (cont.)

RCM-data generator [4]. The simulator uses elements of the full QP scattering matrix to construct the complex CP measurement vector (3.1). The measurement vector was then used to generate the coherence matrix which was then resampled based on each beam mode of the RCM. Here, the CP coherence matrix data are in the medium resolution RCM mode with the pixel spacing of 50m×50m (range× azimuth). A "box-car" averaging with window size of 9×9 is also applied on the data which is used as the input to the unsupervised segmentation algorithm.

3.8   Results and Analyses

The results of the unsupervised segmentation methods, the labeled images, and the quantitative assessments of the methods are provided in this section. First, using a simulated

(a) $M - \chi$

(b) Ground truth

(c) IRGS using RH and RV

(d) Labeled IRGS using RH and RV

(e) IRGS using $M - \chi$
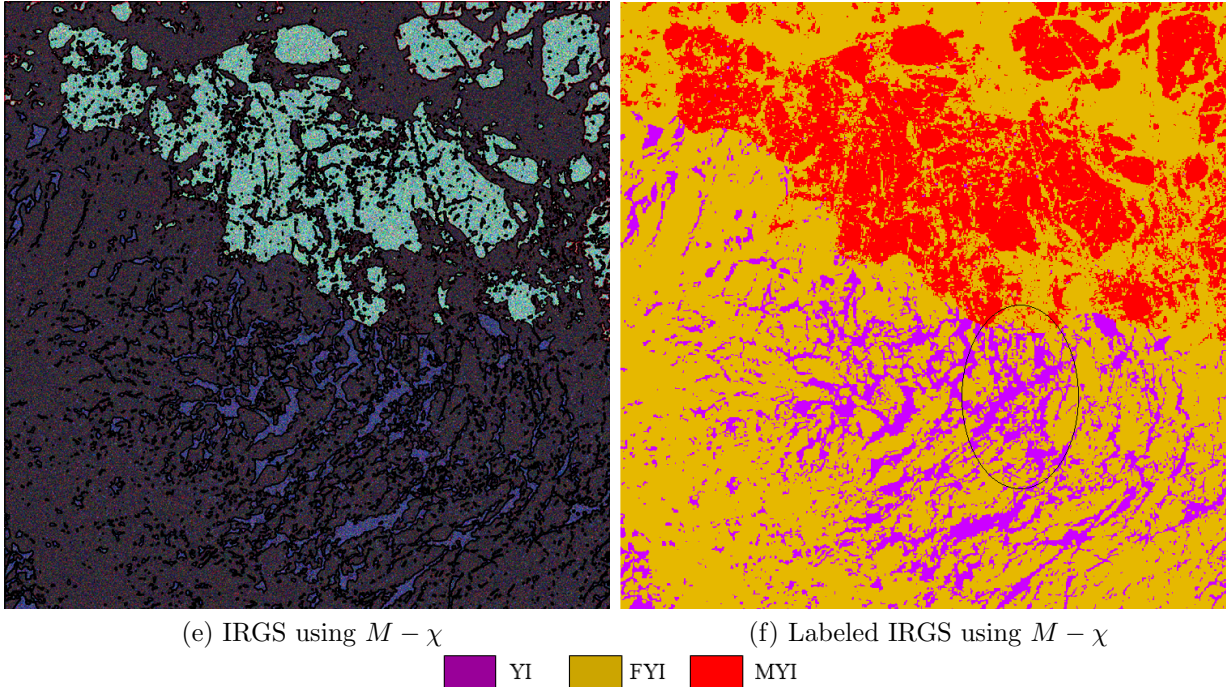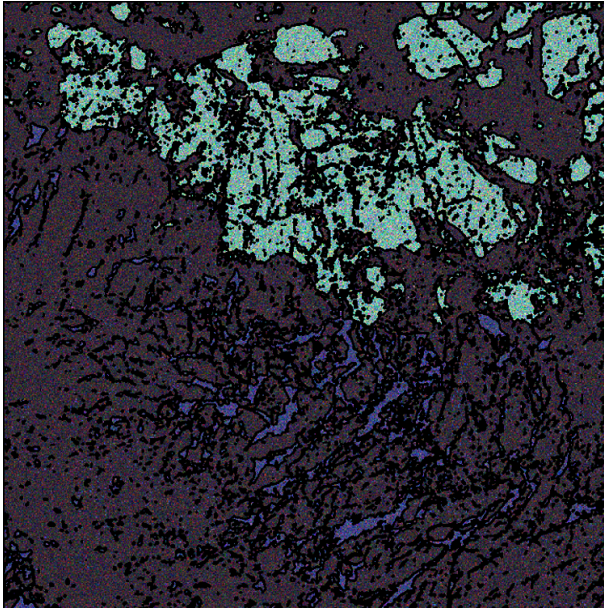
(f) Labeled IRGS using $M - \chi$
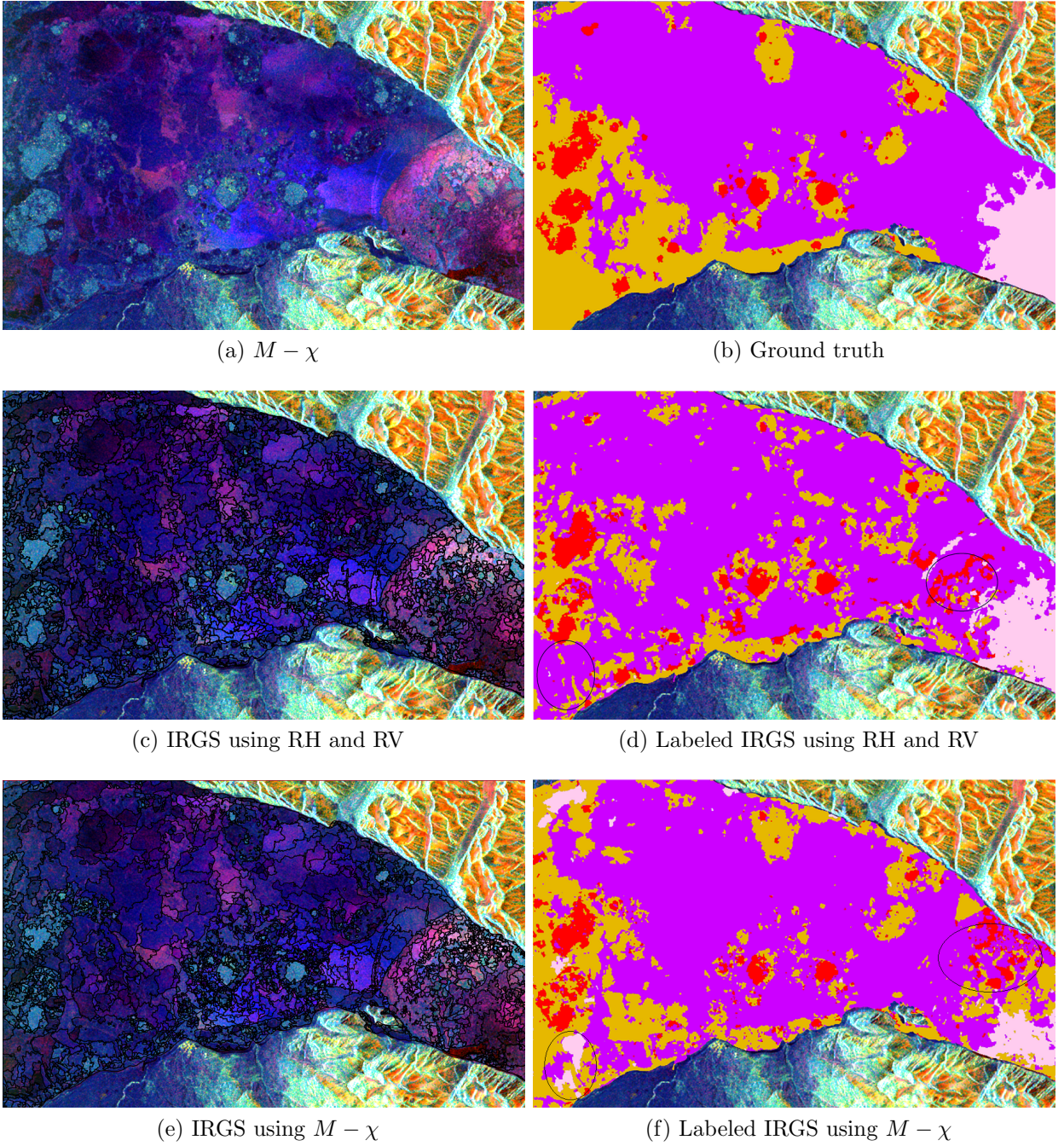
Figure 3.4: Scene Dec16: (a) the $M - \chi$ decomposition RGB composite: R $= \sqrt{(mS_0 - S_3)/2}$ G $= \sqrt{S_0(1 - m)}$ B $= \sqrt{(mS_0 + S_3)/2}$, where S_0, S_1, S_2, S_3 are the Stokes parameters and $m = \sqrt{S_1^2 + S_2^2 + S_3^2}/S_0$ is the degree of polarization, (b) ground truth, unsupervised segmentation, and the labeled images overlaid on top of land masks for the cases: (c)-(d) the unsupervised IRGS segmentation using RH and RV intensity images, and (e)-(f) the unsupervised IRGS segmentation using $M - \chi$ G and B parameters (cont.)
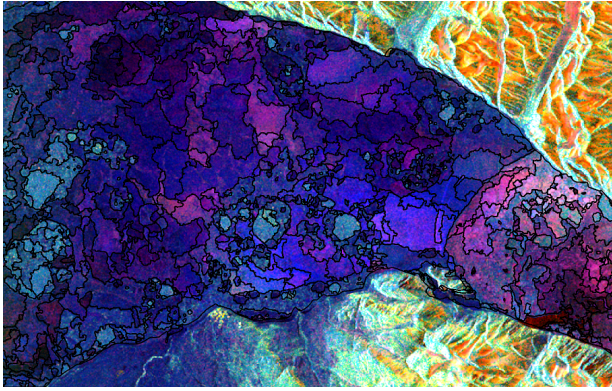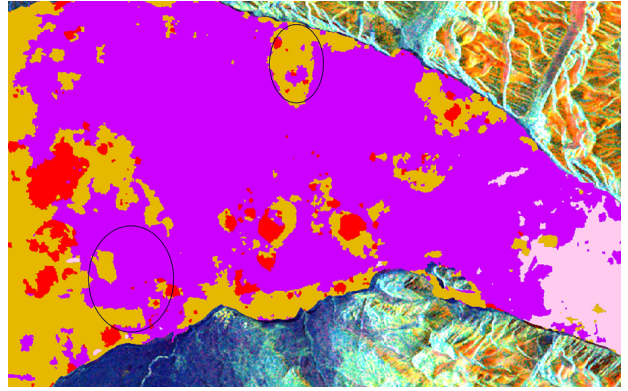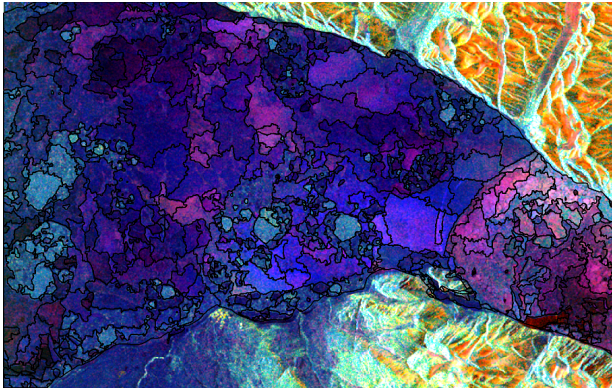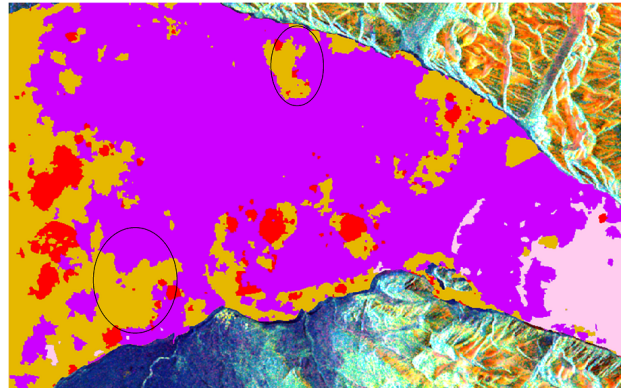
59

(g) CP-IRGS using VFG

(h) Labeled CP-IRGS using VFG

(i) CP-IRGS using CR

(j) Labeled CP-IRGS using CR
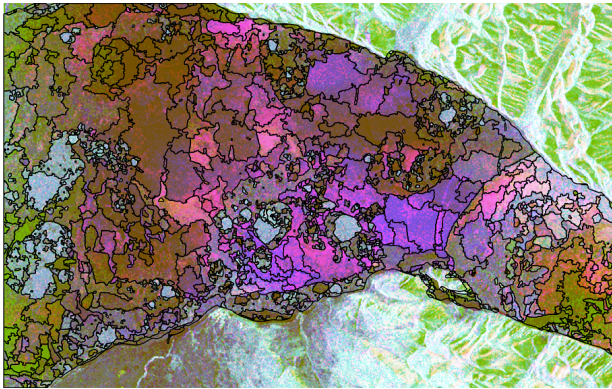
OW & NI   YI   FYI   MYI

(k) PolarIRGS using pseudo-QP

(l) Labeled PolarIRGS using pseudo-QP

OW & NI   YI   FYI   MYI

Figure 3.4: Scene Dec16: (g)-(h) CP-IRGS segmentation using VFG method, (i)-(j) CP-IRGS segmentation using CR-based method, and PolarIRGS segmentation using the reconstructed QP (pseudo-QP) from the simulated MLC CP coherence data overlaid on reconstructed Pauli RGB composite (cont.)

60

Table 3.2: Segmentation method, class accuracy values, the overall accuracy and the κ coefficient, as well as the number of regions in each segmentation image for the simulated and two RADARSAT-2 scenes.

Data Set	Measure	Class	IRGS Using RH and RV	CP-IRGS Using VFG	CP-IRGS Using CR
Simulated Scene	User's Accuracy	OW/NI	-	-	-
		YI	80.03	**90.32**	89.23
		FYI	**97.71**	97.06	96.86
		MYI	95.69	**99.31**	98.37
	Overall Accuracy (%)		94.78	**96.72**	96.26
	Kappa Coefficient		0.90	**0.93**	0.92
	Number of Regions		4285	4144	**3794**
Scene Dec16	User's Accuracy	OW/NI	78.34	86.16	**87.49**
		YI	60.76	**71.37**	71.24
		FYI	60.11	76.94	**82.76**
		MYI	88.99	**90.26**	86.93
	Overall Accuracy (%)		74.63	82.58	**83.27**
	Kappa Coefficient		0.49	0.66	**0.68**
	Number of Regions		3779	1063	**953**
Scene Jan17	User's Accuracy	OW/NI	-	-	-
		YI	-	-	-
		FYI	98.06	**99.45**	99.29
		MYI	**92.25**	85.60	90.48
	Overall Accuracy (%)		97.48	97.76	**98.29**
	Kappa Coefficient		0.87	0.89	**0.91**
	Number of Regions		2816	2213	**2069**

MLC CP image, and, second, using the two MLC CP images described in Section 3.7.1, we compare the three segmentation methods in terms of accuracy as well as the level of oversegmentation.

(a) $M - \chi$

(b) Ground truth

(c) IRGS using RH and RV

(d) Labeled IRGS using RH and RV

(e) IRGS using $M - \chi$

(f) Labeled IRGS using $M - \chi$
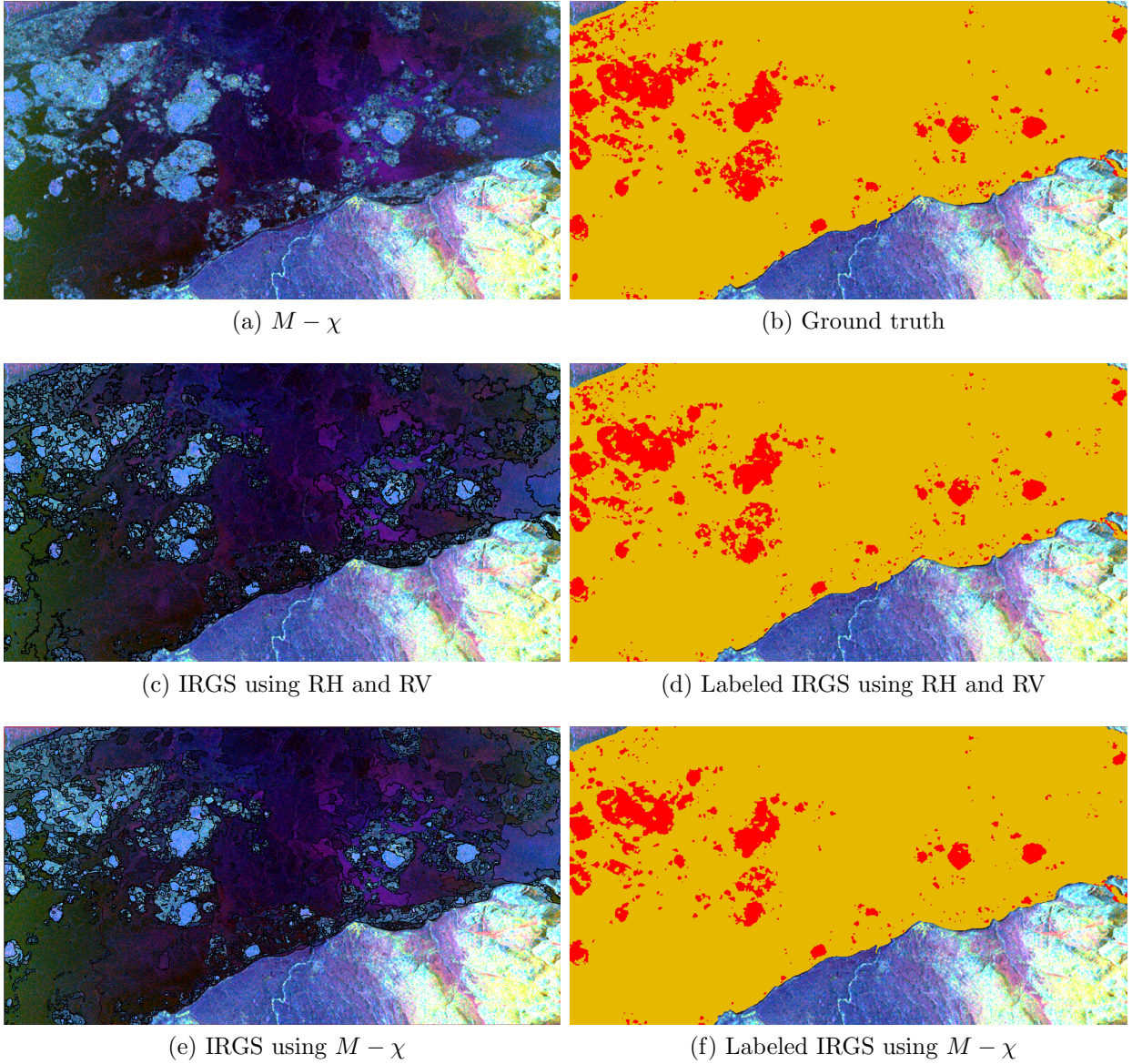
Figure 3.5: Scene Jan17: (a) the $M - \chi$ decomposition RGB composite: R $=$ $\sqrt{(mS_0 - S_3)/2}$ G $= \sqrt{S_0(1 - m)}$ B $= \sqrt{(mS_0 + S_3)/2}$, where S_0, S_1, S_2, S_3 are the Stokes parameters and $m = \sqrt{S_1^2 + S_2^2 + S_3^2}/S_0$ is the degree of polarization, (b) ground truth, unsupervised segmentation, and the labeled images overlaid on top of land masks for the cases: (c)-(d) the unsupervised IRGS segmentation using RH and RV intensity images, and (e)-(f) the unsupervised IRGS segmentation using $M - \chi$ G and B parameters.

62

(g) CP-IRGS using VFG

(h) Labeled CP-IRGS using VFG

(i) CP-IRGS using CR

(j) Labeled CP-IRGS using CR

OW & NI YI FYI MYI

(k) PolarIRGS using pseudo-QP

(l) Labeled PolarIRGS using pseudo-QP

OW & NI YI FYI MYI
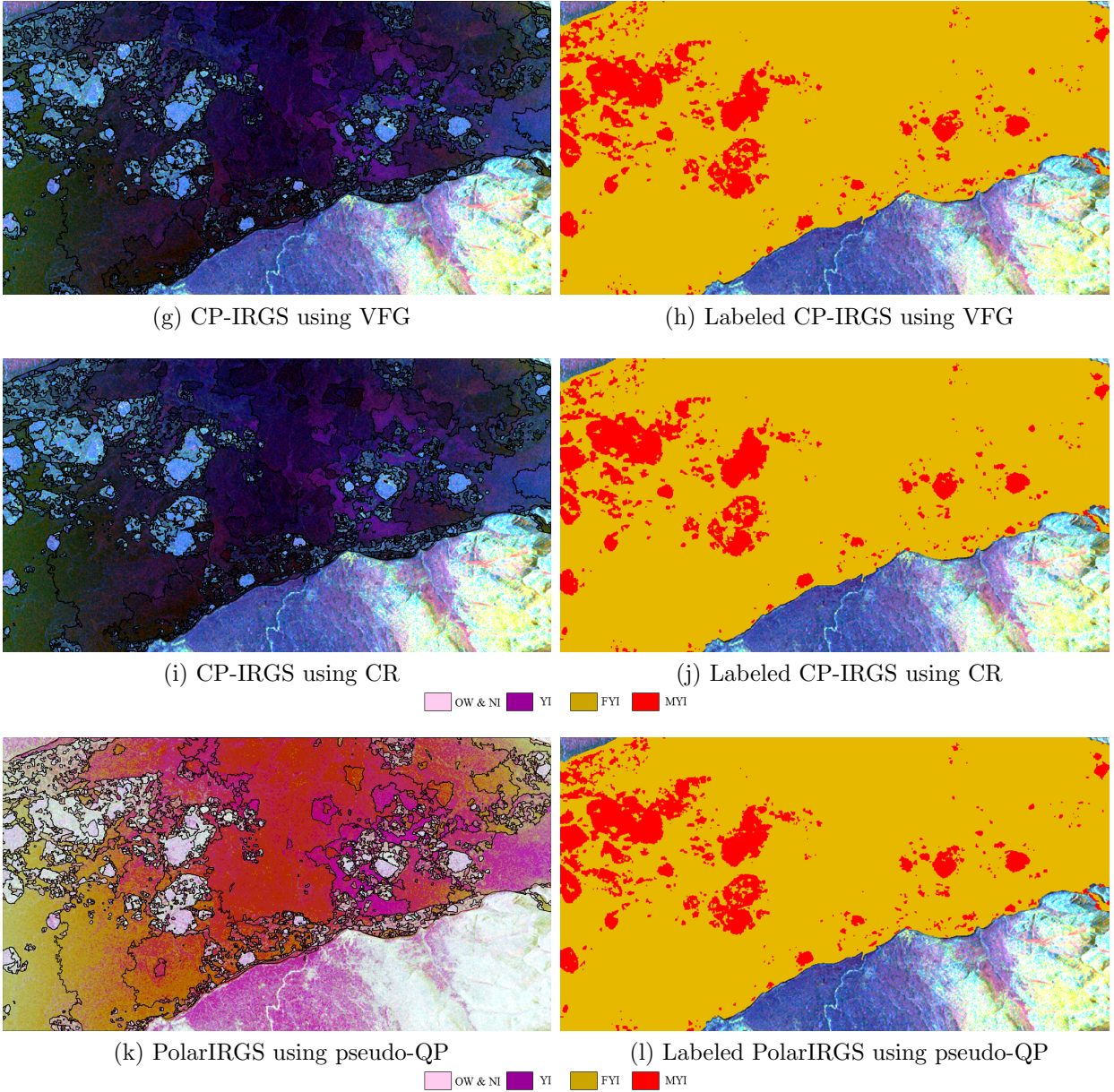
Figure 3.5: Scene Jan17: (g)-(h) CP-IRGS segmentation using VFG method, (i)-(j) CP-IRGS segmentation using CR-based method, and PolarIRGS segmentation using the reconstructed QP (pseudo-QP) from the simulated MLC CP coherence data overlaid on reconstructed Pauli RGB composite (cont.)

3.8.1 Results using the simulated MLC CP data

Here, the results of the simulated MLC CP scene including the unsupervised segmentation images as well as their corresponding labeled images are provided. The $M - \chi$ decomposition RGB composite [18] image of the scene is shown in Fig. 3.3 (a). The results of the

unsupervised segmentation methods in the three cases described in Section 3.6 overlaid on the RGB image as well as their corresponding labeled images are also presented in Fig. 3.3. All the three segmentation methods provided relatively accurate and identical results as shown in Fig. 3.3 and also supported by the quantitative results in Table 3.2 where accuracy in the three cases does not significantly vary from one method to the other.

Other than the three cases described in Section 3.6, the segmentation results using $M - \chi$ parameters, derived from Stokes vector, were also provided. This allows for a comparison between these Stokes vector-derived features with CP intensities in unsupervised segmentation. Two of the three $M - \chi$ parameters that were more discriminative (the parameters G and B from $M - \chi$ RGB composite) were selected. These parameters were then used in Case 1 experiment. In particular, in Case 1, $M - \chi$ parameters G and B were used in the standard IRGS algorithm. Fig. 3.3 (e)-(f) shows the segmentation boundaries and the corresponding ice-type labeled image using these parameters.

Moreover, the segmentation and labeled images using the reconstructed QP from CP data (pseudo-QP data) were also provided in Fig. 3.3. The intention is to compare the performance of pseudo-QP data with directly using 2×2 CP coherence matrix data. The pseudo-QP data was reconstructed from the simulated MLC CP coherence matrix data using Nord's reconstruction method [39], which was described in Section 2.3. PolarIRGS method [21] was performed on the pseudo-QP data. Fig. 3.3 (k) shows the segmentation boundaries overlaid on top of the Paul RGB composite formed from the pseudo-QP data. The corresponding ice-type labeled image was provided in Fig. 3.3 (l).

According to the values OA, κ, and the total number regions, CP-IRGS provides more accurate results with less number of regions than the original IRGS segmentation using RH and RV intensities (Case 1). As delineated in ovals in Fig. 3.3 (e)-(h), a fairly large number of FYI pixels in the middle of the scene are mislabeled as YI using original IRGS. This is also demonstrated in the relatively low accuracy of YI class for this case, 80.03%, as seen in Table 3.2. The performance of CP-IRGS using VFG and CR-based methods indicates no significant difference where the VFG method provides higher accuracy, however, larger number of regions than the CR-based approach as seen in Table 3.2.

3.8.2 Results of the MLC CP data

Since scene Dec16 consists of different ice types, this scene is more challenging than scene Jan17 for segmentation. As labeled in Fig. 3.2 and as shown in the ground truth image of scene Dec16 in Fig. 3.4 (b), the areas covered by YI have totally different radar backscatter across the scene. Also, the ice types YI and FYI in the left part of the scene are very similar

Table 3.3: Segmentation method, the overall accuracy and the κ coefficient, as well as the number of regions in each segmentation image for the simulated and two real MLC CP scenes. The comparison of CP-IRGS segmentation results using CP RH and RV intensities versus $M - \chi$ parameters against PolarIRGS [21] segmentation results using the reconstructed QP (pseudo-QP) data

Data Set	Measure	IRGS RH, RV	IRGS $M - \chi$	CP-IRGS VFG RH, RV	CP-IRGS VFG $M - \chi$	PolarIRGS pseudo-QP
Simulated Scene	OA (%)	94.78	96.07	96.72	96.16	96.65
	Kappa	0.90	0.92	0.93	0.85	0.93
	No Regions	4284	3751	4144	4206	4176
Scene Dec16	OA (%)	74.63	76.08	82.57	84.57	80.84
	Kappa	0.49	0.54	0.66	0.70	0.62
	No Regions	3779	5642	1063	1089	1759
Scene Jan17	OA (%)	97.48	96.66	97.76	96.16	97.30
	Kappa	0.87	0.81	0.89	0.77	0.87
	No Regions	2816	2858	2213	2247	2109

in backscatter. However, scene Jan17 only consists of FYI and MYI that seem to be much more distinguishable for the segmentation algorithm. In Fig. 3.4, the $M - \chi$ decomposition image of scene Dec16, the ground truth, and the unsupervised segmentation results, as well as the labeled images to the real ice types are provided for the three different methods in Cases 1, 2, and 3 discussed in Section 3.6. Moreover, Fig. 3.4 (e)-(f) shows the segmentation boundaries and the corresponding labeled image using $M - \chi$ parameters. Also, Fig. 3.4 (i)-(j) depicts PolarIRGS segmentation boundaries overlaid on top of the Paul RGB composite formed from the pseudo-QP data and the labeled image.

As seen in the highlighted ovals in the labeled images in Fig. 3.4, the results of the CP-IRGS algorithm (Fig. 3.4 (f) and (h)) provide better discrimination between YI and FYI classes all over the scene compared to the IRGS results using RH and RV intensities (Fig. 3.4 (d)). However, there are some misclassified areas highlighted in the left part of the scene for the results of the CP-IRGS algorithm, Fig. 3.4 (f) and (h). Although the segmentation images by the IRGS algorithm using RH and RV intensities in Fig. 3.4 (c) is much more oversegmented than the CP-IRGS segmentation images in Fig. 3.4 (e) and (g), the CP-IRGS algorithm produces more accurate labeled images than the IRGS algorithm, as supported by the accuracy values in Table 3.2.

This demonstrates that the CP-IRGS algorithm produces segmentation classes that are

more homogeneous than those in the segmentation by the original IRGS algorithm using RH and RV intensities. In other words, some segmentation classes produced by the original IRGS algorithm using only RH and RV intensities include multiple ice types (are not purely from one ice type), and the majority voting process of labeling assigns only one ice type to all the regions in the segmentation class. However, the CP-IRGS algorithm produces more pure segmentation classes by leveraging the statistical characteristics of the MLC CP coherence data. Moreover, for scene Dec16, the CP-IRGS using CR produces slightly better labeling results than the CP-IRGS method using VFG (slightly higher overall accuracy and smaller number of regions using CR-based method than the VFG method).

The unsupervised segmentation and the labeled images for scene Jan17 are also shown in Fig. 3.5. All the three segmentation methods provide highly accurate discrimination between the two classes FYI and MYI in the scene. This is because this scene only consists of two ice types that are easily distinguishable by the segmentation algorithms due to the noticeable backscatter difference between classes. Thus, the phase information provided by the MLC CP data might be unnecessary particularly for this scene, and the original IRGS using only RH and RV intensities produces highly accurate results.

Table 3.3 also shows the segmentation performance using $M - \chi$ parameters in comparison with using CP intensities. These results were obtained using the parameters G and B from $M - \chi$ RGB composite were used in Case 1 and Case 2 experiments. In particular, in Case 1, $M - \chi$ parameters G and B were used in the standard IRGS algorithm, and in Case 2, these parameters were used in VFG method. According to Table 3.3, the accuracy-based assessment of the comparison results demonstrated that $M - \chi$ parameters do not consistently provide better results than CP intensities. Investigation of using other CP-derived parameters in unsupervised segmentation remains as a line of future work.

The last column of Table 3.3 shows the performance of PolarIRGS segmentation [21] using pseudo-QP data. According to Table 3.3, the quantitative assessment of the segmentation performance using pseudo-QP data for the application of ice mapping indicates that using pseudo-QP data, segmentation results are almost as accurate as directly using 2×2 CP MLC coherence matrix data. However, since the symmetry assumptions in the reconstruction of QP data might not be always valid, and may pose uncertainties, it is always preferred to directly use 2×2 CP coherence matrix data. Therefore, in any complex QP-based segmentation algorithm, which is developed based on 3×3 QP MLC covariance matrix, the QP MLC covariance matrix should be replaced with the 2CP MLC coherence matrix.

3.9   Summary

In this chapter, an unsupervised segmentation algorithm using complex CP data is proposed. This is the first region-based unsupervised segmentation that uses complex CP statistical properties. The algorithm, called CP-IRGS, is developed based on the well-known IRGS algorithm which exploits edge strength information in a region-growing approach using MRFs. MLC CP data is extracted from the complex measurement of the backscattered field of a CP SAR. It was demonstrated that the MLC data is complex Wishart distributed, based on which the unary potential in CP-IRGS was derived. In the pairwise potential, using a complex CP divergence measure in a bi-window configuration, an edge strength calculation method was proposed.

Only this limited number of QP scenes of sea-ice with CIS ice labels were available for this thesis. Future work involves applying the proposed unsupervised segmentation on a more extensive QP SAR scene data set which would lead to more certain conclusions. However, The results on CP sea-ice scenes demonstrate that the the proposed CP-IRGS performs a better segmentation than IRGS that only uses the RH and RV intensity images. Also, the quantitative assessment of the segmentation results using the two edge strength calculation methods, VFG and CR, indicates for complex scenes where the noise strength is high, the CR method generates segmentation results that are slightly more accurate. However, overall, no significant difference between the quantitative results of the two algorithms were seen in the experimental results.

In the CR-based method, the data used are the complex CP coherence matrix data, which includes intensity as well as phase information. This is advantageous over the VFG method which only uses RH and RV intensity data. However, the performance of CP-IRGS using the two edge strength calculation methods (VFG and CR) are comparable in all the three cases of experiments. This indicates the effectiveness of the VFG method in defining edge strength values. Therefore, developing a version of VFG method that uses complex CP coherence matrix data as input might be an interesting line of future work.

Chapter 4

Semi-Supervised Land-Cover Classification Methodology

The MLC CP data have similar properties to the MLC QP data. In this chapter, a land cover classification method using spatial information is designed based on the statistical characteristics of the complex CP and QP SAR data. First, the local spatial correlation among image pixels is captured by superpixels (segmentation regions). Second, a graph is constructed on the superpixels to model the global spatial correlation among superpixels. The land cover classification image with ground truth labels are then estimated by propagating labels from the few labeled superpixels to the unlabeled superpixels. In this chapter, real RCM complex CP and QP scenes are used to evaluate the performance of the proposed classification method. This chapter is based on a paper submitted to a journal [25].

4.1 Introduction

Land cover classification is an important task in monitoring the Earth's surface. The high-resolution RCM complex SAR data can be used for land cover classification [6]. QP SAR data has the full information acquired by a polarimetric SAR, however, the swaths covered by a QP SAR are relatively small. Therefore, CP SAR is an attractive alternative since, as demonstrated by many studies [4,13,23,44], CP classifications are comparable to those from a QP SAR, and the RCM CP scenes can be acquired in wide swaths ($\sim$350 km) which are more suitable for studying larger earth regions. Many studies on land cover classification using SAR data are dedicated to QP SAR data [84–87], and there has been

very limited work on CP land cover classification [88,89]. In this chapter, we propose a land cover classification method that models the "local" (using a superpixel-based approach) and "global" (using a graph-based formulation) spatial correlation information in the QP and CP SAR data types.

Using superpixels [90] is advocated in computer vision algorithms since compared with the rigid pixel representation of images, a superpixel representation utilizes the "local" spatial correlation between adjacent pixels and, by forming pixel groups, greatly reduces the number of image primitives [91–93]. A superpixel segmentation algorithm is expected to preserve the image boundaries by generating homogeneous superpixels that contain only one surface object type [93]. Moreover, the superpixel segmentation should be adaptive, in that it should capture the important local details without having to utilize many superpixels in homogeneous regions [94]. Our proposed segmentation algorithm utilizes statistical properties of QP and CP SAR data calculated based on superpixels.

Coherent acquisition of the backscatter in a CP SAR allows for constructing the Stokes vector, or equivalently, the 2×2 complex coherence matrix. By averaging several independent CP single-look complex (SLC) coherence matrices, the multilook complex (MLC) coherence matrix is calculated. Both the CP 2×2 MLC coherence and the QP 3×3 MLC covariance matrices have a complex Wishart distribution [95]. Based on this characteristic of the QP MLC covariance and CP MLC coherence matrices, Yu *et al.* [21] and Ghanbari *et al.* [95], proposed QP SAR and CP SAR extensions of an unsupervised segmentation algorithm called Iterative Region Growing with Semantics (IRGS).

PolarIRGS (full polarimetric IRGS) [21] and CP-IRGS (compact polarimetric IRGS) [95] utilize the statistical properties of the QP and CP MLC data types in both the unary and pairwise potentials of IRGS. IRGS is superpixel-based, in that the statistical properties of superpixels are used, and, as a result, it is less sensitive to speckle noise and incidence angle induced spatial non-stationarities in SAR images [11]. Also, IRGS uses edge strength in its formulation to assist determining when adjacent superpixels should be merged [20]. These characteristics make PolarIRGS and CP-IRGS algorithms effective for superpixel segmentation. PolarIRGS and CP-IRGS model local spatial relationship using edge strength and information from neighboring superpixels.

The superpixels are then used in a graph-based classification approach. Considering each superpixel as a vertex, a fully-connected undirected graph is constructed on the superpixels to model the "global" spatial correlation between superpixels. Once the graph is constructed, learning involves assigning labels to the superpixels. Given a few labeled superpixels, graph learning is performed in a semi-supervised manner. In a semi-supervised method, the information from labeled as well as unlabeled superpixels is used to predict the

labels of unlabeled superpixels [96]. The advantage of this method is that a very limited number of superpixels are needed to be labeled [97].

A semi-supervised graph learning is based on the assumption that the vertices connected by a high-similarity edge are likely to have the same label [98]. In essence, the labels of labeled data propagate to the unlabeled data according to the adjacency information of the graph vertices [99]. Inspired by the recent work on hyperspectral classification by Sellars *et al.* [97] and Jia *et al.* [100], in this chapter, we propose semi-supervised fully-connected graph learning based on label propagation [99] for complex QP and CP SAR data. The adjacency relationship between the superpixels is measured by a metric that consists of two components: spatial and backscatter difference. While the spatial difference is based on the spatial distance between superpixel centroids, the backscatter distance is measured by statistical significance between MLC matrices [71].

In summary, we have designed, implemented, and tested a scene classification approach that coherently models the *local and global spatial* (LGS) correlation using MLC QP and CP via superpixels and a graph-based approach. The novel approach involves semi-supervised fully-connected graph learning to classify superpixels by modeling the global correlation among all scene superpixels. The graph-based approach uniquely characterizes superpixel differences by spatial distance and statistical properties of MLC matrices.

4.2 Related Work

Recently, the incorporation of spatial correlation among pixels in image classification methods has drawn increasing attention [100–102]. In general, studies have incorporated spatial correlation information in classification in two main categories: (1) using derived features for classification and (2) designing a classification method that inherently incorporates spatial correlation. In the first category, "hand-crafted" texture features based on gray-level co-occurrence matrices (GLCM) [103, 104] and Gabor filters [105] are extracted and used in classification. To overcome the difficulties in effective feature representation, deep convolutional neural networks (CNNs) inherently learn features [102, 106, 107].

In the second category, the spatial correlation effect is embodied in the classification method [100, 108, 109]. Remote sensing image classification methods inherently incorporating spatial correlation effect are based on either pixels or superpixels. Chen *et al.* [108] proposed an image classification method using sparse representation, where the spatial correlation between a pixel and its neighbors is represented by a sparse linear combination of a few common training samples in the feature space induced by a kernel function [108].

In another pixel-based classification method [110], a hypergraph constructed on image pixels with spatial and spectral hyperedges was used in a semi-supervised method for image classification.

In more recent studies, image classification based on superpixels has attracted significant interest. In a study by Li *et al.* [111], by incorporating the local spatial correlation using superpixels, while avoiding the undersegmentation problem of superpixel segmentation algorithm, both pixel-level and superpixel-level probability maps were derived, and, using an adaptive probabilistic fusion model, the joint probability maps were calculated. Then, the maximization optimization problem were transformed to an energy minimization problem, which was iteratively solved to obtain the final classification map. To overcome the high computation demand of CNNs, Lv *et al.* proposed superpixel CNN classification [109]. They compared various superpixel segmentation methods while using different-scale deep CNN features. Recently, a graph was constructed on superpixels generated from a hyperspectral imge using the entropy rate segmentation method [100]. Then, an adaptive version of the dynamic label propagation method [112] was designed to pass labels from labeled to unlabeled superpixels.

There have been numerous studies in the literature on land cover classification using SAR data. In a study [84], using single-polarized SAR images, Esch *et al.* demonstrated the analysis of mean and standard deviation of local backscatter values provided valuable information in differentiating different land cover types such as water, open land, woodland, and urban areas. A deep convolutional autoencoder was developed by Geng *et al.* [106] for land cover classification. Using a single-polarization SAR image, they demonstrated the superiority of features automatically derived by the autoencoder over the hand-crafted GLCM and Gabor features. In another work [113] using single-polarized SAR images, a superpixel segmentation through a probabilistic model based on the amplitude SAR statistics was developed. It was demonstrated that their method, which utilizes amplitude ratio distance, provides better land cover classification results than the other methods, which mostly use Gaussian kernels to measure the similarity between pixel intensities.

Majority of recent studies on SAR land cover classification exploit the polarimetric information of full QP and CP SAR data. Ohki *et al.* [89] investigated large-scale classification of land cover types such as forest, rice paddy, grass, urban area, and water using three different SAR data types including linear DP, CP, and full QP. In their studies, the support vector machine (SVM), random forest (RF), and a neural-network-based classifier were employed. They indicated that the experiment with some selective QP SAR features provides the most accurate classification results with a maximum overall accuracy of 73.4%. Huang *et al.* [85] applied a deep neural network based on reinforcement learning called deep Q-network [114] for QP SAR image classification using extracted target decomposition fea-
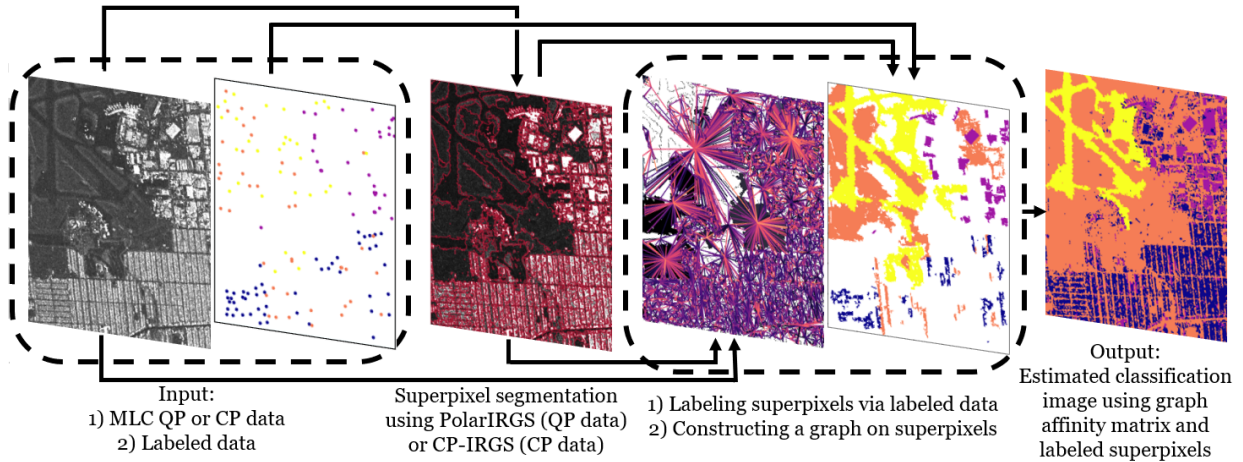
Figure 4.1: General block diagram of the proposed land cover classification method.

tures as the input data, and demonstrated that the method achieves the same accuracy as the compared deep-learning-based methods with a relatively smaller labeled data size. In another attempt to address the classification with limited amount of labeled data, a CNN classification inspired by principal component analysis network [115] is designed by Guo *et al.* [116].

With regard to capturing spatial correlation as well as accounting for the polarimetric response variation by target orientation in QP SAR data, a dynamic texture based on the sequence of polarimetric responses was employed in a work by Yang *et al.* [86]. In a QP SAR classification of land cover by Zou *et al.* [117], the spatial information in the parameters of a target decomposition in pixel-level (using morphological operators) and superpixel-level (using a semantic indicator derived from the graph constructed on the superpixels) is incorporated. To exploit the spatial correlation among neighboring pixels in the process of dimensionality reduction in QP-SAR-derived features, graph embedding [118] was used in a tensor-based representation [87].

Over the past decade, semi-supervised classification of QP SAR data has been used by many researchers to exploit both labeled and unlabeled data information to obtain accurate classifications using limited labeled samples. Studies on semi-supervised classification of QP SAR data include various methods mostly in a pixel-based manner. Wei *et al.* [119] proposed a QP SAR semi-supervised classification based on a graph to capture the high-order relationship between hypergraph vertices. Using image pixels as the hypergraph

72

vertices and the Gaussian kernel as the similarity measure, they applied a regularization framework [120] to find the labels. Hou *et al.* developed a graph-based semi-supervised classification that incorporates the spatial consistency of labels using a Gaussian field model [121] as a regularizer in the optimization framework. The classifier was proposed to deal with the impurity of QP SAR pixels—containing more than one land cover type—and inaccurate labeled data [122].

A QP SAR semi-supervised classification method was implemented based on co-training, which utilizes two different classifiers with distinct feature spaces to boost the data reliability [123]. Superpixels were only used in the selection of reliable unlabeled data to enlarge the labeled data. Unlike co-training, in another multi-view learning approach, a multi-attribute graph model was developed by Liu *et al.* [124] for QP SAR land cover classification. In their method, the QP-derived features were divided into attribute groups, and multiple graphs were constructed on the attribute groups. Then, after the spatial correlation effect was modeled as a term in their objective function, a weight for each graph and the label of unlabeled pixels were optimized [124]. Following the idea of increasing the diversity of classification, Wang *et al.* [125] proposed a tri-training-based algorithm where three groups of QP-derived features were used to train three different classifiers. The spatial information was utilized in the selection process of reliable unlabeled data for adding to the labeled data.

In some recent semi-supervised classification studies, investigators exploited CNNs while modeling the spatial correlation effect in their framework. A CNN classification network incorporates two semantic priors to preserve the spatial consistency and boundaries [126]. Active learning has also been integrated into a CNN-based architecture [127] to select the most informative training data for annotation based on the CNN's output. Also, a Markov random field (MRF) model was applied to the output probability maps of the CNN to encourage the spatial consistency. Gadhiya *et al.* [128] utilized the information of each pixel as well as the containing superpixel in a Wishart network [129]. A few methods also aimed to integrate superpixel-driven information into the deep neural networks [130, 131]. Other QP semi-supervised classification methods based on CNNs either perform on a pixel-level basis, or they lack an effective model for spatial correlation effect [132, 133]. Recently, a multi-scale graph constructed on superpixels to overcome the limitations of pixel-based classification techniques [134].

From this discussion, we recognize the following shortcomings based on observations drawn from the research literature:

1) There is a limited number of CP land cover classification studies, despite a great deal of land cover classification using QP data.

2) Research using correlation among superpixels in SAR images in a graph-based approach is limited. We are not aware of published methods that learn the global correlation using superpixel-based graphs for the purpose of SAR land cover classification.

3) Superpixel segmentation methods used in the land cover classification studies are generic and do not account for the statistical properties of QP SAR data.

We implement a method that is able to address these shortcomings:

1) We design and implement a land cover classification method for CP complex data that is also applicable to complex QP.

2) This method utilizes the local spatial information via superpixels. A graph-learning method is then developed to effectively model the global spatial correlation among the superpixels.

3) The statistical properties of QP and CP SAR data are used to perform the superpixel segmentation.

4.3 Complex CP and QP SAR

In an SLC CP SAR data set, the measurements are the elements of a complex vector $\mathbf{E}$ that corresponds to the backscattered field. The radar scattering matrix $\mathbf{S}$ relates the incident field to the backscattered field [30]:

$$\mathbf{E}_r = \begin{bmatrix} E_H \\ E_V \end{bmatrix} = \mathbf{S}\hat{\mathbf{u}}_t = \begin{bmatrix} S_{HH} & S_{HV} \\ S_{VH} & S_{VV} \end{bmatrix} \hat{\mathbf{u}}_t \tag{4.1}$$

where $\hat{\mathbf{u}}_t$ is the unit Jones vector related to the incident field and $\mathbf{E}_r$ is the backscattered field that is shown by $\mathbf{E}_{CP}$ in CP SAR case. The measurement in the case of an SLC QP SAR data set is the scattering matrix $\mathbf{S}$ in Eq. (4.1) which can be represented as a vector using the lexicographic basis set as $\mathbf{\Omega}_{QP} = [S_{HH} \quad \sqrt{2}S_{HV} \quad S_{VV}]$ when the reciprocity assumption, $S_{HV} = S_{VH}$, holds.

By multiplying $\mathbf{E}_{CP}$ and $\mathbf{\Omega}_{QP}$ by their Hermitian conjugates, the Hermitian positive semidefinite MLC CP coherence ($\mathbf{C}_{CP}$) and QP covariance ($\mathbf{C}_{QP}$) matrices are derived,

respectively [30, 32]

$$\mathbf{C}_{CP} = \frac{1}{L} \sum_{i=1}^{L} \mathbf{E}_{CP_i} \mathbf{E}_{CP_i}^{\dagger} = \begin{bmatrix} \langle |E_H|^2 \rangle & \langle E_H E_V^* \rangle \\ \langle E_V E_H^* \rangle & \langle |E_V|^2 \rangle \end{bmatrix} \tag{4.2}$$

$$\mathbf{C}_{QP} = \frac{1}{L} \sum_{i=1}^{L} \mathbf{\Omega}_{QP_i} \mathbf{\Omega}_{QP_i}^{\dagger}$$
$$= \begin{bmatrix} \langle |S_{HH}|^2 \rangle & \sqrt{2} \langle S_{HH} S_{HV}^* \rangle & \langle S_{HH} S_{VV}^* \rangle \\ \sqrt{2} \langle S_{HV} S_{HH}^* \rangle & 2 \langle |S_{HV}|^2 \rangle & \sqrt{2} \langle S_{HV} S_{VV}^* \rangle \\ \langle S_{VV} S_{HH}^* \rangle & \sqrt{2} \langle S_{VV} S_{HV}^* \rangle & \langle |S_{VV}|^2 \rangle \end{bmatrix} \tag{4.3}$$

where $< \cdots >$ shows temporal or spatial averaging, $\dagger$ indicates Hermitian conjugate, $*$ is complex conjugate, and L is the number of looks used for averaging. The matrices $\sum_{i=1}^{L} \mathbf{E}_{CP_i} \mathbf{E}_{CP_i}^{*T}$ and $\sum_{i=1}^{L} \mathbf{\Omega}_{QP_i} \mathbf{\Omega}_{QP_i}^{\dagger}$ are both complex Wishart distributed [61, 95]. The similar statistical properties of the complex CP and QP data allow us to design a unified classification method.

4.4 Proposed Method

4.4.1 Overview

The proposed land cover classification method mainly consists of two components. First, using the multilook complex QP/CP data, the PolarIRGS/CP-IRGS algorithm generates the superpixels on the scene. In this manner, the local spatial correlation among pixels as well as the strong edges in the image are preserved. Second, a fully-connected undirected graph is constructed on the superpixels. Each vertex in the graph corresponds to a superpixel for which three different features are derived: the mean MLC complex matrix (calculated using the superpixel's pixels), the weighted superpixel-based mean MLC matrix (calculated using the mean MLC matrices of a superpixel and its neighboring superpixels), and the superpixel spatial centroid. The affinity matrix, where each element represents the similarity between the corresponding superpixels, is then constructed using these three features. The affinity matrix comprises the global correlation information between all pairs of superpixels across the MLC data.

A few pixels that are spatially distributed all over the image were manually labeled and, then, the superpixels containing the labeled pixels were assigned the same label. The spa-

tial distribution of the labeled superpixels is important since the semi-supervised method propagates labels from labeled to unlabeled superpixels. Using the labeled superpixels and the affinity matrix, the graph-based method estimates the labels of all superpixels—including the labeled and unlabeled ones—generating the land cover classification map of the SAR scene. The block diagram of the proposed land cover classification method is shown in Fig. 4.1. The PolarIRGS and CP-IRGS superpixel generation algorithms are described next. Then, the details of the calculation of the graph affinity matrix and the graph-based approach is explained.

4.4.2   Superpixel generation using PolarIRGS and CP-IRGS

To generate homogeneous superpixels, where each superpixel contains only one land cover type, while preserving the edges in the scene, we apply PolarIRGS and CP-IRGS segmentation algorithms. PolarIRGS and CP-IRGS, as the extensions of IRGS algorithm for QP and CP SAR data, were inherently developed for the application of unsupervised image segmentation [21, 95]. In the historic names of IRGS algorithms [20, 21, 95], "region" is used to describe a group of pixels. Equivalently, "superpixel" is used here due to its current usage in the literature. There are three reasons for applying PolarIRGS and CP-IRGS algorithms to generate superpixel segmentation: first, the IRGS algorithm starts with a highly-oversegmented image and iteratively merges superpixels to obtain the final segmentation. The parameters in the IRGS algorithms allows for choosing the level of oversegmentation—in terms of the size of superpixels—that is suitable for the proposed superpixel-based classification method. Second, the PolarIRGS and CP-IRGS were particularly designed based on the statistical properties of MLC QP and CP data, and, third, these algorithms incorporate the concept of edge strength to preserve the edges in SAR images. This is particularly important in superpixel segmentation where each superpixel is assumed to be homogeneous.

Here, a short description of the PolarIRGS and CP-IRGS segmentation methods is provided. Assuming $\mathcal{S}$ is the image and $s \in \mathcal{S}$ be an image pixel. Also, let $\mathbf{x} = \{x_s | s \in \mathcal{S}\}$ represent the image data and $\mathbf{y} = \{y_s | y_s \in \mathcal{M}, s \in \mathcal{S}\}$ is a label configuration on the image with discrete-valued random variables y_s having a value from the label set $\mathcal{M} = \{1, ..., m\}$. The purpose of an image segmentation is to find the optimum label configuration y^* from the set of possible label configurations $\mathbf{Y}$. IRGS is superpixel-based, and uses a region adjacency graph (RAG) [19], $\mathcal{G} = (\mathcal{V}, \mathcal{E})$, where $\mathcal{V}$ and $\mathcal{E}$ denote the image superpixels as vertices and arcs that are the boundaries of adjacent superpixels. Thus, a superpixel $v \in \mathcal{V}$ in the image contains a set of image pixels denoted by $\mathcal{S}_v$. The optimization problem in

PolarIRGS and CP-IRGS is solved by minimizing two energy terms [20, 21, 95]

$$\mathbf{y}^* = \arg\min_{\mathbf{y} \in \mathbf{Y}} \{ -\sum_{i=1}^{m} \sum_{\mathcal{S}_v \in v_i} \sum_{s \in \mathcal{S}_v} \{ \ln|\mathbf{C}_i| + \mathrm{tr}\left(\mathbf{C}_i^{-1}\mathbf{C}_s\right) \}$$
$$+ \beta \sum_{i=1}^{m-1} \sum_{j=i+1}^{m} \sum_{s \in \partial v_i \cap \partial v_j} g(\nabla_s) \} \tag{4.4}$$

where $\mathbf{C}_s$ is the MLC QP or CP matrix of the pixel s, $\mathbf{C}_i$ is the mean MLC matrix over all the pixels that are labeled i from the set $\mathcal{M}$, $g(\nabla_s)$ is called the edge penalty term [20], v_i is a subset of all superpixels with label i, and ∂v_i indicates all the boundary pixels between superpixels labeled i with other superpixels. Thus, $\partial v_i \cap \partial v_j$ denotes all the boundary pixels between classes i and j.

The edge penalty function $g(\nabla_s)$ is a monotonically decreasing function that is smaller for a strong edge than when the edge between two superpixels assigned to different classes is weak. In this manner, two neighboring superpixels are assigned same labels in segmentation only when the edge between two superpixels is weak [20]. The parameter β controls the smoothness of the segmentation with the greater values of β leading to smoother segmentation results. This parameter, in particular, allows us to control the level of over-segmentation of superpixels.

A main advantage of the IRGS algorithm is incorporating a greedy superpixel merging method in each iteration of the optimization. This increases the algorithm speed in moving toward the optimized segmentation. Starting from an oversegmentation, a superpixel merging process is executed in each iteration. For each pair of neighboring superpixels with like labels, Eq. (4.4) is calculated. Adjacent superpixels with like labels that reduce the energy the most are merged [20].

4.4.3 Semi-supervised graph-based method

The output of the PolarIRGS and CP-IRGS segmentation is a label configuration with labels from the set $\mathcal{M}$. To use this segmentation, we assign a unique label to each superpixel in the segmentation map. In this manner, each superpixel in the segmentation is assigned a unique label. Then, an undirected graph is constructed with each superpixel as a vertex in the graph. The graph is shown by the affinity matrix $\mathbf{A} \in \mathbb{R}^{N \times N}$ (also called weight/similarity matrix) that is $N \times N$ where N is the number of vertices/superpixels and each element in the matrix indicates the similarity between a pair of superpixels in

the graph. The affinity matrix in the proposed method is defined as

$$A_{ij} = A_{ij}^l A_{ij}^c \tag{4.5}$$

where A_{ij}^l is related to the similarity of the superpixels i and j in terms of their location in the image

$$A_{ij}^l = \exp\left(\frac{-\|\vec{\mathcal{L}}_i - \vec{\mathcal{L}}_j\|_2^2}{\sigma_l^2}\right) \tag{4.6}$$

where $\vec{\mathcal{L}}_i$ is a vector of two scalars corresponding to the mean x and y coordinates for all the pixels in the ith superpixel. Also, $\|\cdot\|$ represents the l_2-norm distance, and σ_l is the width of Gaussian kernel. A_{ij}^c is the term corresponding to the similarity of superpixels based on the mean, $\mathbf{C}^m$ and the weighted superpixel-based mean, $\mathbf{C}^w$, MLC matrices [97]

$$A_{ij}^c = \exp\left(\frac{(\gamma - 1)D_{\text{MH}}(\mathbf{C}_i^w, \mathbf{C}_j^w) - \gamma D_{\text{MH}}(\mathbf{C}_i^m, \mathbf{C}_j^m)}{\sigma_c^2}\right) \tag{4.7}$$

where $\mathbf{C}_i^m$ is the mean MLC matrix over all the pixels in the superpixel i and $\mathbf{C}_i^w$ is defined as

$$\mathbf{C}_i^w = \sum_{k=1}^K w_k \mathbf{C}_k^m \tag{4.8}$$

which calculates a weighted average of the K neighboring superpixels of the superpixel i. The weight from the kth superpixel is defined as

$$w_k = \frac{\exp\left(-D_{\text{MH}}(\mathbf{C}_i^w, \mathbf{C}_k^w)/h\right)}{\sum_{k=1}^K \exp\left(-D_{\text{MH}}(\mathbf{C}_i^w, \mathbf{C}_k^w)/h\right)} \tag{4.9}$$

where h is a scale parameter. γ is a scale parameter that balances the effect from the mean MLC matrices as against to the weighted superpixel-based mean MLC matrices. σ_c indicates the width of the Gaussian kernel. $D_{\text{MH}}(\mathbf{C}_1, \mathbf{C}_2)$ represents the statistical dissimilarity between the MLC matrices $\mathbf{C}_1$ and $\mathbf{C}_2$ calculated by the maximum value of Hotelling-Laweley traces (HLTs) [81]

$$D_{\text{MH}}(\mathbf{C}_1, \mathbf{C}_2) = \max\{\text{tr}(\mathbf{C}_1^{-1}\mathbf{C}_2), \text{tr}(\mathbf{C}_2^{-1}\mathbf{C}_1)\}. \tag{4.10}$$

This metric has been demonstrated to be more effective in the application of change detection—similar to the problem here, the difference between two MLC matrices should be measured in change detection—as compared to the likelihood ratio test [81] and other sim-

(a) Google Earth images   (b) RH images

Figure 4.2: The Google Earth and RH images of the RCM CP data set. The magnified areas indicate the two subscenes used in the experiments. Subscene 1 and Subscene 2 are respectively the upper and lower images in the first and last columns.

ilar metrics such as symmetric Wishart distance and Kullback-Leibler divergence [82]. A complete affinity matrix, that is equivalent to a fully-connected graph, models the global spatial correlation effect between all pairs of superpixels in the image. Then, a semi-supervised classification method based on label propagation [99] is performed. First, the superpixels containing labeled pixels are assigned labels. Then, from a conceptual perspective, the semi-supervised method propagates the labels from the labeled superpixels to the unlabeled ones.

Assume $\mathbf{Z} \in \mathbb{R}^{N \times T}$ is the initial label information, where T is the number of land cover types. Each row of the matrix $\mathbf{Z}$ corresponds to a superpixel: if the superpixel i is labeled j, the element $\mathbf{Z}_{ij} = 1$, otherwise, for all j, $\mathbf{Z}_{ij} = 0$. For all the unlabeled superpixels, $\mathbf{Z}_{ij} = 0$ for all j. The label propagation is performed based on the assumption that the classification matrix $\mathbf{F} \in \mathbb{R}^{N \times T}$ in each iteration is a function of the spatial correlation information between superpixels and the initial label information [99]

$$\mathbf{F}(i+1) = \alpha \mathbf{B}^{-1/2} \mathbf{A} \mathbf{B}^{-1/2} \mathbf{F}(i) + (1-\alpha)\mathbf{Z} \tag{4.11}$$

where $\mathbf{F}(i)$ indicates the classification matrix in iteration i, $\mathbf{B} \in \mathbb{R}^{N \times N}$ is a diagonal matrix with its ii-element equal to the sum of the i_{th} row of $\mathbf{A}$, and the parameter α balances the relative effect from the global spatial correlation information and the initial labeling information. The classification matrix $\mathbf{F}$ converges to a closed-form solution $\mathbf{F}^*$

as follows [99]

$$\mathbf{F}^* = \frac{\mu}{\mu+1}(\mathbf{I} - \frac{1}{\mu+1}\mathbf{B}^{-1/2}\mathbf{A}\mathbf{B}^{-1/2})^{-1}\mathbf{Z} \tag{4.12}$$

where I is the $N \times N$ identity matrix and μ is a weight parameter, where $\alpha = \frac{1}{\mu+1}$. The final land cover labels of the superpixels are then calculated as $z_i = \arg\max_j \mathbf{F}_{ij}$.

4.5   Experimental Results

In this section, the RCM SLC data sets used in the experiments are described. The pre-processing of the data sets is then explained followed by the experimental setup to evaluate the proposed method and analyze the effects of local as well as global spatial correlation in the land cover classification method.

4.5.1   RCM data sets

Two RCM SLC data sets were used in the experiments. The first data set is a very high-resolution SLC CP data set that was acquired over the Winnipeg city in Manitoba, Canada, on February 2, 2020. The sampled pixel and line spacing for the data set are 1.39m and 2.16m, respectively. The CP scene has a size of 14066×9734 pixels. The second data set is an SLC full QP data acquired over the Québec City in Québec, Canada, on December 29, 2019. The sampled pixel and line spacing for the SLC QP data set are 3.13m and 3.31m, respectively. The size of the QP scene is 8007×2935.

To evaluate the performance of the proposed method, two subscenes were acquired from each SLC scene. Fig. 4.2 and Fig. 4.3 show the Google Earth and intensity images of the CP and QP scenes, respectively. Each of the subscenes from the CP scene, indicated in Fig. 4.2, consists of four land cover types that are visually identified. The size of Subscene 1 of CP data is 1622×1272 pixels and includes low-rise residential (LRR), high-rise residential (HRR), vegetation (VEG), and asphalt (ASP) land cover classes. Subscene 2 of CP data has a size of 1000×1200 with the same first three land cover types as those in Subscene 1: LRR, HRR, VEG, and another class as train (TRA).

The two subscenes taken from the QP scene, shown in Fig. 4.3, have 700×500 pixels, for Subscene 1, and 500×700 pixels, for Subscene 2. Subscene 1 from the QP scene consists of six classes: river (RIV), LRR, HRR, VEG1, VEG2, and shore (SHR). VEG1 and VEG2 correspond to the two types of vegetation that have different SAR backscatter values. Subscene 2 includes all the classes in Subscene 1 except the class HRR. Next,

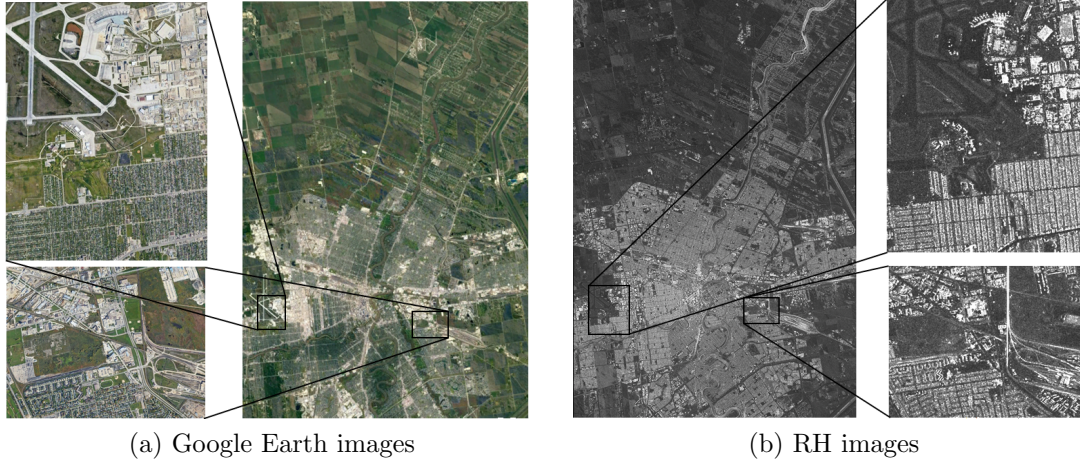(a) Google Earth images   (b) HH images
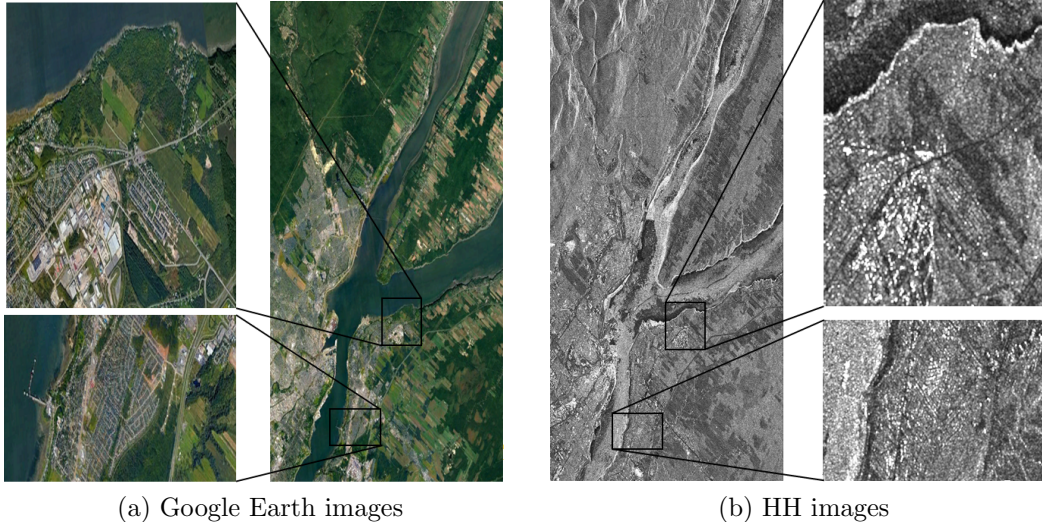
Figure 4.3: The Google Earth and HH images of the RCM QP data set. The magnified areas indicate the two subscenes used in the experiments. Subscene 1 and Subscene 2 are respectively the upper and lower images in the first and last columns.

the experimental setup including the pre-processing of the SLC data sets, the parameter setting of the proposed method, and the compared methods are described.

4.5.2   Experimental setup

The RCM SLC CP data set contains two files that represent the complex elements E_H and E_V in Eq. (4.1). Also, the SLC QP data set includes three files corresponding to the complex elements of the scattering matrix in Eq. (4.1). The MLC CP coherence ($\mathbf{C}_{CP}$) and the MLC QP covariance ($\mathbf{C}_{QP}$) were respectively derived based on Eq. (4.2) and Eq. (4.3) with the number of looks, $L = 1$. Box-car averaging with a window size of 5×5 was then performed only on the MLC CP data. Averaging was found unnecessary for the MLC QP data for both segmentation and classification—since the pixel and line spacing for the QP scene are larger than those for the CP scene, to fully-preserve the boundaries in segmentation and classification the averaging was not performed in the case of QP data.

To generate superpixels, CP-IRGS and PolarIRGS were performed with 10 segmentation classes. After the segmentation, each superpixel in the segmentation image, regardless of its segmentation class, is given a unique label. Then, the graph is constructed on the

81

Table 4.1: The number of train and test pixels for the two Subscenes of CP SAR data.

Subscene #	Class name	Description	# of train	# of test
Subscene 1	LRR	Low-rise residential	49	227
	HRR	High-rise residential	32	58
	VEG	Vegetation	42	169
	ASP	Asphalt	32	61
Subscene 2	LRR	Low-rise residential	36	191
	HRR	High-rise residential	37	84
	VEG	Vegetation	50	90
	TRA	Train	40	83

superpixels. We need to set the parameters of the proposed semi-supervised graph-based method including h (4.9), σ_l (4.6), σ_c (4.7), γ (4.7), and μ (4.12). The parameter h was set to 10. The parameters σ_l and σ_c were set to 1000 and 1, respectively. The parameter γ was set to 0.9 allowing for more impact from $\mathbf{C}_i^m$ (the superpixel itself) than that of $\mathbf{C}_i^w$ (the neighboring superpixels). Finally, the parameter μ was also set to 0.1. All these values were kept the same for all experiments.

The parameter values were found using an empirical testing in a course-to-fine search method. The two components of the affinity matrix elements in Eq. (4.5), naming A_{ij}^l and A_{ij}^c, should have comparable values so that the effect from both spatial and backscatter differences between superpixel pairs is balanced. The parameters σ_l and σ_c have a huge impact on the values of affinity matrix elements. To incorporate effect from both spatial and backscatter information, the width of the spatial Gaussian kernel σ_l are set to a large value to balance the large values of l_2-norm distance between superpixels very apart from each other across the scene. Also, as shown in previous work [97], with a complex land cover structure, information from neighboring superpixels (here modeled by the weighted MLC matrix, C_i^w) should be limited by choosing a high value for the parameter γ to incorporate more information from within each superpixel (here modeled by the mean MLC matrix, C_i^m). In general, the classification results were not considerably sensitive to the values of the parameters γ, h and μ.

To evaluate the performance of the land cover classification method, the user's accuracy values of the classes, the overall accuracy (OA), and the Kappa (κ) coefficient were used. For comparison, these values were also calculated for four other methods: support

Table 4.2: The number of train and test pixels for the two Subscenes of QP SAR data.

Subscene #	Class name	Description	# of train	# of test
Subscene 1	RIV	River	50	66
	LRR	Low-rise residential	40	97
	HRR	High-rise residential	51	56
	VEG1	Vegetation 1	51	166
	VEG2	Vegetation 2	44	180
	SHR	Shore	35	36
Subscene 2	RIV	River	50	57
	LRR	Low-rise residential	54	127
	VEG1	Vegetation 1	46	110
	VEG2	Vegetation 2	39	80
	SHR	Shore	15	31

vector machine (SVM) [29], random forest (RF) [135], superpixel-based SVM (SSVM), and superpixel-based RF (SRF). The latter two methods, SSVM and SRF, exploit the superpixels for the classification. In particular, the mean value of the feature vectors for all pixels in each superpixel was calculated and used for estimating the label of the superpixel. The input to the proposed method is the MLC data which was used to extract several features as the input to the compared methods including SVM, RF, SSVM, and SRF. In the case of CP data, all the Stokes-derived features, and in the case of QP data, the features extracted from the QP covariance matrix ($\mathbf{C}_{QP}$) including the original SAR features (full QP coherency matrix elements), SAR discriminators (SPAN and correlation coefficients), and various decomposition parameters were used in the experiments [23].

For each class, around 50 training pixels and a minimum of 30 test pixels (usually much higher number) that were independently collected were used for all the classification methods. The number of train and test samples for each land cover type in the QP and CP SAR subscenes is provided in Table 4.1 and Table 4.2. For the four compared methods, a hyperparameter tuning step was performed separately for each experiment. The values of hyperparameters c and γ in SVM and the hyperparameters n_e (number of estimators) and m_d (maximum depth) in RF were calculated using a grid search strategy. In each experiment where the methods RF, SVM, SRF, and SSVM were performed, a grid

(a) RH	(b) Segmentation	(c) Proposed method	(d) SRF	(e) SSVM

■ Low-rise residential ■ High-rise residential ■ Vegetation ■ Asphalt

(f) RH	(g) Segmentation	(h) Proposed method	(i) SRF	(j) SSVM

■ Low-rise residential ■ High-rise residential ■ Vegetation ■ Asphalt

Figure 4.4: Classification results on the CP data set. (a) and (f) The RH intensity for Subscene 1 and the zoomed-in area, (b) superpixel segmentation with labeled train superpixels using train pixels and (g) superpixel segmentation of the zoomed-in area overlaid on RH image, as well as the classification images of the (c) and (h) proposed method, (d) and (i) superpixel-based RF, and (e) and (j) superpixel-based SVM for Subscene 1 of the CP data.

search in $c \in [2^{-6}, 2^{14}]$ and $\gamma \in [2^{-9}, 2^{11}]$ (increment factor of one for the power of two) or $n_e \in [50, 2000]$ (increment factor of 50) and $m_d \in [1, 110]$ (increment factor of 2) was executed to select the hyperparameter values that provide the highest κ when half of the training pixels were used for training and the remaining half for testing.

4.5.3 Results of MLC CP data

The RH image, superpixel segmentation with the labeled superpixels and the classification images of the proposed method along with the SRF and SSVM are presented in Fig. 4.4

| (k) RH | (l) Segmentation | (m) Proposed method | (n) SRF | (o) SSVM |

■ Low-rise residential ■ High-rise residential ■ Vegetation ■ Train

| (p) RH | (q) Segmentation | (r) Proposed method | (s) SRF | (t) SSVM |

■ Low-rise residential ■ High-rise residential ■ Vegetation ■ Train
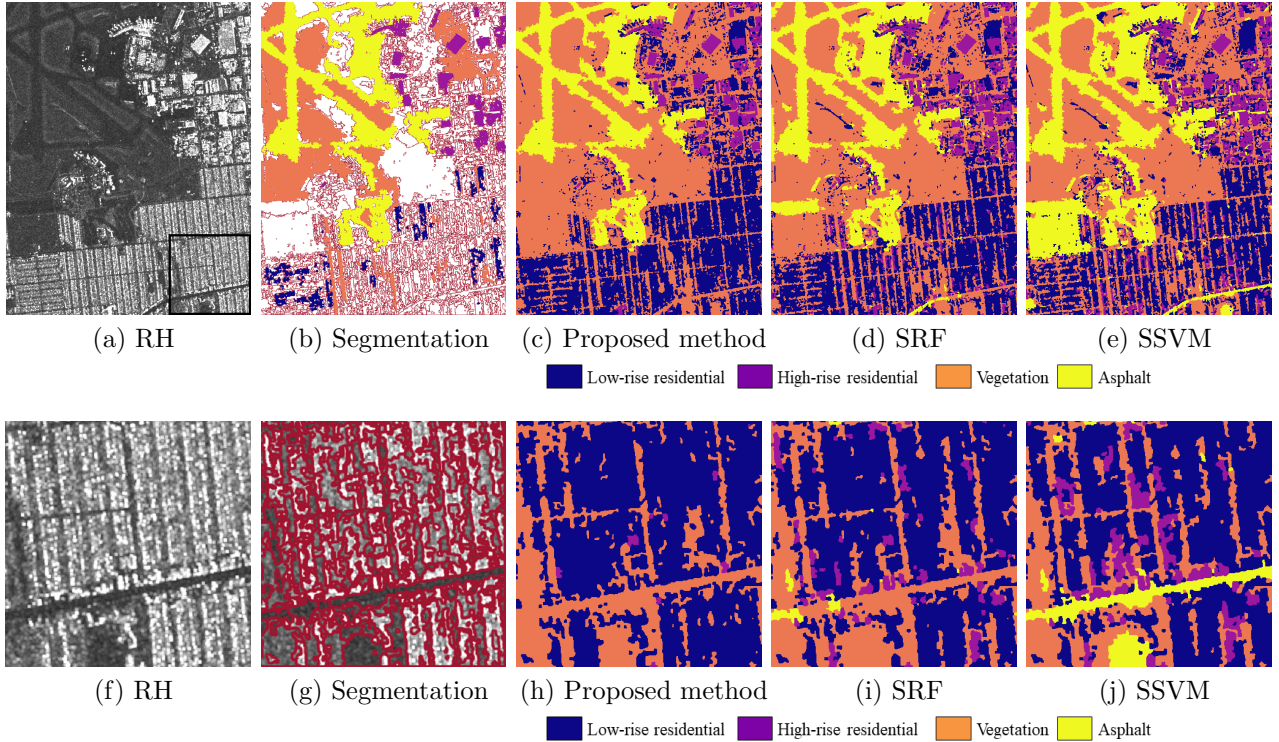
Figure 4.4: Classification results on the CP data set. (k) and (p) The RH intensity for Subscene 2 and the zoomed-in area, (l) superpixel segmentation with labeled train super-pixels using train pixels and (q) superpixel segmentation of the zoomed-in area overlaid on RH image, as well as the classification images of the (m) and (r) proposed method, (n) and (s) superpixel-based RF, and (o) and (t) superpixel-based SVM for Subscene 2 of the CP data.

Table 4.3: Classification performance of the five compared methods in terms of class accuracy values, the overall accuracy and the κ coefficient on the Subscene 1 of the CP SAR data

Measure	Class	**Proposed Method**	SRF	SSVM	RF	SVM
User's Accuracy (%)	LRR	**94.47**	69.59	67.28	40.55	37.79
	HRR	80.95	**96.83**	**96.83**	77.78	85.71
	VEG	**93.87**	93.25	85.28	47.24	40.49
	ASP	84.72	**95.83**	**95.83**	75.00	87.50
Overall Accuracy (%)		**91.26**	84.08	80.58	52.04	51.46
Kappa Coefficient		**0.87**	0.78	0.73	0.34	0.38

85

(a) HH   (b) Segmentation   (c) Proposed method   (d) SRF   (e) SSVM

River   Low-rise residential   High-rise residential   Vegetation 1   Vegetation 2   Shore

(f) HH   (g) Segmentation   (h) Proposed method   (i) SRF   (j) SSVM

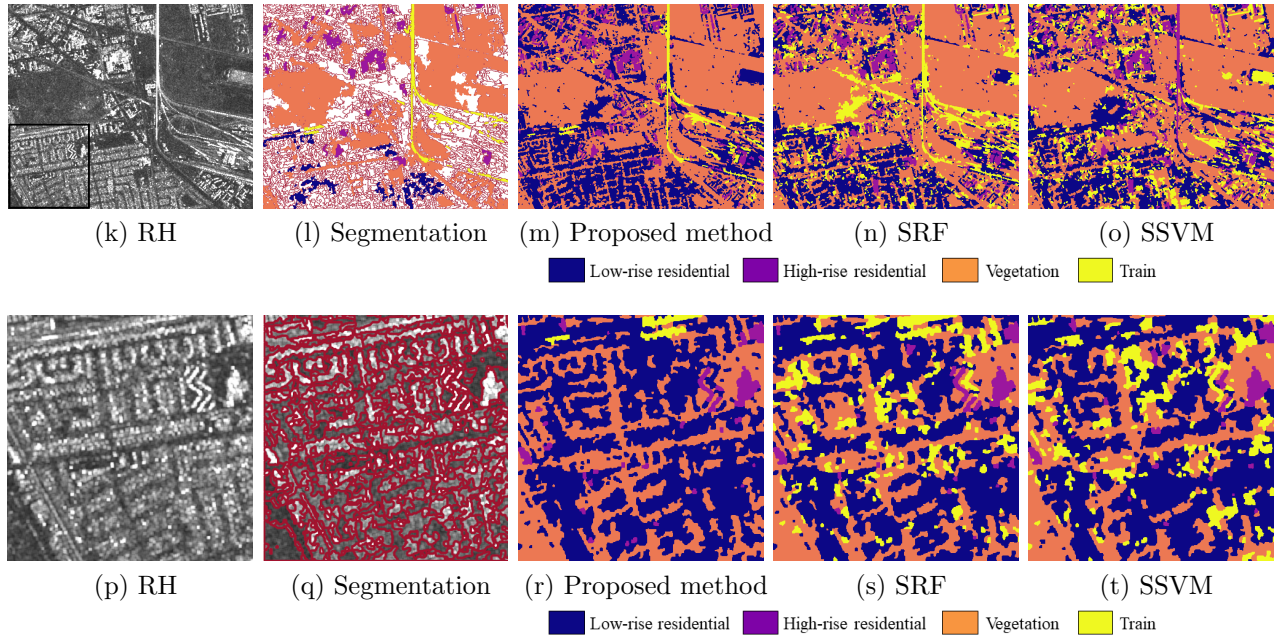River   Low-rise residential   High-rise residential   Vegetation 1   Vegetation 2   Shore

Figure 4.5: Classification results on the QP data set. (a) and (f) The HH intensity for Subscene 1 and the zoomed-in area, (b) superpixel segmentation with labeled train superpixels using train pixels and (g) superpixel segmentation of the zoomed-in area overlaid on HH image, as well as the classification images of (c) and (h) proposed method, (d) and (i) superpixel-based RF, and (e) and (j) superpixel-based SVM for Subscene 1 of the QP data.

(a) - (e). The quantitative results for the CP subscenes are shown in Table 4.3 and Table 4.4. As seen in the first subscene (the first row in Fig. 4.4), the land cover types have distinguishable radar backscatter. In this case, the classification images are similar. Although the SRF and SSVM methods provide higher class accuracy values for HRR and ASP classes, the proposed method provides better class accuracy values for LRR and VEG classes and higher OA and κ values than the compared methods, as demonstrated in Table 4.3. The pixel-based RF and SVM classifiers, which do not exploit the local spatial correlation effect of superpixels, perform poorly in land cover classification.
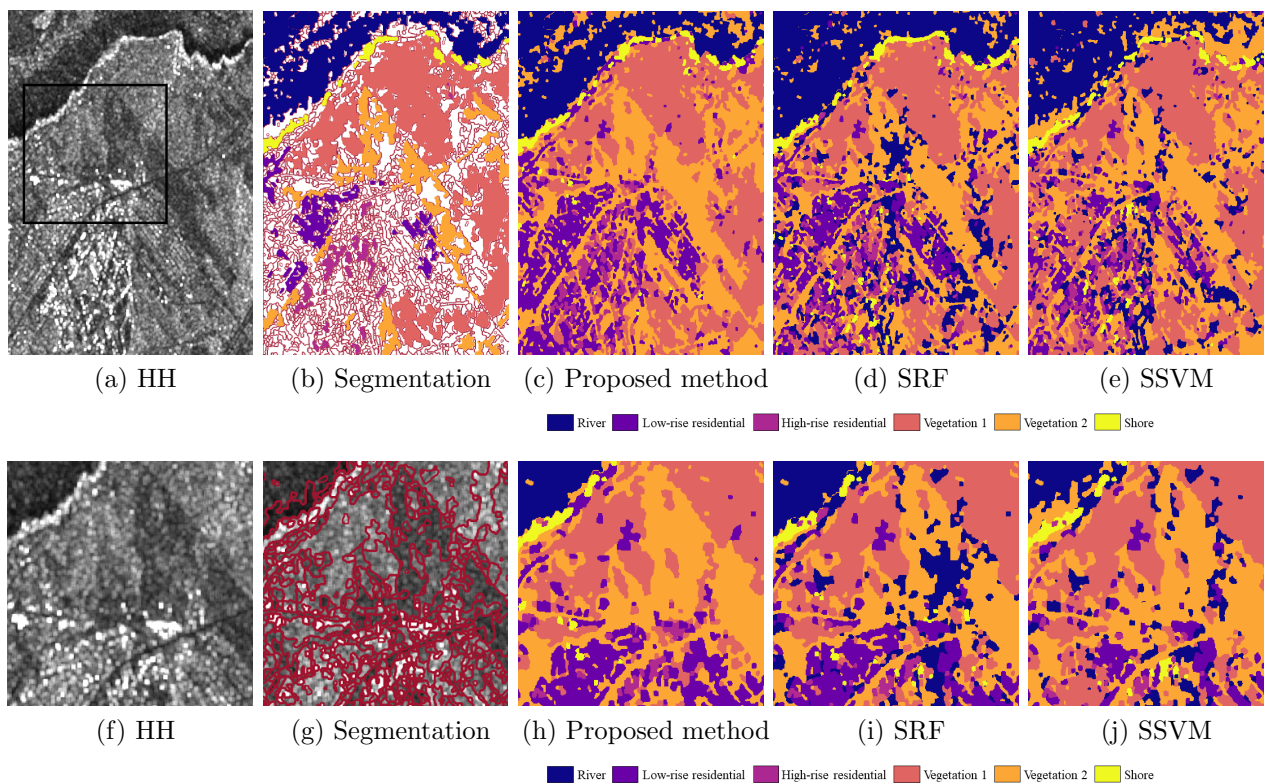
86
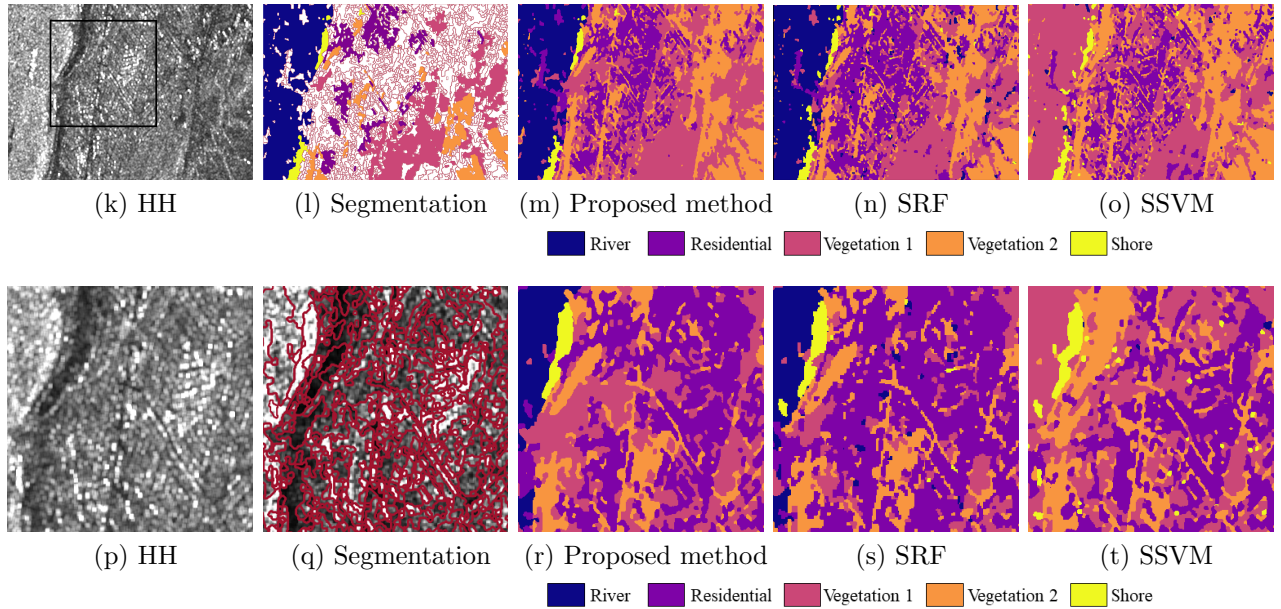
Figure 4.5: Classification results on the QP data set. (k) and (p) The HH intensity for Subscene 2 and the zoomed-in area, (l) superpixel segmentation with labeled train superpixels using train pixels and (q) superpixel segmentation of the zoomed-in area overlaid on HH image, as well as the classification images of (m) and (r) proposed method, (n) and (s) superpixel-based RF, and (o) and (t) superpixel-based SVM for Subscene 2 of the QP data.

Table 4.4: Classification performance of the five compared methods in terms of class accuracy values, the overall accuracy and the κ coefficient on the Subscene 2 of the CP SAR data

Measure	Class	**Proposed Method**	SRF	SSVM	RF	SVM
	LRR	**91.46**	69.35	67.84	00.50	52.76
User's Accuracy (%)	HRR	**87.18**	84.62	85.90	0.00	65.39
	VEG	97.62	**98.81**	**98.81**	**98.81**	96.43
	TRA	83.91	91.95	20.69	**99.99**	47.13
Overall Accuracy (%)		**90.40**	81.92	67.63	38.17	62.05
Kappa Coefficient		**0.86**	0.75	0.56	0.23	0.49

Table 4.5: Classification performance of the five compared methods in terms of class accuracy values, the overall accuracy and the κ coefficient on the Subscene 1 of the QP SAR data

Measure	Class	**Proposed Method**	SRF	SSVM	RF	SVM
	RIV	81.48	**88.89**	74.07	54.32	18.52
	LRR	**89.61**	74.03	49.35	40.26	40.26
	HRR	**86.89**	70.49	67.21	32.79	34.42
User's Accuracy (%)	VEG1	**79.21**	63.37	**79.21**	71.29	72.77
	VEG2	**97.89**	80.99	92.25	75.35	92.25
	SHR	**89.47**	86.84	**89.47**	78.95	84.21
Overall Accuracy (%)		**86.69**	74.54	77.20	62.56	62.73
Kappa Coefficient		**0.83**	0.68	0.71	0.52	0.52

The results of a zoomed-in area at the bottom-right of Subscene 1 were also provided in Fig. 4.4 (f) - (j). The classification images indicate that the proposed method keeps the consistency of the areas of the scene, which can lead to either accurate classification (some LRR areas being mislabeled by SRF and SSVM as HRR) or incorrect classification (ASP being mislabeled as VEG by the proposed method). Experiments showed that to obtain accurate classification results using the proposed method and avoid these misclassifications, the labeled superpixels should be selected from different parts of the scene. In other words, the proposed method needs only few labeled superpixels in each part of the scene, where there is a land cover type, to perform accurately.

In Subscene 2, the class TRA has a similar radar backscatter to that of HRR and LRR classes as seen in Fig. 4.4 (k). The proposed method incorporates the global spatial information among superpixels, and prevents the misclassifications of LRR and HRR classes to TRA class which happen in the case of SRF and SSVM methods (see Fig. 4.4 (n) - (o)). Most of TRA pixels are misclassified by SSVM method leading to a relatively lower OA compared to that of SRF mehtod. The OA and κ values of the proposed method in this case are noticeably higher than the compared methods as seen in Table 4.4. The pixel-based RF, in this case, assigns all the pixels to only VEG and TRA classes failing to correctly classify this subscene. The zoomed-in area at the bottom-left part of the subscene highlights the misclassified residential areas to TRA.

Table 4.6: Classification performance of the five compared methods in terms of class accuracy values, the overall accuracy and the κ coefficient on the Subscene 2 of the QP SAR data

Measure	Class	**Proposed Method**	SRF	SSVM	RF	SVM
User's Accuracy (%)	RIV	92.86	**96.43**	0.00	75.00	66.07
	LRR	78.81	**86.75**	70.86	52.32	47.02
	VEG1	**93.18**	76.14	78.41	9.09	0.00
	VEG2	97.10	95.65	**98.56**	94.20	98.55
	SHR	75.67	75.61	**80.49**	4.87	0.00
Overall Accuracy (%)		**86.67**	86.00	68.40	48.40	43.46
Kappa Coefficient		**0.83**	0.82	0.58	0.33	0.28

4.5.4 Results of MLC QP data

In Fig. 4.5, the results for the two QP subscenes were shown. As seen in the HH images of the two subscenes (Fig. 4.5 (a) and (k)), due to the similar backscatter values for the classes, the classification task is more challenging in this case than the CP data set. Also, as mentioned in the data set description in Section 4.5.1, the QP data set has a coarser resolution than that of the CP data. This is the reason for lower accuracy values in the case of QP data set. In subscene 1 of the QP data, shown in Fig. 4.5 (a) - (j), the proposed method performed much better than the methods SRF and SSVM, where there are many misclassified areas (misclassification of vegetation to river across the scene in the case of SRF method, Fig. 4.5 (d) and more highlighted in the center of the zoomed-in area in Fig. 4.5 (i), and misclassification of residential areas to vegetation types in the case of SSVM method, Fig. 4.5 (e) and the bottom-left of the zoomed-in area in Fig. 4.5 (j)). The accuracy values in Table 4.5 supports the latter conclusion.

In the second QP subscene, the SRF method provides classification results as accurate as the proposed method. Although SRF method performs better for HRR and ASP than the proposed method, SRF provides a much lower accuracy value for LRR, and given a higher number of test samples for LRR class as seen in Table 4.2, a higher overall accuracy is obtained for the proposed method. The other three methods including the SSVM, RF, and SVM were unable to perform the classification accurately where each of these methods misclassifies a whole class (see the user's accuracy values in Table 4.6). For instance, the RIV ares are misclassified as VEG1 using SSVM method as seen in Fig. 4.5 (o) - (t). Next, the analyses of the variation of OA values as functions of the number of training pixels and the number of superpixels are provided.

4.5.5   Effects of number of training pixels and N

To assess the performance of the proposed method as compared to the other methods with small numbers of training pixels, the classification OA values were calculated with choosing the number of training pixels from the set $\{2, 5, 10, 20, 30, 40, 50\}$, and plotted, as presented in Fig. 4.6. As expected, in general, the OA values of all the methods increase with more number of training pixels. The proposed method in all data sets provides consistently higher classification rates compared to the other methods. Also, the accuracy values of the RF method are mostly higher than those of the SVM method comparing either pixel-based or superpixel-based versions of these two classifiers. In all cases, with only five training pixels per class, the proposed method provides an accuracy of $\sim 80\%$ where the other methods typically need more training pixels to obtain an accuracy as high as 80%.

Finally, the sensitivity of OA as a function of the number of superpixels was shown in Fig. 4.7. By setting a large value of β in Eq. (4.4), the PolarIRGS and CP-IRGS segmentation methods provide smoother segmentation images with fewer superpixels. The β values were reduced gradually allowing for more superpixels in the segmentation image. For all cases, after an increase in OA accuracy, the values of OA remain relatively steady. This indicates that it is unnecessary to construct a graph using a highly oversegmented image as with a lower number of superpixels the algorithm executes much more quickly. Using the spatial resolution and size of the scenes, as well as the numbers of superpixels, the average ground area per superpixel can be calculated. For the number of superpixels associated with the highest OA accuracy value for each subscene from Fig. 4.7, the average ground area per superpixel were approximately 3191m^2 and 3486m^2 for the CP and QP subcenes, respectively. The constant C_1 from Eq. (3.18) in Section 3.5.2 was used to control the value of β. In these experiments, $C_1 = 2$ and $C_1 = 1.25$ for CP and QP subscenes, respectively. A proper value of C_1 should be selected based on the homogeneity and pixel spacing of the scene.

4.6   Summary

In this chapter, the problem of land cover classification using RCM complex CP and QP data types was addressed. Using superpixels is favorable in image classification since it reduces the number of image primitives as compared to using pixels. The superpixel segmentation methods here were generated using CP-IRGS and PolarIRGS unsupervised segmentation algorithms, which respectively are the extensions of IRGS algorithm to complex CP and QP data. By modeling the local spatial correlation information based on
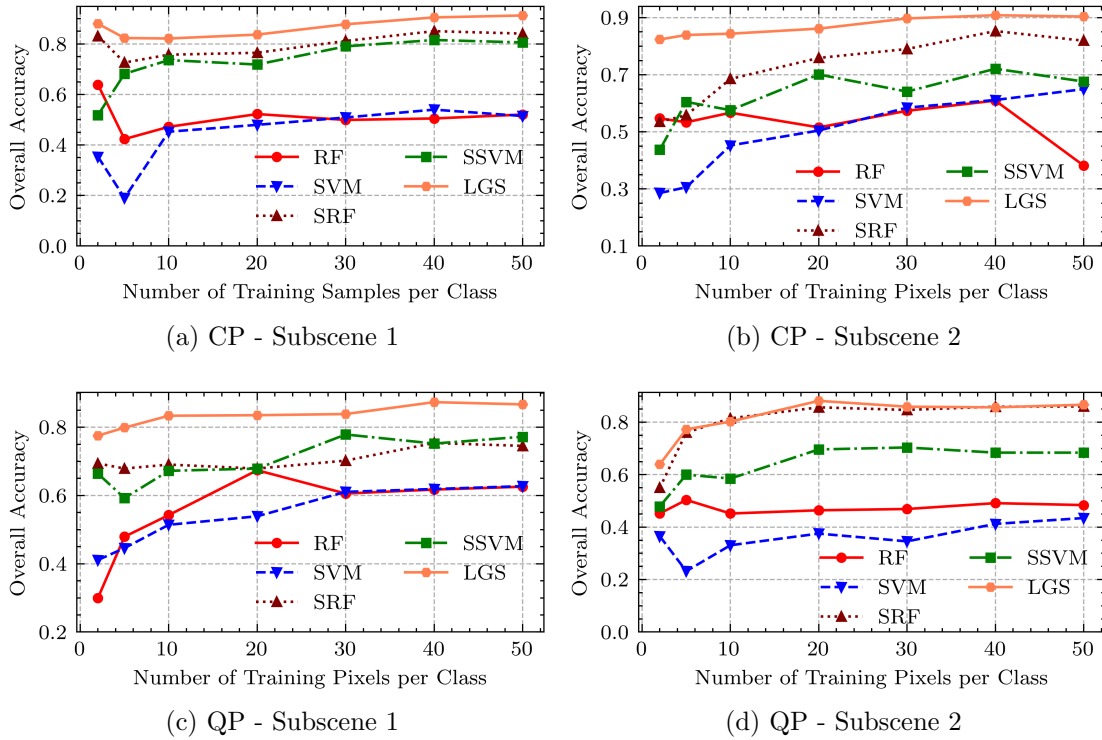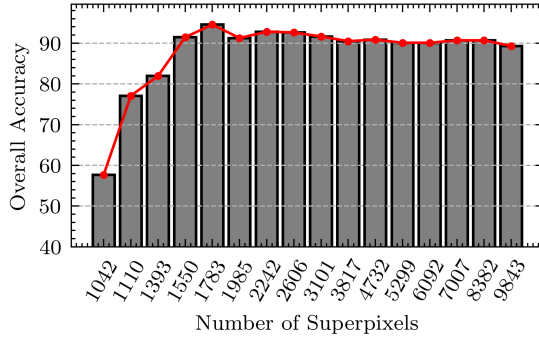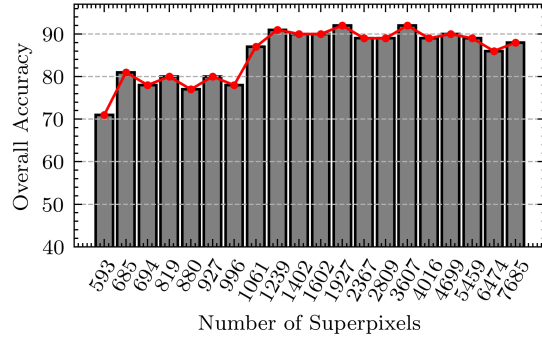
Figure 4.6: Overall accuracy of the five compared methods as functions of number of training pixels per class.

the statistical properties of complex CP and QP data, CP-IRGS and PolarIRGS generate superpixels where the boundaries are preserved without wasting too many superpixels in homogeneous areas. Next, the global spatial information among superpixels are modeled by a graph constructed on superpixels as the vertices of the graph. Then, with only a few superpixels labeled, the labels of unlabeled superpixels were predicted in a semi-supervised manner using a label propagation algorithm.

The classification results on a pair of CP and a pair QP images indicate that the proposed method performs the classification with higher accuracy values than two superpixel-based SVM and RF methods particularly when the number of labeled superpixels are low. The analysis of classification accuracy relative to the number of superpixels in the image indicates that, to a certain level, oversegmentation (higher number of superpixels) results in higher classification accuracy values. After some level of oversegmentation, the accuracy values do not vary significantly. Therefore, there is no need for a highly oversegmented

(a) CP - Subscene 1

(b) CP - Subscene 2
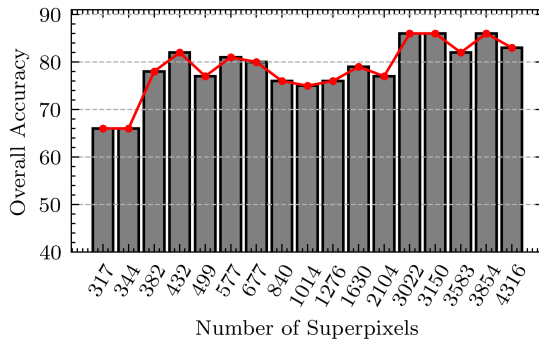
(c) QP - Subscene 1

(d) QP - Subscene 2

Figure 4.7: Overall accuracy of the five compared methods as functions of number of superpixels in the superpixel segmentation image.

image since that increases the execution time of the graph-based classification dramatically.

Chapter 5

Conclusions and Future Work

The overall aim of this thesis was to design classification algorithms for CP SAR data. With CP data becoming accessible from the recent launch of RCM, developing automated CP classification methods is of interest for different application, especially, sea-ice mapping. Throughout 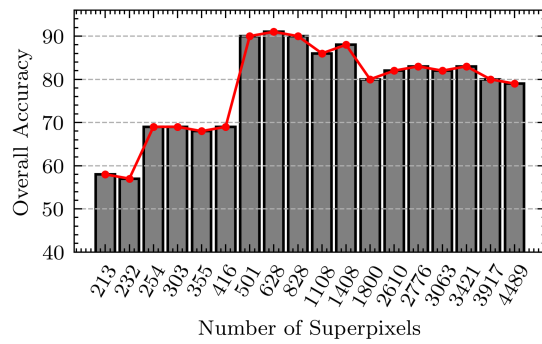this thesis, the effort was to develop algorithms that make use of the whole information in CP data, which is represented in the format of 2×2 complex coherence matrix, or equivalently, the Stokes vector.

Symmetry assumptions allow for reconstructing 3×3 complex QP covariance matrix from the complex CP coherence matrix. First contribution of this thesis is to develop a scene classification method that combines the segmentation results using the reconstructed QP data with an SVM labeling method using a set of derived features from the Stokes vector. Second contribution involves developing a region-based unsupervised segmentation method using complex CP coherence matrix data. Finally, the third main contribution of this thesis is designing a superpixel-based semi-supervised RCM CP classification where the global spatial information among the superpixels in image is modeled by a graph.

Unlike the QP reconstruction and the unsupervised segmentation methods that were evaluated using sea-ice data, the performance of the superpixel-based classification method was evaluated using real RCM scenes from rural areas that were accessible for this thesis. A summary of contributions and experimental results of each chapter of the thesis are provided next.

5.1 Summary of Contributions and Results

Most of the previous work on CP classification exploits either the derived features from Stokes vector or the reconstructed complex QP data from CP in a classification scheme. In Chapter 2, a full-scene ice-type classification approach using CP SAR data was designed where both reconstructed QP data from CP and the features derived from CP Stokes vector are used. First, a full scene segmentation is performed for producing class-homogeneous regions. Depending on the type of SAR data, either IRGS (in the cases of DP or CP intensities only) or PolarIRGS (in the cases of reconstructed QP and full QP) are performed to generate the segmentation images. Using the spatial-context information that is modeled in the unsupervised segmentation regions, we aimed to improve the pixel-based classification results of an SVM model which uses the CP-derived features. In particular, the segmentation is combined with the SVM classification using a majority voting approach to assign an ice-type label to each region of the unsupervised segmentation image.

In the experiments, four ice types were classified on the test scene. The performance of four different reconstruction methods were assessed for various ice types. According to the reconstruction accuracy values, Nord's reconstruction method provides the lowest error values in reconstruction. The classification results were obtained for four different cases were tested: DP, CP (RH and RV only), CP (all features), and QP. The SVM labeling model is trained on one scene and tested on another scene. Using CP with all features generated the overall classification accuracy (96.53%) which is slightly lower than that achieved using the full QP data. A direct comparison between the results of the CP intensities (overall accuracy of 92.86%) case and those of the DP intensities (overall accuracy of 81.04%) indicates the high potential of CP scenes in providing improved sea-ice maps as compared to DP scenes. Also, the comparison of results of pixel-based SVM with the method that combines segmentation and SVM labeling indicates that using an unsupervised segmentation image of the scene, the pixel-based classification accuracy values increases by 15%, where a very low number of training samples (10 samples per class) were needed to obtain an accuracy as high as over 90%.

In Chapter 3, a region-based unsupervised segmentation algorithm using the MLC CP coherence matrix data was proposed. The algorithm was structured based on the well-known IRGS. In the proposed algorithm, CP-IRGS, both unary and pairwise potentials were modeled based on the complex CP data. The experiments were conducted on a simulated CP scene and a pair of RADARASAT-2 QP SLC images. Three different methods were tested: IRGS method using RH and RV intensities, CP-IRGS using VFG method, and CP-IRGS using CR-based method. The results indicate that the CP-IRGS algorithm, which is particularly developed for the MLC CP coherence matrix data, performs the unsu-

pervised segmentation in a more accurate manner than the original IRGS algorithm using RH and RV intensity images especially where the SAR scene consists of multiple classes.

The purpose of Chapter 4 was to exploit the segmentation images, also called superpixels, provided by the unsupervised CP-IRGS algorithm in a classification process. A unified complex CP and QP SAR superpixel-based classification method was proposed. The proposed method incorporates the spatial correlation information in both local and global scales. The local spatial information was obtained by using the superpixels generated by the CP-IRGS and PolarIRGS segmentation methods. The local spatial information from an unsupervised segmentation was also used in Chapter 2 where the classification approach combines segmentation and labeling using majority voting. In Chapter 4, a semi-supervised graph-based learning method models the spatial correlation among the superpixels in a global manner.

Two RCM SLC land cover data sets were used to evaluate the performance of the proposed method. Comparing only the results of the SVM and RF classifiers in pixel-based and superpixel-based methods demonstrates the effect of the local spatial correlation information among pixels where much higher classification accuracy values were obtained using superpixel-based methods than pixel-based ones. The effect of global spatial correlation was shown by comparing the results of the proposed graph-based method against those of the superpixel-based SVM and RF classifiers which do not take advantage of the global-scale spatial information. The results show that, using global spatial correlation, the proposed method prevents the misclassifications that happen in the case of superpixel-based SVM and RF methods. Another important advantage of the proposed method is that, with a very low number of training pixels, the method provides highly-accurate classification images.

5.2 Future Work

This work demonstrated the advantage of using spatial information in local and global scales in CP classification. The local spatial information was modeled using the unsupervised segmentation discussed in Chapter 3. The global spatial information was also modeled using graph models in Chapter 4. Previous work [11] has investigated the use of texture features in sea-ice classification using DP SAR images. A future line of work would incorporate the spatial correlation information in CP classification using either "hand-crafted" texture features such as gray-level coccurrence matrix (GLCM) [103, 104] and Gabor features [105] or a feature representation that is based on deep convolutional neural networks (CNNs) derived from CP-derived features. Developing CNN-based classification methods

that use the complex 2×2 coherence matrix data would be an interesting line of future work.

In Chapter 3, an edge detection method using ratio-based edge detectors was designed. Future work would involve exploring various edge strength map calculation methods and adapting them to MLC CP coherence data. This can improve the performance of unsupervised segmentation to a great extent. CP-IRGS segmentation, as demonstrated in Chapter 3, successfully identifies superpixels in the image by performing an unsupervised segmentation. This is particularly useful when designing superpixel-based classification methods such as the one in Chapter 4. The remaining work will only be to label the homogeneous superpixels identified by CP-IRGS. A valuable future study would investigate various graph convolutional networks for CP classification where a graph is constructed over the superpixels generated by CP-IRGS.

References

[1] D. Flett, Y. Crevier, and R. Girard, "The RADARSAT Constellation Mission: Meeting the government of Canada's needs and requirements," in *Geoscience and Remote Sensing Symposium, 2009 IEEE International, IGARSS 2009*, vol. 2. IEEE, 2009, pp. II–910.

[2] M. Manore, R. DeAbreu, V. Zabeline, M. Arkett, and D. Bradley, "The RADARSAT Constellation Mission (RCM): Extending operational marine surveillance for environment Canada," in *ASTRO Annu. Meet.*, 2010.

[3] R. K. Raney, "Hybrid-polarity SAR architecture," *IEEE Transactions on Geoscience and Remote Sensing*, vol. 45, no. 11, pp. 3397–3404, 2007.

[4] F. Charbonneau, B. Brisco, R. Raney, H. McNairn, C. Liu, P. Vachon, J. Shang, R. DeAbreu, C. Champagne, A. Merzouki *et al.*, "Compact polarimetry overview and applications assessment," *Canadian Journal of Remote Sensing*, vol. 36, no. S2, pp. S298–S315, 2010.

[5] R. Ressel, S. Singha, S. Lehner, A. Rösel, and G. Spreen, "Investigation into different polarimetric features for sea ice classification using X-band synthetic aperture radar," *IEEE Journal of Selected Topics in Applied Earth Observations and Remote Sensing*, vol. 9, no. 7, pp. 3131–3143, 2016.

[6] M. Dabboor, S. Iris, and V. Singhroy, "The RADARSAT constellation mission in support of environmental applications," in *Multidisciplinary Digital Publishing Institute Proceedings*, vol. 2, no. 7, 2018, p. 323.

[7] M. Dabboor and T. Geldsetzer, "Towards sea ice classification using simulated RADARSAT Constellation Mission compact polarimetric SAR imagery," *Remote Sensing of Environment*, vol. 140, pp. 189–195, 2014.

[8] "Interpreting ice charts," *Canadian Ice Service publications, ice forecasts and observations, Environment and Natural Resources, Government of Canada* *https://www.canada.ca/en/environment-climate-change/services/ice-forecasts-observations/publications/interpreting-charts.html*.

[9] T. Geldsetzer, M. Arkett, T. Zagon, F. Charbonneau, J. J. Yackel, and R. K. Scharien, "All-season compact-polarimetry C-band SAR observations of sea ice," *Canadian Journal of Remote Sensing*, vol. 41, no. 5, pp. 485–504, 2015.

[10] "Sea-ice information services in the world," *World Meteorological Organization*, vol. Technical Report 574, 2017.

[11] S. Leigh, Z. Wang, and D. A. Clausi, "Automated ice–water classification using dual polarization SAR satellite imagery," *IEEE Transactions on Geoscience and Remote Sensing*, vol. 52, no. 9, pp. 5529–5539, 2014.

[12] X. Yang and D. A. Clausi, "Evaluating SAR sea ice image segmentation using edge-preserving region-based MRFs," *IEEE Journal of Selected Topics in Applied Earth Observations and Remote Sensing*, vol. 5, no. 5, pp. 1383–1393, 2012.

[13] H. Liu, H. Guo, and L. Zhang, "SVM-based sea ice classification using textural features and concentration from RADARSAT-2 dual-pol ScanSAR data," *IEEE Journal of Selected Topics in Applied Earth Observations and Remote Sensing*, vol. 8, no. 4, pp. 1601–1613, 2015.

[14] S. Singha and R. Ressel, "Arctic sea ice characterization using RISAT-1 compact-pol SAR imagery and feature evaluation: A case study over northeast Greenland," *IEEE Journal of Selected Topics in Applied Earth Observations and Remote Sensing*, 2017.

[15] X. Zhang, J. Zhang, M. Liu, and J. Meng, "Assessment of C-band compact polarimetry SAR for sea ice classification," *Acta Oceanologica Sinica*, vol. 35, no. 5, pp. 79–88, 2016.

[16] H. Li and W. Perrie, "Sea ice characterization and classification using hybrid polarimetry SAR," *IEEE Journal of Selected Topics in Applied Earth Observations and Remote Sensing*, vol. 9, no. 11, pp. 4998–5010, 2016.

[17] M. M. Espeseth, C. Brekke, and S. N. Anfinsen, "Hybrid-polarity and reconstruction methods for sea ice with L-and C-band SAR," *IEEE Geoscience and Remote Sensing Letters*, vol. 13, no. 3, pp. 467–471, 2016.

[18] R. K. Raney, J. T. Cahill, G. Patterson, and D. B. J. Bussey, "The m-chi decomposition of hybrid dual-polarimetric radar data with application to lunar craters," *Journal of Geophysical Research: Planets*, vol. 117, no. E12, 2012.

[19] S. Z. Li, *Markov Random Field Modeling in Image Analysis*. Springer Science and Business Media, 2009.

[20] Q. Yu and D. A. Clausi, "IRGS: Image segmentation using edge penalties and region growing," *IEEE Transactions on Pattern Analysis and Machine Intelligence*, vol. 30, no. 12, pp. 2126–2139, 2008.

[21] P. Yu, A. Qin, and D. A. Clausi, "Unsupervised polarimetric SAR image segmentation and classification using region growing with edge penalty," *IEEE Transactions on Geoscience and Remote Sensing*, vol. 50, no. 4, pp. 1302–1317, 2012.

[22] F. Li, D. A. Clausi, L. Xu, and A. Wong, "ST-IRGS: A region-based self-training algorithm applied to hyperspectral image classification and segmentation," *IEEE Transactions on Geoscience and Remote Sensing*, vol. 56, no. 1, pp. 3–16, 2018.

[23] M. Ghanbari, D. A. Clausi, L. Xu, and M. Jiang, "Contextual classification of sea-ice types using compact polarimetric SAR data," *IEEE Transactions on Geoscience and Remote Sensing*, vol. 57, no. 10, pp. 7476–7491, 2019.

[24] M. Ghanbari, D. A. Clausi, and L. Xu, "CP-IRGS: A region-based segmentation of multilook complex compact polarimetric SAR data," *IEEE Journal of Selected Topics in Applied Earth Observations and Remote Sensing*, vol. 14, pp. 6559–6571, 2021.

[25] M. Ghanbari, L. Xu, and D. A. Clausi, "Local and global spatial information for land cover semi-supervised classification of complex polarimetric SAR data," *Submitted to IEEE Transactions on Geoscience and Remote Sensing*, 2021.

[26] Q. Yu and D. Clausi, "SAR sea-ice image analysis based on iterative region growing using semantics," *IEEE Transactions on Geoscience and Remote Sensing*, vol. 45, no. 12, pp. 3919–3931, 2007.

[27] R. Achanta, A. Shaji, K. Smith, A. Lucchi, P. Fua, and S. Süsstrunk, "Slic superpixels," Tech. Rep., 2010.

[28] L. Vincent and P. Soille, "Watersheds in digital spaces: an efficient algorithm based on immersion simulations," *IEEE Transactions on Pattern Analysis and Machine Intelligence*, no. 6, pp. 583–598, 1991.

[29] C. Cortes and V. Vapnik, "Support-vector networks," *Machine Learning*, vol. 20, no. 3, pp. 273–297, 1995.

[30] J.-S. Lee and E. Pottier, *Polarimetric Radar Imaging: From Basics to Applications*. CRC press, 2009.

[31] W.-M. Boerner, W.-L. Yan, A.-Q. Xi, and Y. Yamaguchi, "Basic concepts of radar polarimetry," in *Direct and Inverse Methods in Radar Polarimetry*. Springer, 1992, pp. 155–245.

[32] S. Cloude, *Polarisation: Applications in Remote Sensing*. Oxford University Press, 2010.

[33] J.-C. Souyris and S. Mingot, "Polarimetry based on one transmitting and two receiving polarizations: the $\frac{\pi}{4}$ mode," in *Geoscience and Remote Sensing Symposium, 2002. IGARSS'02. 2002 IEEE International*, vol. 1. IEEE, 2002, pp. 629–631.

[34] R. K. Raney, "Comments on hybrid-polarity SAR architecture," in *Geoscience and Remote Sensing Symposium, 2007. IGARSS 2007. IEEE International*. IEEE, 2007, pp. 2229–2231.

[35] S. R. Cloude, D. G. Goodenough, and H. Chen, "Compact decomposition theory," *IEEE Geoscience and Remote Sensing Letters*, vol. 9, no. 1, pp. 28–32, 2012.

[36] P. C. Dubois-Fernandez, J.-C. Souyris, S. Angelliaume, and F. Garestier, "The compact polarimetry alternative for spaceborne SAR at low frequency," *IEEE Transactions on Geoscience and Remote Sensing*, vol. 46, no. 10, pp. 3208–3222, 2008.

[37] R. K. Raney, "Dual-polarized SAR and Stokes parameters," *IEEE Geoscience and Remote Sensing Letters*, vol. 3, no. 3, pp. 317–319, 2006.

[38] J.-C. Souyris, P. Imbo, R. Fjortoft, S. Mingot, and J.-S. Lee, "Compact polarimetry based on symmetry properties of geophysical media: The $\frac{\pi}{4}$ mode," *IEEE Transactions on Geoscience and Remote Sensing*, vol. 43, no. 3, pp. 634–646, 2005.

[39] M. E. Nord, T. L. Ainsworth, J.-S. Lee, and N. J. Stacy, "Comparison of compact polarimetric synthetic aperture radar modes," *IEEE Transactions on Geoscience and Remote Sensing*, vol. 47, no. 1, pp. 174–188, 2009.

[40] S. Nghiem, S. Yueh, R. Kwok, and F. Li, "Symmetry properties in polarimetric remote sensing," *Radio Science*, vol. 27, no. 05, pp. 693–711, 1992.

[41] M. J. Collins, M. Denbina, and G. Atteia, "On the reconstruction of quad-pol SAR data from compact polarimetry data for ocean target detection," *IEEE Transactions on Geoscience and Remote Sensing*, vol. 51, no. 1, pp. 591–600, 2013.

[42] T. Ainsworth, J. Kelly, and J.-S. Lee, "Classification comparisons between dual-pol, compact polarimetric and quad-pol SAR imagery," *ISPRS Journal of Photogrammetry and Remote Sensing*, vol. 64, no. 5, pp. 464–471, 2009.

[43] Y. Li, Y. Zhang, J. Chen, and H. Zhang, "Improved compact polarimetric SAR quad-pol reconstruction algorithm for oil spill detection," *IEEE Geoscience and Remote Sensing Letters*, vol. 11, no. 6, pp. 1139–1142, 2014.

[44] M. J. Collins, M. Denbina, B. Minchew, C. E. Jones, and B. Holt, "On the use of simulated airborne compact polarimetric SAR for characterizing oil–water mixing of the deepwater horizon oil spill," *IEEE Journal of Selected Topics in Applied Earth Observations and Remote Sensing*, vol. 8, no. 3, pp. 1062–1077, 2015.

[45] B. Zhang, X. Li, W. Perrie, and O. Garcia-Pineda, "Compact polarimetric synthetic aperture radar for marine oil platform and slick detection," *IEEE Transactions on Geoscience and Remote Sensing*, vol. 55, no. 3, pp. 1407–1423, 2017.

[46] C. Lardeux, P.-L. Frison, C. Tison, J.-C. Souyris, B. Stoll, B. Fruneau, and J.-P. Rudant, "Classification of tropical vegetation using multifrequency partial SAR polarimetry," *IEEE Geoscience and Remote Sensing Letters*, vol. 8, no. 1, pp. 133–137, 2011.

[47] B. Souissi, M. Ouarzeddine, and A. Belhadj-Aissa, "Optimal SVM classification for compact polarimetric data using Stokes parameters," *Journal of Mathematical Modelling and Algorithms in Operations Research*, vol. 13, no. 4, p. 433, 2014.

[48] A. Aghabalaei, Y. Maghsoudi, and H. Ebadi, "Forest classification using extracted PolSAR features from compact polarimetry data," *Advances in space research*, vol. 57, no. 9, pp. 1939–1950, 2016.

[49] J. van der Sanden and T. Geldsetzer, "Compact polarimetry in support of lake ice breakup monitoring: Anticipating the RADARSAT Constellation Mission," *Canadian Journal of Remote Sensing*, vol. 41, no. 5, pp. 440–457, 2015.

[50] Z. Yang, K. Li, L. Liu, Y. Shao, B. Brisco, and W. Li, "Rice growth monitoring using simulated compact polarimetric C band SAR," *Radio Science*, vol. 49, no. 12, pp. 1300–1315, 2014.

[51] R. Shirvany, M. Chabert, and J.-Y. Tourneret, "Ship and oil-spill detection using the degree of polarization in linear and hybrid/compact dual-pol SAR," *IEEE Journal of Selected Topics in Applied Earth Observations and Remote Sensing*, vol. 5, no. 3, pp. 885–892, 2012.

[52] A.-B. Salberg, Ø. Rudjord, and A. H. S. Solberg, "Oil spill detection in hybrid-polarimetric SAR images," *IEEE Transactions on Geoscience and Remote Sensing*, vol. 52, no. 10, pp. 6521–6533, 2014.

[53] F. Nunziata, M. Migliaccio, and X. Li, "Sea oil slick observation using hybrid-polarity SAR architecture," *IEEE Journal of Oceanic Engineering*, vol. 40, no. 2, pp. 426–440, 2015.

[54] J. Yin, J. Yang, Z.-S. Zhou, and J. Song, "The extended bragg scattering model-based method for ship and oil-spill observation using compact polarimetric SAR," *IEEE Journal of Selected Topics in Applied Earth Observations and Remote Sensing*, vol. 8, no. 8, pp. 3760–3772, 2015.

[55] A. Buono, F. Nunziata, M. Migliaccio, and X. Li, "Polarimetric analysis of compact-polarimetry SAR architectures for sea oil slick observation," *IEEE Transactions on Geoscience and Remote Sensing*, vol. 54, no. 10, pp. 5862–5874, 2016.

[56] D. A. Clausi, A. Qin, M. Chowdhury, P. Yu, and P. Maillard, "MAGIC: MAp-guided ice classification system," *Canadian Journal of Remote Sensing*, vol. 36, no. S1, pp. S13–S25, 2010.

[57] S. Ochilov and D. A. Clausi, "Operational SAR sea-ice image classification," *IEEE Transactions on Geoscience and Remote Sensing*, vol. 50, no. 11, pp. 4397–4408, 2012.

[58] A. Qin and D. A. Clausi, "Multivariate image segmentation using semantic region growing with adaptive edge penalty," *IEEE Transactions on Image Processing*, vol. 19, no. 8, pp. 2157–2170, 2010.

[59] P. Yu, A. Qin, and D. A. Clausi, "Feature extraction of dual-pol SAR imagery for sea ice image segmentation," *Canadian Journal of Remote Sensing*, vol. 38, no. 03, pp. 352–366, 2012.

[60] P. Maillard, D. A. Clausi, and H. Deng, "Operational map-guided classification of SAR sea ice imagery," *IEEE Transactions on Geoscience and Remote Sensing*, vol. 43, no. 12, pp. 2940–2951, 2005.

[61] J.-S. Lee, M. R. Grunes, and R. Kwok, "Classification of multi-look polarimetric SAR imagery based on complex Wishart distribution," *International Journal of Remote Sensing*, vol. 15, no. 11, pp. 2299–2311, 1994.

[62] B. Scholkopf and A. J. Smola, *Learning with Kernels: Support Vector Machines, Regularization, Optimization, and Beyond.* MIT press, 2001.

[63] Y. Tarabalka, J. Chanussot, and J. A. Benediktsson, "Segmentation and classification of hyperspectral images using minimum spanning forest grown from automatically selected markers," *IEEE Transactions on Systems, Man, and Cybernetics, Part B (Cybernetics)*, vol. 40, no. 5, pp. 1267–1279, 2009.

[64] ——, "Segmentation and classification of hyperspectral images using watershed transformation," *Pattern Recognition*, vol. 43, no. 7, pp. 2367–2379, 2010.

[65] X. Cao, D. Wang, X. Wang, J. Zhao, and L. Jiao, "Hyperspectral imagery classification with cascaded support vector machines and multi-scale superpixel segmentation," *International Journal of Remote Sensing*, vol. 41, no. 12, pp. 4530–4550, 2020.

[66] T. Geldsetzer, F. Charbonneau, M. Arkett, and T. Zagon, "Ocean wind study using simulated RCM compact-polarimetry SAR," *Canadian Journal of Remote Sensing*, vol. 41, no. 5, pp. 418–430, 2015.

[67] S. R. Cloude and E. Pottier, "An entropy based classification scheme for land applications of polarimetric SAR," *IEEE transactions on geoscience and remote sensing*, vol. 35, no. 1, pp. 68–78, 1997.

[68] R. Touzi, A. Deschamps, and G. Rother, "Phase of target scattering for wetland characterization using polarimetric C-band SAR," *IEEE Transactions on Geoscience and Remote Sensing*, vol. 47, no. 9, pp. 3241–3261, 2009.

[69] R. K. Raney, "Synthetic aperture radar hybrid-polarity method and architecture for obtaining the Stokes parameters of a backscattered field," Jun. 29 2010, uS Patent 7,746,267.

[70] R. Raney, "Comparing compact and quadrature polarimetric SAR performance," *IEEE Geoscience and Remote Sensing Letters*, vol. 13, no. 6, pp. 861–864, 2016.

[71] G. A. Seber, *Multivariate Observations.* John Wiley and Sons, 2009, vol. 252.

[72] C. Oliver and S. Quegan, *Understanding Synthetic Aperture Radar Images.* SciTech Publishing, 2004.

[73] N. R. Goodman, "Statistical analysis based on a certain multivariate complex Gaussian distribution (an introduction)," *The Annals of mathematical statistics*, vol. 34, no. 1, pp. 152–177, 1963.

[74] A. C. Frery, A. Correa, C. D. Rennó, F. Corina da da C, J. Jacobo-Berlles, K. L. Vasconcellos, M. Mejail, and S. J. Sant'anna, "Models for synthetic aperture radar image analysis," *Resenhas do Instituto de Matemática e Estatística da Universidade de São Paulo*, vol. 4, no. 1, pp. 45–77, 1999.

[75] A. P. Doulgeris, S. N. Anfinsen, and T. Eltoft, "Classification with a non-gaussian model for PolSAR data," *IEEE Transactions on Geoscience and Remote Sensing*, vol. 46, no. 10, pp. 2999–3009, 2008.

[76] A. C. Frery, A. H. Correia, and C. d. C. Freitas, "Classifying multifrequency fully polarimetric imagery with multiple sources of statistical evidence and contextual information," *IEEE Transactions on Geoscience and Remote Sensing*, vol. 45, no. 10, pp. 3098–3109, 2007.

[77] H.-C. Lee and D. R. Cok, "Detecting boundaries in a vector field," *IEEE Transactions on Signal Processing*, vol. 39, no. 5, pp. 1181–1194, 1991.

[78] R. Touzi, A. Lopes, and P. Bousquet, "A statistical and geometrical edge detector for SAR images," *IEEE Transactions on Geoscience and Remote Sensing*, vol. 26, no. 6, pp. 764–773, 1988.

[79] C. Oliver, D. Blacknell, and R. White, "Optimum edge detection in SAR," *IEE Proceedings-Radar, Sonar and Navigation*, vol. 143, no. 1, pp. 31–40, 1996.

[80] J. Schou, H. Skriver, A. A. Nielsen, and K. Conradsen, "CFAR edge detector for polarimetric SAR images," *IEEE Transactions on Geoscience and Remote Sensing*, vol. 41, no. 1, pp. 20–32, 2003.

[81] V. Akbari, S. N. Anfinsen, A. P. Doulgeris, T. Eltoft, G. Moser, and S. B. Serpico, "Polarimetric SAR change detection with the complex Hotelling–Lawley trace statistic," *IEEE Transactions on Geoscience and Remote Sensing*, vol. 54, no. 7, pp. 3953–3966, 2016.

[82] M. Ghanbari and V. Akbari, "Unsupervised change detection in polarimetric SAR data with the Hotelling-Lawley trace statistic and minimum-error thresholding," *IEEE Journal of Selected Topics in Applied Earth Observations and Remote Sensing*, vol. 11, no. 12, pp. 4551–4562, 2018.

[83] X. Descombes, R. D. Morris, J. Zerubia, and M. Berthod, "Estimation of Markov random field prior parameters using Markov chain Monte Carlo maximum likelihood," *IEEE Transactions on Image Processing*, vol. 8, no. 7, pp. 954–963, 1999.

[84] T. Esch, A. Schenk, T. Ullmann, M. Thiel, A. Roth, and S. Dech, "Characterization of land cover types in TerraSAR-X images by combined analysis of speckle statistics and intensity information," *IEEE Transactions on Geoscience and Remote Sensing*, vol. 49, no. 6, pp. 1911–1925, 2011.

[85] K. Huang, W. Nie, and N. Luo, "Fully polarized SAR imagery classification based on deep reinforcement learning method using multiple polarimetric features," *IEEE Journal of Selected Topics in Applied Earth Observations and Remote Sensing*, vol. 12, no. 10, pp. 3719–3730, 2019.

[86] R. Yang, X. Xu, Z. Xu, H. Dong, R. Gui, and F. Pu, "Dynamic fractal texture analysis for PolSAR land cover classification," *IEEE Transactions on Geoscience and Remote Sensing*, vol. 57, no. 8, pp. 5991–6002, 2019.

[87] B. Ren, B. Hou, J. Chanussot, and L. Jiao, "PolSAR feature extraction via tensor embedding framework for land cover classification," *IEEE Transactions on Geoscience and Remote Sensing*, vol. 58, no. 4, pp. 2337–2351, 2019.

[88] B. Brisco, K. Li, B. Tedford, F. Charbonneau, S. Yun, and K. Murnaghan, "Compact polarimetry assessment for rice and wetland mapping," *International journal of remote sensing*, vol. 34, no. 6, pp. 1949–1964, 2013.

[89] M. Ohki and M. Shimada, "Large-area land use and land cover classification with quad, compact, and dual polarization SAR data by PALSAR-2," *IEEE Transactions on Geoscience and Remote Sensing*, vol. 56, no. 9, pp. 5550–5557, 2018.

[90] X. Ren and J. Malik, "Learning a classification model for segmentation," in *Computer Vision, IEEE International Conference on*, vol. 2. IEEE Computer Society, 2003, pp. 10–10.

[91] T. Priya, S. Prasad, and H. Wu, "Superpixels for spatially reinforced bayesian classification of hyperspectral images," *IEEE Geoscience and Remote Sensing Letters*, vol. 12, no. 5, pp. 1071–1075, 2015.

[92] A. Farag, L. Lu, H. R. Roth, J. Liu, E. Turkbey, and R. M. Summers, "A bottom-up approach for pancreas segmentation using cascaded superpixels and (deep) image patch labeling," *IEEE Transactions on Image Processing*, vol. 26, no. 1, pp. 386–399, 2016.

[93] D. Stutz, A. Hermans, and B. Leibe, "Superpixels: An evaluation of the state-of-the-art," *Computer Vision and Image Understanding*, vol. 166, pp. 1–27, 2018.

[94] R. Uziel, M. Ronen, and O. Freifeld, "Bayesian adaptive superpixel segmentation," in *Proceedings of the IEEE International Conference on Computer Vision*, 2019, pp. 8470–8479.

[95] M. Ghanbari, D. Clausi, L. Xu, and M. Jiang, "Unsupervised segmentation of multilook compact polarimetric SAR data based on complex Wishart distribution," in *IGARSS 2020-2020 IEEE International Geoscience and Remote Sensing Symposium*. IEEE, pp. 1456–1459.

[96] X. Zhu and A. B. Goldberg, "Introduction to semi-supervised learning," *Synthesis Lectures on Artificial Intelligence and Machine Learning*, vol. 3, no. 1, pp. 1–130, 2009.

[97] P. Sellars, A. I. Aviles-Rivero, and C.-B. Schönlieb, "Superpixel contracted graph-based learning for hyperspectral image classification," *IEEE Transactions on Geoscience and Remote Sensing*, vol. 58, no. 6, pp. 4180–4193, 2020.

[98] X. Zhu and Z. Ghahramani, "Learning from labeled and unlabeled data with label propagation," 2002.

[99] D. Zhou, O. Bousquet, T. N. Lal, J. Weston, and B. Schölkopf, "Learning with local and global consistency," in *Advances in Neural Information Processing Systems*, 2004, pp. 321–328.

[100] S. Jia, X. Deng, M. Xu, J. Zhou, and X. Jia, "Superpixel-level weighted label propagation for hyperspectral image classification," *IEEE Transactions on Geoscience and Remote Sensing*, 2020.

[101] L. Wang, C. Shi, C. Diao, W. Ji, and D. Yin, "A survey of methods incorporating spatial information in image classification and spectral unmixing," *International Journal of Remote Sensing*, vol. 37, no. 16, pp. 3870–3910, 2016.

[102] J. Geng, H. Wang, J. Fan, and X. Ma, "Deep supervised and contractive neural network for SAR image classification," *IEEE Transactions on Geoscience and Remote Sensing*, vol. 55, no. 4, pp. 2442–2459, 2017.

[103] R. M. Haralick, K. Shanmugam, and I. H. Dinstein, "Textural features for image classification," *IEEE Transactions on Systems, Man, and Cybernetics*, no. 6, pp. 610–621, 1973.

[104] D. A. Clausi, "An analysis of co-occurrence texture statistics as a function of grey level quantization," *Canadian Journal of Remote Sensing*, vol. 28, no. 1, pp. 45–62, 2002.

[105] A. Jain and G. Healey, "A multiscale representation including opponent color features for texture recognition," *IEEE Transactions on Image Processing*, vol. 7, no. 1, pp. 124–128, 1998.

[106] J. Geng, J. Fan, H. Wang, X. Ma, B. Li, and F. Chen, "High-resolution SAR image classification via deep convolutional autoencoders," *IEEE Geoscience and Remote Sensing Letters*, vol. 12, no. 11, pp. 2351–2355, 2015.

[107] Z. Huang, M. Datcu, Z. Pan, and B. Lei, "Deep SAR-Net: Learning objects from signals," *ISPRS Journal of Photogrammetry and Remote Sensing*, vol. 161, pp. 179–193, 2020.

[108] Y. Chen, N. M. Nasrabadi, and T. D. Tran, "Hyperspectral image classification via kernel sparse representation," *IEEE Transactions on Geoscience and Remote sensing*, vol. 51, no. 1, pp. 217–231, 2012.

[109] X. Lv, D. Ming, Y. Chen, and M. Wang, "Very high resolution remote sensing image classification with SEEDS-CNN and scale effect analysis for superpixel CNN classification," *International Journal of Remote Sensing*, vol. 40, no. 2, pp. 506–531, 2019.

[110] R. Ji, Y. Gao, R. Hong, Q. Liu, D. Tao, and X. Li, "Spectral-spatial constraint hyperspectral image classification," *IEEE Transactions on Geoscience and Remote Sensing*, vol. 52, no. 3, pp. 1811–1824, 2013.

[111] S. Li, T. Lu, L. Fang, X. Jia, and J. A. Benediktsson, "Probabilistic fusion of pixel-level and superpixel-level hyperspectral image classification," *IEEE Transactions on Geoscience and Remote Sensing*, vol. 54, no. 12, pp. 7416–7430, 2016.

[112] B. Wang, Z. Tu, and J. K. Tsotsos, "Dynamic label propagation for semi-supervised multi-class multi-label classification," in *Proceedings of the IEEE International Conference on Computer Vision*, 2013, pp. 425–432.

[113] S. Arisoy and K. Kayabol, "Mixture-based superpixel segmentation and classification of SAR images," *IEEE Geoscience and Remote Sensing Letters*, vol. 13, no. 11, pp. 1721–1725, 2016.

[114] V. Mnih, K. Kavukcuoglu, D. Silver, A. A. Rusu, J. Veness, M. G. Bellemare, A. Graves, M. Riedmiller, A. K. Fidjeland, G. Ostrovski *et al.*, "Human-level control through deep reinforcement learning," *nature*, vol. 518, no. 7540, pp. 529–533, 2015.

[115] T.-H. Chan, K. Jia, S. Gao, J. Lu, Z. Zeng, and Y. Ma, "Pcanet: A simple deep learning baseline for image classification?" *IEEE Transactions on Image Processing*, vol. 24, no. 12, pp. 5017–5032, 2015.

[116] J. Guo, L. Wang, D. Zhu, C.-Y. Hu, and C.-Y. Xue, "Subspace learning network: An efficient ConvNet for PolSAR image classification," *IEEE Geoscience and Remote Sensing Letters*, vol. 16, no. 12, pp. 1849–1853, 2019.

[117] B. Zou, X. Xu, and L. Zhang, "Object-based classification of PolSAR images based on spatial and semantic features," *IEEE Journal of Selected Topics in Applied Earth Observations and Remote Sensing*, vol. 13, pp. 609–619, 2020.

[118] S. Yan, D. Xu, B. Zhang, H.-J. Zhang, Q. Yang, and S. Lin, "Graph embedding and extensions: A general framework for dimensionality reduction," *IEEE Transactions on Pattern Analysis and Machine Intelligence*, vol. 29, no. 1, pp. 40–51, 2006.

[119] B. Wei, J. Yu, C. Wang, H. Wu, and J. Li, "PolSAR image classification using a semi-supervised classifier based on hypergraph learning," *Remote Sensing Letters*, vol. 5, no. 4, pp. 386–395, 2014.

[120] J. Yu, D. Tao, and M. Wang, "Adaptive hypergraph learning and its application in image classification," *IEEE Transactions on Image Processing*, vol. 21, no. 7, pp. 3262–3272, 2012.

[121] X. Zhu, Z. Ghahramani, and J. D. Lafferty, "Semi-supervised learning using gaussian fields and harmonic functions," in *Proceedings of the 20th International Conference on Machine learning (ICML-03)*, 2003, pp. 912–919.

[122] B. Hou, Q. Wu, Z. Wen, and L. Jiao, "Robust semisupervised classification for PolSAR image with noisy labels," *IEEE Transactions on Geoscience and Remote Sensing*, vol. 55, no. 11, pp. 6440–6455, 2017.

[123] W. Hua, S. Wang, H. Liu, K. Liu, Y. Guo, and L. Jiao, "Semisupervised PolSAR image classification based on improved cotraining," *IEEE Journal of Selected Topics in Applied Earth Observations and Remote Sensing*, vol. 10, no. 11, pp. 4971–4986, 2017.

[124] H. Liu, S. Yang, S. Gou, S. Liu, and L. Jiao, "Terrain classification based on spatial multi-attribute graph using polarimetric SAR data," *Applied Soft Computing*, vol. 68, pp. 24–38, 2018.

[125] S. Wang, Y. Guo, W. Hua, X. Liu, G. Song, B. Hou, and L. Jiao, "Semi-supervised PolSAR image classification based on improved tri-training with a minimum spanning tree," *IEEE Transactions on Geoscience and Remote Sensing*, 2020.

[126] B. Hou, J. Guan, Q. Wu, and L. Jiao, "Semisupervised classification of PolSAR image incorporating labels' semantic priors," *IEEE Geoscience and Remote Sensing Letters*, 2019.

[127] H. Bi, F. Xu, Z. Wei, Y. Xue, and Z. Xu, "An active deep learning approach for minimally supervised PolSAR image classification," *IEEE Transactions on Geoscience and Remote Sensing*, vol. 57, no. 11, pp. 9378–9395, 2019.

[128] T. Gadhiya and A. K. Roy, "Superpixel-driven optimized Wishart network for fast PolSAR image classification using global k-means algorithm," *IEEE Transactions on Geoscience and Remote Sensing*, vol. 58, no. 1, pp. 97–109, 2019.

[129] L. Jiao and F. Liu, "Wishart deep stacking network for fast POLSAR image classification," *IEEE Transactions on Image Processing*, vol. 25, no. 7, pp. 3273–3286, 2016.

[130] B. Hou, H. Kou, and L. Jiao, "Classification of polarimetric SAR images using multilayer autoencoders and superpixels," *IEEE Journal of Selected Topics in Applied Earth Observations and Remote Sensing*, vol. 9, no. 7, pp. 3072–3081, 2016.

[131] J. Geng, X. Ma, J. Fan, and H. Wang, "Semisupervised classification of polarimetric SAR image via superpixel restrained deep neural network," *IEEE Geoscience and Remote Sensing Letters*, vol. 15, no. 1, pp. 122–126, 2017.

[132] X. Liu, L. Jiao, X. Tang, Q. Sun, and D. Zhang, "Polarimetric convolutional network for PolSAR image classification," *IEEE Transactions on Geoscience and Remote Sensing*, vol. 57, no. 5, pp. 3040–3054, 2018.

[133] W. Xie, G. Ma, F. Zhao, H. Liu, and L. Zhang, "PolSAR image classification via a novel semi-supervised recurrent complex-valued convolution neural network," *Neurocomputing*, 2020.

[134] S. Ren and F. Zhou, "Semi-supervised classification for PolSAR data with multi-scale evolving weighted graph convolutional network," *IEEE Journal of Selected Topics in Applied Earth Observations and Remote Sensing*, vol. 14, pp. 2911–2927, 2021.

[135] L. Breiman, "Random forests," *Machine Learning*, vol. 45, no. 1, pp. 5–32, 2001.